Comparison and Analysis of Attitude Control Systems of a Satellite Using Reaction Wheel Actuators

Ibrahim Kök

Comparison and Analysis of Attitude Control Systems of a Satellite Using Reaction Wheel Actuators

A Thesis Presented to:

University of Würzburg

and

Lulea University of Technology

In partial fulfillment of the requirements for the degree of

Master of Science

in the subject of

Space Science and Technology

presented by

İbrahim Kök

Supervisors:

Prof. Dr.-Ing. Sergio Montenegro

Dr. Anita Enmark

M.Sc. Eng. Atheel Redah

October 2012

Acknowledgements

First of all, I would like to gratefully thank Prof. Dr. Sergio Montenegro for providing me to be a part of such an interesting project and for his support during my thesis.

Special thanks to Dr. Johnny Ejemalm and my examiner Dr. Anita Enmark in Lulea University of Technology in Kiruna, who appreciated my problems and supported me during my thesis.

My sincere thanks to my supervisor Atheel Redah for his support and guidance throughout the thesis. The meetings and discussions with him helped me a lot and highly appreciated.

Finally I would like to thank people from University of Würzburg in Germany and Lulea University of Technology in Sweden for providing me great opportunities and supporting me throughout my two year master's program.

Abstract

In this thesis, analysis and comparison of different attitude control systems of a satellite using different reaction wheel configurations were investigated. Three different reaction wheel configurations (e.g. tetrahedron configuration, pyramid configuration, standard orthogonal 3-wheel configuration) and three control algorithms (Linear Quadratic Regulator, Sliding Mode, Integrator Backstepping) were analyzed and compared in terms of settling times, power consumptions and actuator failure robustness.

A nonlinear mathematical model of spacecraft dynamics was presented. A quaternion based PD controller was linearized and a cost-efficient feedback gain matrix was found by LQR method. For the Sliding Mode, Lyapunov function was employed to guarantee convergence to the desired state. Integrator Backstepping controller recursively uses Lyapunov functions in each integrator level to cancel the nonlinear terms which ensures asymptotic stability. In the simulations a second order reference model was employed, which provides a rather smooth trajectory which consumes less power. All the controllers provided an accuracy of $\pm 0.01^\circ$ in Euler angles. Together with the controllers, different reaction wheel configurations were simulated and some results were tabulated for pyramid and tetrahedron configurations to compare them in terms of power consumptions and actuator failure robustness. Finally some conclusions were drawn from the results of the simulation and recommendations for future work was remarked.

Contents

Chapter 1

Introduction

1.1 Theoretical Background

The attitude determination and control system (ADCS) of spacecrafts has been widely investigated in the past years. ADCS is responsible for 3-axis stabilization and orientation of the satellite in desired direction. High pointing accuracy and reliability are the most important problems of the attitude control system designs. Several subsystems in a satellite, such as reorienting antennas or telescopes toward specified directions or keep solar arrays in proper direction relative to solar rays in order to absorb maximum energy, may require a stabilized satellite to get a better performance from payloads.

Dynamics of a spacecraft is time varying and non-linear. Different environmental disturbances and some system parameters which are not well known also affect the spacecraft dynamics. Moreover, actuator failure possibilities add more uncertanties to the overall system. Design of attitude control systems by regarding these environmental effects and uncertanties require proper algorithms and actuators. In order to evaluate the performance of an actual system, modelling and simulation of the actuators are important.[1]

Like in any other system of the satellite, redundancy is an important part of attitude control system. It is necessary to consider the possibility of reaction wheel failures. To provide the continuous 3-axis controllability in the case of a reaction wheel failure, four reaction wheel configurations are implemented in spacecrafts. The mostly used four-wheel configurations are namely tetrahedron and pyramid configurations. The tetrahedral configuration of reaction wheel structure has the advantage of having a net angular momentum of zero when all wheels are rotating at the same angular velocity.[2]

Different attitude parameterisations (i.e direction cosine matrix, Euler axis/angle parameters, Euler angles, quaternions, Rodrigues parameters, Gibbs vector) can be employed for the design of feedback control laws. The selection of minimal attitude coordinate sets like Euler angles leads to singularities in attitude parameters and kinematic equations. The most commonly used attitude parameter sets in attitude control system design are quaternions and the modified Rodrigues parameters. Quaternions have the advantages of offering a globally non-singular spacecraft attitude, successive rotations by a convenient quaternion multiplication rule and being well suited to onboard real-time implementations. [3]

Different linear and nonlinear control algorithms for attitude control have been investigated in the past years. A Quaternion Feedback Control is employed in this thesis, which is essentially a PD controller that is using a gain matrix determined by LQR control strategy. Sliding Mode Control (SMC) offers high levels of robustness in the precense of parameter uncertainties and dynamic model errors, mostly characterised by spacecraft inertia uncertainty and bounded disturbances. The conventional SMC design consists of two steps. First, a sliding manifold satisfying certain desired properties is selected. A discontinuous control is designed such that the system trajectories reach that manifold in finite time. [4] Integrator Backstepping Control is essentially a quternion feedback control based on Lyapunov stability theory (Appendix C). The method stabilizes the entire plant recursively starting from the state variables that are to be tracked by the closed loop system. A feedback control torque and positive definite Lyapunov function must be selected such that the first-order time derivative of the Lyapunov function is negative definite. [3]

1.2 Purpose of the Report

The purpose of this report is to apply one linear and two non-linear controllers for the attitude control of a satellite with three and four reaction wheel configurations and compare their performances. Different controllers with different reaction wheel configurations are compared with respect to power consumption, settling time and actuator failure tolerances. The nonlinear model of the satellite is developed and simulated in MATLAB/SIMULINK environment. The outcomings of this thesis will be implemented in a testbed, which is an air suspended sphere with four reaction wheels.

1.3 Literature Survey

Wertz (1978), Sidi (1997) and Wie (1998) are the basic references on spacecraft dynamics and control. Sidi (1997) has studied a complete reaction wheel-based attitude control system (ACS) with four reaction wheels and analyzed the system in terms of power consumption and effects of sensor noises and disturbances on ACS accuracy.[7] Kristiansen (2000) analyzed the performance of attitude control of a microsatellite employing magnetic torquers and reaction wheels and made Lyapunov analysis on the nonlinear satellite model.[6] Also in his thesis controllability and reachability of the satellite is studied. Topland (2004) modelled and simulated linear and nonlinear attitude control strategies for the microsatellite European Student Earth Orbiter (ESEO).[18] Ytherus (2003) modelled and simulated in his thesis attitude control system of a spacecraft which employs four reaction wheels in tetrahedron configuration.[19]

Stefanescu and Priproc (2012) studied attitude control of European Student Moon Orbiter (ESMO) satellite which has thrusters and reaction wheels as actuators.[9] The control system is based on the Linear Quadratic Regulator (LQR) theory. Kristiansen and Nicklasson (2005) presented the results on attitude control of a microsatellite by integrator backstepping based on quaternion feedback.[8] The controller is shown to be stable in the sense of Lyapunov. Yu et al. (2011) modelled a reconfigurable control system using variable-structure control and improved pseudo-inverse which is based on error quaternion nonlinear model.[12] The controller is shown to provide desirable control qualities in the event of one reaction wheel failure, and robust for disturbance. Hu (2009) proposed a robust adaptive fault-tolerant control approach to handle reaction wheel failures, external disturbances and time-varying inertia parameter uncertainties.[1] Simulation results show that the precise attitudes control is successfully achieved using various scenarios of control effect failures. Rao at al. studied the problem of attitude stabilization/tracking for a spacecraft in the presence of inertia uncertainty and external disturbance, a sliding mode controller has been designed to force the state variables of the closed loop system to converge to the reference values.[4] Johanessen (2006) analyzed attitude control system of ESMO microsatellite in terms of detecting reaction wheel failures, proposing a neural adaptive observer (NAO) for detection. [20]

1.4 Outline of the Report

Chapter 1 - Introduction presents the motivation, objectives and literature review done for this thesis work.

Chapter 2 – Definitions and Notations provides a description of various notations used throughout the report and some fundamental definitions are presented.

Chapter 3 – Mathematical Models provides a complete mathematical model of the satellite with kinematics and dynamics equations. Moreover, reaction wheel assembly configurations and electrical modeling of reaction wheels are mentioned.

Chapter 4 – Control Strategies provides definitions and derivations of one linear and two non-linear control algorithms.

Chapter 5 – Simulations and Results presents the simulation results for different control algorithms and different reaction wheel configurations.

Chapter 6 – Conclusion includes the conclusions drawn from the work done in this thesis together with some recommendations for future work.

Chapter 2

Definitions and Notations

This chapter provides descriptions of various notations used throughout the report and some fundamental definitions are presented. These notations and definitions are required for the mathematical models used throughout the thesis. This chapter includes definitions of basic reference systems, rotation matrices for the transformations between different frames and finally the inertia matrix of a satellite body.

2.1 Reference Systems

2.1.1 Earth Centered Inertial (ECI) Frame

This frame is fixed in space, which makes it a non-accelerated reference frame in which Newton's Laws are valid. The origin of the frame is located at the center of the Earth. Z-axis points towards the North Pole, X-axis points towards Vernal Equinox and the Y-axis completes the right hand Cartesian coordinate system. This frame is indicated by **i**.

2.1.2 Earth Centered Earth Fixed (ECEF) Frame

The origin of ECEF frame is also at the center of the Earth, however X and Y axes rotate with the Earth relative to the ECI frame about the Z-axis which extends through the North Pole. X-axis points towards the intersection of Greenwich meridian and the Equator, which represents zero degree longitude and zero degree latitude. Y-axis completes the right handed orthogonal system. The ECEF frame rotates relative to the ECI frame with a constant angular velocity of $\omega = 7.2921 * 10^{-5} \ rad/s$
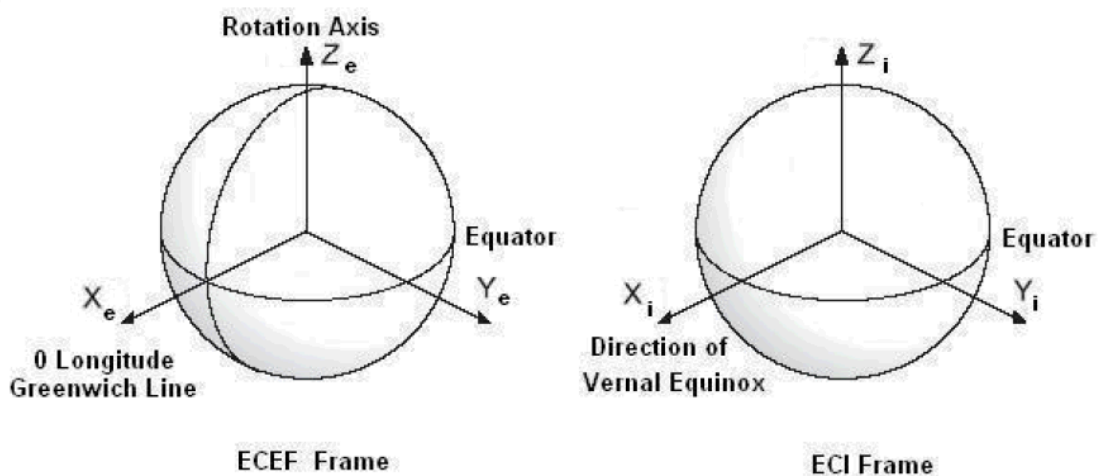
This frame is indicated by **e**.

Figure 2.1 – ECEF and ECI frames (Credits: [5])

2.1.3 Orbit Frame

The origin of this frame coincides with the center of the mass of the satellite. Z-axis points towards the center of the Earth. X-axis points in the direction of motion tangentially to the orbit. Y-axis completes the right hand system, as shown in Figure 2.2. The orbit frame is indicated by **o**.

2.1.4 Body Frame

The body frame is fixed with the satellite and its origin is located at the center of mass of the satellite. The orientation of the satellite is described relative to the orbit frame. The nadir side of the satellite is in Z-axis direction, while X and Y-axes coincide with the orbit frame axes when the satellite has an attitude of 0 degree in roll, pitch and yaw. The body frame is indicated by **b** (Figure 2.2).
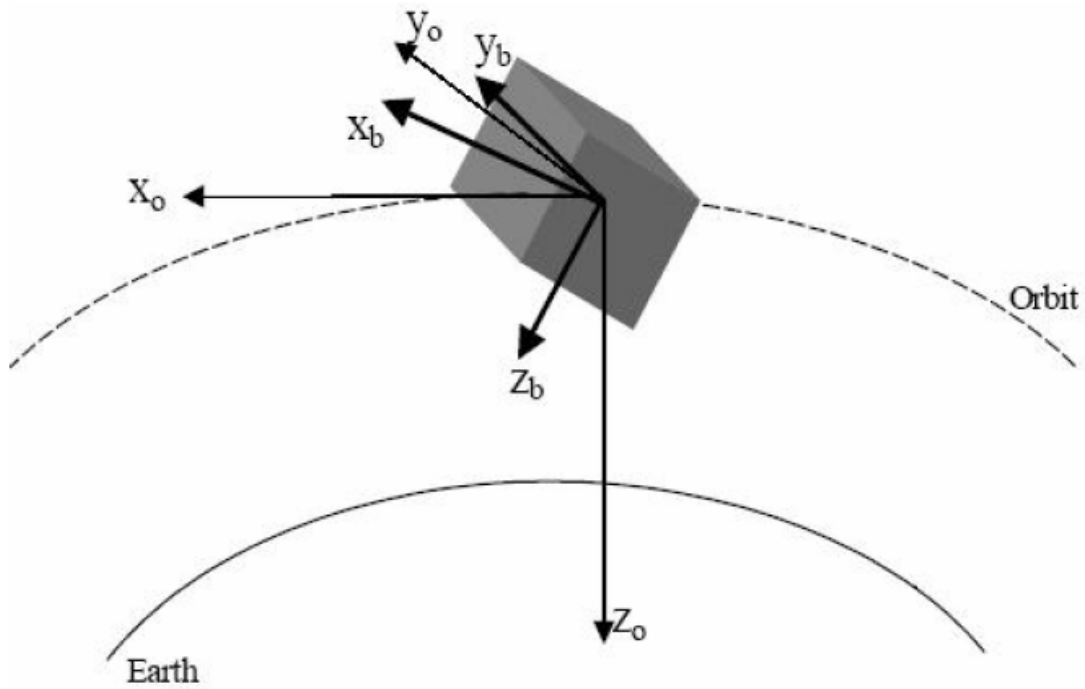

Figure 2.2 – The orbit and body frames (Credits: [5])

2.2 Rotation Matrix

The rotation matrix is used for transformation of a vector represented in one coordinate frame into another frame. The rotation matrix R from frame 'x' to frame 'y' is denoted by R_x^y. The rotation of a vector from one frame to another frame can be performed as follows [6]:

$$v^y = R_x^y v^x \tag{2.1}$$

Rotation matrix is a symmetric orthonormal matrix, which results in:

$$(R_y^x)^{-1} = (R_y^x)^T = R_x^y \tag{2.2}$$

An angle-axis parameterization corresponds to a rotation of angle Θ about λ axis, which can be defined as:

$$R_{\lambda,\Theta} = I_{3x3} + S(\lambda)\sin\Theta + (1 - \cos\Theta)S^2(\lambda) \tag{2.3}$$

where I is the 3-by-3 identity matrix and S(.) is the cross-product operator:

$$S(\omega) = \begin{bmatrix} 0 & -\omega_z & \omega_y \\ \omega_z & 0 & -\omega_x \\ -\omega_y & \omega_x & 0 \end{bmatrix}, \quad S^2(\lambda) = S(\lambda)S(\lambda) \tag{2.4}$$

2.2.1 Euler Angles

The successive angular rotations about the three orthogonal body axes are defined as the Euler angle rotations. The Euler roll angle (Ø) is the rotation about the **x** body axis, the pitch angle (Θ) is the rotation about the **y** body axis and the yaw angle (Ψ) is the rotation about the **z** body axis. Euler angle rotation matrices about each axis are defined as [7]:

$$R_x(\text{Ø}) = \begin{bmatrix} 1 & 0 & 0 \\ 0 & \cos\text{Ø} & \sin\text{Ø} \\ 0 & -\sin\text{Ø} & \cos\text{Ø} \end{bmatrix} \tag{2.5}$$

$$R_y(\Theta) = \begin{bmatrix} \cos\Theta & 0 & -\sin\Theta \\ 0 & 1 & 0 \\ \sin\Theta & 0 & \cos\Theta \end{bmatrix} \tag{2.6}$$

$$R_z(\Psi) = \begin{bmatrix} \cos\Psi & -\sin\Psi & 0 \\ \sin\Psi & \cos\Psi & 0 \\ 0 & 0 & 1 \end{bmatrix} \tag{2.7}$$

For different rotation sequences, different rotation matrices can be derived using these Euler angle rotation matrices above. For example, the rotation matrix for the transformation of $\Psi \rightarrow \theta \rightarrow \text{Ø}$ succesively about the z, y and x body axes can be achieved by the following multiplications:

$$R = R_x(\text{Ø})R_y(\Theta)R_z(\Psi) \tag{2.8}$$

$$R_o^b = \begin{bmatrix} \cos\Theta\cos\Psi & \cos\Theta\sin\Psi & -\sin\Theta \\ -\cos\text{Ø}\sin\Psi + \sin\text{Ø}\sin\Theta\cos\Psi & \cos\text{Ø}\cos\Psi + \sin\text{Ø}\sin\Theta\sin\Psi & \sin\text{Ø}\cos\Theta \\ \sin\text{Ø}\sin\Psi + \cos\text{Ø}\sin\Theta\cos\Psi & -\sin\text{Ø}\cos\Psi + \cos\text{Ø}\sin\Theta\sin\Psi & \cos\text{Ø}\cos\Theta \end{bmatrix} \tag{2.9}$$

2.2.2 Unit Quaternions

Unit quaternions (Euler parameters) are mostly used as attitude parameterizations to overcome the singularity problems. Euler's theorem states that, the most general

11

displacement of a rigid body with one point fixed is a rotation about some axis.[7] The elements of unit quaternions can be expressed in terms of the principal eigenvector $\hat{e}$ and the rotation angle Θ as follows:

$$\mathcal{E} = [\mathcal{E}_1 \quad \mathcal{E}_2 \quad \mathcal{E}_3]^T = \hat{e} \sin\left(\frac{\Theta}{2}\right), \quad \eta = \cos\left(\frac{\Theta}{2}\right), \quad \hat{e} = [e_1 \; e_2 \; e_3]^T \tag{2.10}$$

$$q = \begin{bmatrix} \eta \\ \mathcal{E}_1 \\ \mathcal{E}_2 \\ \mathcal{E}_3 \end{bmatrix} = \begin{bmatrix} \cos\left(\frac{\Theta}{2}\right) \\ \hat{e} \sin\left(\frac{\Theta}{2}\right) \end{bmatrix}, \quad 0 \leq \Theta \leq 2\pi \tag{2.11}$$
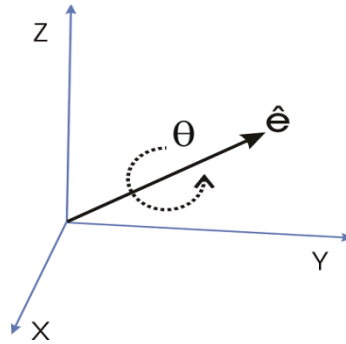
Figure 2.3 – A rotation represented by an Euler axis and angle

It is clear that,

$$q^T q = \eta^2 + \mathcal{E}_1{}^2 + \mathcal{E}_2{}^2 + \mathcal{E}_3{}^2 = 1 \tag{2.12}$$

The rotation matrix in quaternions can be expressed as follows [6]:

$$R(q) = I_{3x3} + 2\eta S(\mathcal{E}) + 2S^2(\mathcal{E}) \tag{2.13}$$

$$R_b^o(q) = \begin{bmatrix} 1 - 2(\mathcal{E}_2^2 + \mathcal{E}_3^2) & 2(\mathcal{E}_1\mathcal{E}_2 - \mathcal{E}_3\eta) & 2(\mathcal{E}_1\mathcal{E}_3 + \mathcal{E}_2\eta) \\ 2(\mathcal{E}_1\mathcal{E}_2 + \mathcal{E}_3\eta) & 1 - 2(\mathcal{E}_1^2 + \mathcal{E}_3^2) & 2(\mathcal{E}_2\mathcal{E}_3 - \mathcal{E}_1\eta) \\ 2(\mathcal{E}_1\mathcal{E}_3 - \mathcal{E}_2\eta) & 2(\mathcal{E}_2\mathcal{E}_3 + \mathcal{E}_1\eta) & 1 - 2(\mathcal{E}_1^2 + \mathcal{E}_2^2) \end{bmatrix} \tag{2.14}$$

2.3 Inertia Matrix

The inertia matrix of the satellite I can be defined as follows [5]:

$$I = \begin{bmatrix} I_x & -I_{xy} & -I_{xz} \\ -I_{yx} & I_y & -I_{yz} \\ -I_{zx} & -I_{zy} & I_z \end{bmatrix} \tag{2.15}$$

where

$$I_x = \int_V (y^2 + z^2)\rho_m \, dV, \quad I_y = \int_V (x^2 + z^2)\rho_m \, dV, \quad I_z = \int_V (x^2 + y^2)\rho_m \, dV \tag{2.16}$$

with mass of density ρ_m and volume V.

$I_{xy} = I_{yx}$, $I_{yz} = I_{zy}$ and $I_{xz} = I_{zx}$ are the products of inertia, which are defined as:

$$I_{xy} = \int_V xy\rho_m \, dV \qquad I_{xz} = \int_V xz\rho_m \, dV \qquad I_{yz} = \int_V yz\rho_m \, dV \qquad (2.17)$$

Assuming that the axes of the body frame coincide with the principal axes of the satellite inertia, the inertia matrix I can be reduced to:

$$I = \begin{bmatrix} I_x & 0 & 0 \\ 0 & I_y & 0 \\ 0 & 0 & I_z \end{bmatrix} \qquad (2.18)$$

Chapter 3

Mathematical Models

This chapter provides a complete mathematical model of the satellite with kinematics and dynamics equations. The disturbance torques experienced by satellites are mentioned. Moreover, reaction wheel assembly configurations and electrical modeling of reaction wheels are covered.

3.1 Kinematics Equations

Coordinate transformation of a vector **r** from frame *a* to frame *b* is defined as:

$$r^b = R_a^b r^a \tag{3.1}$$

The time derivative of rotation matrix R_a^b can be expressed as [8]:

$$\dot{R}_b^a = S(\omega_{ab}^a) R_b^a \tag{3.2}$$

where $S(.)$ is the cross-product operator:

$$S(\omega) = \begin{bmatrix} 0 & -\omega_z & \omega_y \\ \omega_z & 0 & -\omega_x \\ -\omega_y & \omega_x & 0 \end{bmatrix} \tag{3.3}$$

The rotation matrix can be expressed by Euler parameters as follows:

$$R_{\eta,\epsilon} = I_{3x3} + 2\eta S(\epsilon) + 2S^2(\epsilon) \tag{3.4}$$

where I is 3-by-3 identity matrix.

ω_{bo}^b is the angular velocity in body frame relative to the orbit frame, which is defined as:

$$\omega_{bo}^b = \omega_{bi}^b - R_o^b \omega_{oi}^o = \omega_{bi}^b + \omega_o c_2 \tag{3.5}$$

where $\omega_{oi}^o = [0 \; \omega_o \; 0]^T$ is the angular velocity of orbit frame with respect to inertial frame and $R_o^b = [c_1 \; c_2 \; c_3]$. From the definition of orbit frame, ω_o represents the angular velocity of the orbit frame about its y_o axis [7] and can be defined for a circular orbit as:

$\omega_o = \sqrt{\dfrac{\mu}{r_c^3}}$ where $\mu = 3.986x10^{14} \; m^3/s^2$ is the Earth's gravitational coefficient and r_c is the distance from the center of Earth.

The kinematics equations that describes the orientation of a satellite can be derived from equations (3.2) and (3.4) as [8]:

$$\dot{\eta} = -\frac{1}{2}\varepsilon^T \omega_{bo}^b \tag{3.6}$$

$$\dot{\varepsilon} = \frac{1}{2}\eta\omega_{bo}^b - \frac{1}{2}\omega_{bo}^b \times \varepsilon \tag{3.7}$$

where $\times$ is the cross product.

3.2 Dynamics Equations

The total angular momentum of the spacecraft is [9]:

$$H_b = I\omega_b + h_w \tag{3.8}$$

where I is the inertia matrix of the satellite, ω_b is the angular velocity of satellite in body frame and h_w is the angular momentum of the reaction wheels, which can be described in body frame as follows:

$$h_w = LI_w\omega_w \tag{3.9}$$

where $I_w = diag(I_{w1}, I_{w2}, \dots, I_{wn})$ is the reaction wheel diagonal inertia matrix, $[L]_{3xn}$ is the reaction wheel distribution matrix (chapter 3.4), and $\omega_w = [\omega_{w1} \ \omega_{w2} \dots \ \omega_{wn}]^T$ is the angular speed of the wheels. n is the total number of reaction wheels.

From the Euler's moment equations represented by the angular momentum rate with respect to the body frame, the following dynamics of the satellite can be described [9]:

$$\frac{d}{dt}H_b = -\omega_b(t) \times H_b(t) + T_d(t) \tag{3.10}$$

where T_d represents disturbance torques.

From equation (3.8), the following can be derived:

$$\dot{H}_b = \left[\frac{dH}{dt}\right]_b = I\frac{d\omega_b}{dt} + \dot{h}_w \tag{3.11}$$

Equating equations (3.10) and (3.11) :

$$I\frac{d\omega_b}{dt} = -\omega_b(t) \times H_b(t) + T_d(t) - \dot{h}_w \tag{3.12}$$

By substituting equation (3.8) into (3.12):

$$\frac{d\omega_b}{dt} = I^{-1}[-\omega_b(t) \times (I\omega_b + h_w) + T_d(t) - \dot{h}_w] \tag{3.13}$$

The reaction wheels work on the principle of momentum exchange, therefore the angular momentum produced by reaction wheels is transferred to the satellite with opposite sign, i.e.

$$\dot{h_w} = -T_c \tag{3.14}$$

where T_c is the command torque, which is determined by the controllers.

By substituting (3.14) into (3.13), the following dynamics equation can be found:

$$\frac{d\omega_b}{dt} = I^{-1}[-\omega_b(t) \times (I\omega_b + h_w) + T_d + T_c] \tag{3.15}$$

3.3 Disturbance Torques

The satellites are exposed to several different external disturbance torques in space. The disturbance torques mentioned in literature are gravity gradient torques, aerodynamic drag, solar radiation and magnetic torques. Among these disturbances, aerodynamic drag is considerable for satellites in orbits lower that 500 km. The gravity gradient torque results from a non-symmetric satellite due to the small difference in gravitational attraction from one end of the satellite to the other.[6]

These external torques are mostly negligible compared to control torques from the reaction wheels. Throughout the report, only gravity gradient torque will be considered as disturbance torques:

$$T_d = T_{gg} \tag{3.16}$$

According to [6], the gravity gradient torque can be described as:

$$T_{gg} = 3\omega_o{}^2 c_3 \times I c_3 \tag{3.17}$$

where I is the ineria matrix of the satellite and ω_o represents the angular velocity of the orbit frame about its y_o axis. c_3, which is the unit vector toward nadir, is the third column of the rotation matrix R_o^b and transforms the z_b axis to z_o axis. ω_o and c_3 can be defined as follows:

$$\omega_o{}^2 = \frac{\mu}{r_c^3}, \qquad c_3 = \begin{bmatrix} 2(\varepsilon_1\varepsilon_3 - \varepsilon_2\eta) \\ 2(\varepsilon_2\varepsilon_3 + \varepsilon_1\eta) \\ 1 - 2(\varepsilon_1^2 + \varepsilon_2^2) \end{bmatrix} \tag{3.18}$$

where $\mu = 3.986x10^{14} \ m^3/s^2$ is the Earth's gravitational coefficient and r_c is the distance from the center of Earth.

3.4 Reaction Wheel Distribution Matrix

The distribution matrix of reaction wheels, which is uniquely decided by reaction wheel configuration, consists of n columns corresponding to n reaction wheels. Each column vector represents the distribution of the reaction wheel torques on to the axes of rotation of the satellite.

3.4.1 Standard Orthogonal 3-wheel Configuration

If T_1, T_2, T_3 represent the torques produced by each reaction wheel, then the moments acted on the satellite can be defined as:

$$\begin{bmatrix} T_x \\ T_y \\ T_z \end{bmatrix} = L_{3x3} \begin{bmatrix} T_1 \\ T_2 \\ T_3 \end{bmatrix} \tag{3.19}$$

The distribution matrix of standard orthogonal 3-wheel configuration can be defined as:

$$L = \begin{bmatrix} 1 & 0 & 0 \\ 0 & 1 & 0 \\ 0 & 0 & 1 \end{bmatrix} \tag{3.20}$$
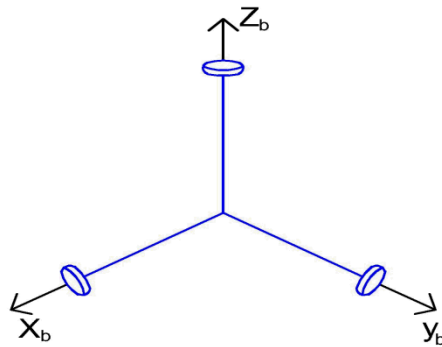
Figure 3.1 – Standard orthogonal 3-wheel configuration

3.4.2 Pyramid Configuration

If T_1, T_2, T_3, T_4 represent the torques produced by each reaction wheel, then the moments acted on the satellite can be defined as:

$$\begin{bmatrix} T_x \\ T_y \\ T_z \end{bmatrix} = L_{3x4} \begin{bmatrix} T_1 \\ T_2 \\ T_3 \\ T_4 \end{bmatrix} \tag{3.21}$$

The general form of the distribution matrix L_{3x4} for 4-wheel configurations can be defined as:

$$L = [c^1 \quad c^2 \quad c^3 \quad c^4] = \begin{bmatrix} c_x^1 & c_x^2 & c_x^3 & c_x^4 \\ c_y^1 & c_y^2 & c_y^3 & c_y^4 \\ c_z^1 & c_z^2 & c_z^3 & c_z^4 \end{bmatrix} \qquad (3.22)$$
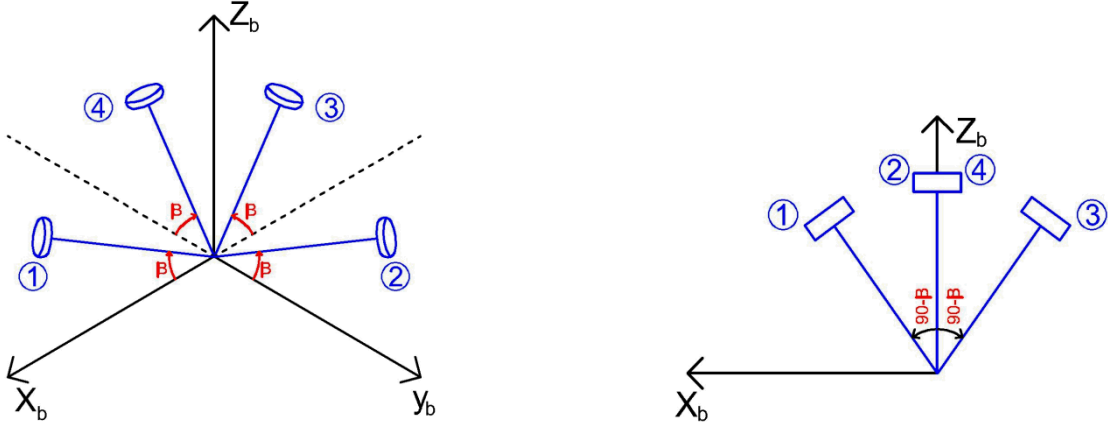
Figure 3.2 - The pyramid configuration of four reaction wheels

The pyramid configuration of reaction wheels is demonstrated in Figure 3.2. The relation between each reaction wheel torque T_1, T_2, T_3, T_4 and the torques produced along the three body axes of the satellite T_x, T_y, T_z can be shown as:

$$T_x = T_1 cos\beta - T_3 cos\beta \qquad (3.23)$$

$$T_y = T_2 cos\beta - T_4 cos\beta \qquad (3.24)$$

$$T_z = T_1 sin\beta + T_2 sin\beta + T_3 sin\beta + T_4 sin\beta \qquad (3.25)$$

Therefore, the distribution matrix becomes:

$$L = \begin{bmatrix} cos\beta & 0 & -cos\beta & 0 \\ 0 & cos\beta & 0 & -cos\beta \\ sin\beta & sin\beta & sin\beta & sin\beta \end{bmatrix} \qquad (3.26)$$
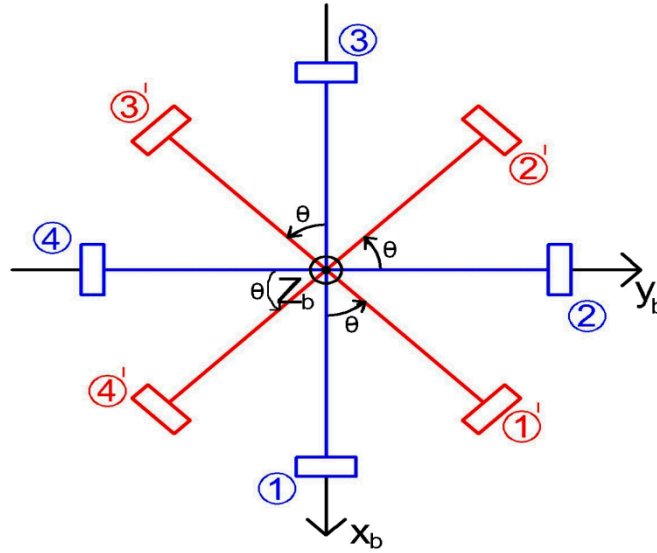
Figure 3.3 – Pyramid configuration rotation about z_b axis by an angle of Θ

When the pyramid configuration is rotated by an angle Θ around z_b axis as shown in Figure 3.3, the distribution matrix becomes:

$$L = \begin{bmatrix} cos\beta cos\Theta & -cos\beta sin\Theta & -cos\beta cos\Theta & cos\beta sin\Theta \\ cos\beta sin\Theta & cos\beta cos\Theta & -cos\beta sin\Theta & -cos\beta cos\Theta \\ sin\beta & sin\beta & sin\beta & sin\beta \end{bmatrix} \tag{3.27}$$

If the angles are selected as $\Theta = 45^o$ and $\beta = 35.264^o$, the following homogenous distribution matrix can be found:

$$L = \begin{bmatrix} \sqrt{3}/3 & -\sqrt{3}/3 & -\sqrt{3}/3 & \sqrt{3}/3 \\ \sqrt{3}/3 & \sqrt{3}/3 & -\sqrt{3}/3 & -\sqrt{3}/3 \\ \sqrt{3}/3 & \sqrt{3}/3 & \sqrt{3}/3 & \sqrt{3}/3 \end{bmatrix} \tag{3.28}$$

3.4.3 Tetrahedron Configuration

The advantage of this configuration is that the wheel assembly can provide twice as much of maximum torque on an axis that a single wheel can provide. [5] Determining the distribution matrix for the tetrahedron configuration is cumbersome relative to pyramid configuration. We may rewrite the distribution matrix as follows:

$$L = \begin{bmatrix} c^1 & c^2 & c^3 & c^4 \end{bmatrix} = \begin{bmatrix} c_x^1 & c_x^2 & c_x^3 & c_x^4 \\ c_y^1 & c_y^2 & c_y^3 & c_y^4 \\ c_z^1 & c_z^2 & c_z^3 & c_z^4 \end{bmatrix} \tag{3.29}$$

Each column vector in distribution matrix is a unit vector, therefore:

$$\sqrt{(c_x^i)^2 + (c_y^i)^2 + (c_z^i)^2} = 1, \quad i=1,2,3,4 \tag{3.30}$$

19

The dot product between two column vectors can be defined as:

$$c^i c^j = |c^i||c^j|\cos\alpha, \qquad |c^i| = |c^j| = 1 \tag{3.31}$$

The angle between the actuators in tetrahedral formation, as shown in Figure 3.4, is given as (Appendix B):

$$\alpha = \cos^{-1}\left(-\frac{1}{3}\right) = 109.47^o \tag{3.32}$$
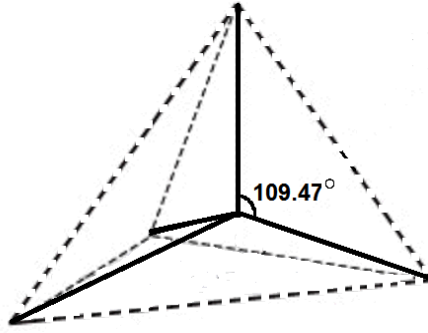
Figure 3.4 – Tetrahedral formation angle

According to [5], the distribution matrix (3.29) satisfies the following equations for each row:

$$c_x^1 + c_x^2 + c_x^3 + c_x^4 = 0 \tag{3.33}$$

$$c_y^1 + c_y^2 + c_y^3 + c_y^4 = 0 \tag{3.34}$$

$$c_z^1 + c_z^2 + c_z^3 + c_z^4 = 0 \tag{3.35}$$

These equations imply that if all four wheels provide equal torque, the total moments in body axes are zero.
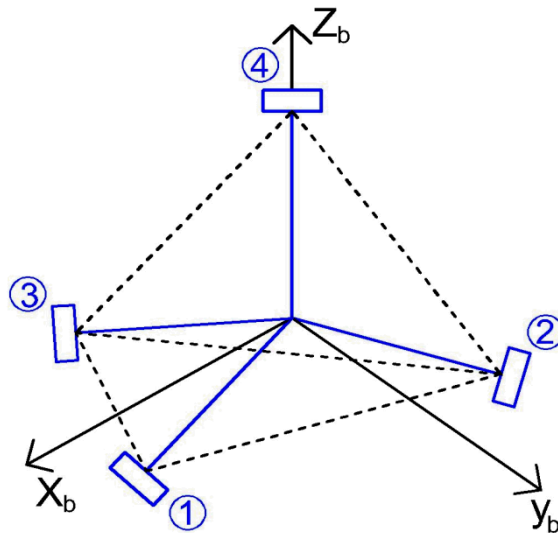
Figure 3.5 – Tetrahedron configuration of four reaction wheels
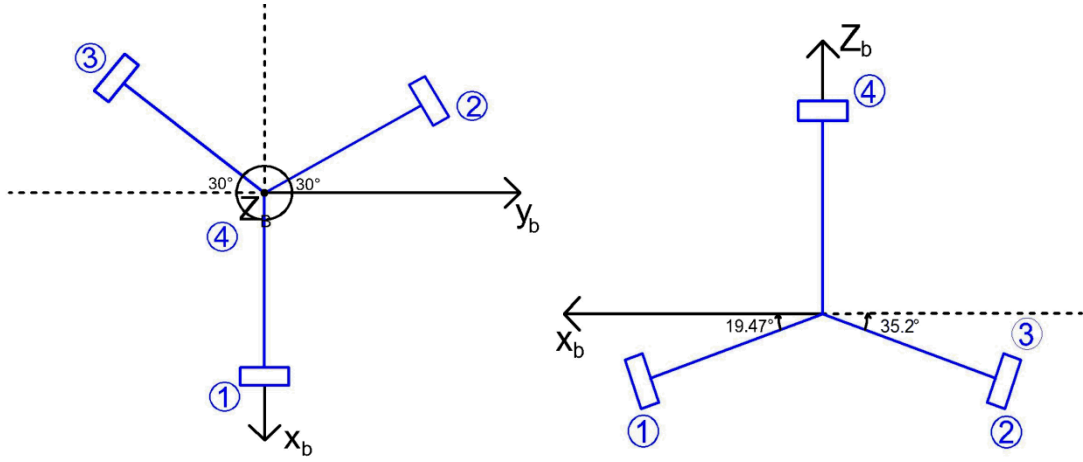
Figure 3.6 – Tetrahedron configuration of four reaction wheels on x_b-y_b and x_b-z_b planes

In Figure 3.5 and Figure 3.6, one possible tetrahedron configuration relative to body frame is demonstrated. Wheels 1, 2 and 3 makes 19.47^o angle with x_b-y_b plane. From Figure 3.6, the relation between each reaction wheel torque T_1, T_2, T_3, T_4 and the torques produced along the three body axes of the satellite T_x, T_y, T_z can be derived as:

$$T_x = T_1 \cos(19.47) - T_2 \cos(19.47) \cos(60) - T_3 \cos(19.47) \cos(60) \qquad (3.36)$$

$$T_y = T_2 \cos(19.47) \cos(30) - T_3 \cos(19.47) \cos(30) \qquad (3.37)$$

$$T_z = -T_1 \sin(19.47) - T_2 \sin(19.47) - T_3 \sin(19.47) + T_4 \qquad (3.38)$$

Therefore, the distribution matrix becomes:

$$L = \begin{bmatrix} \cos(19.47) & -\cos(19.47)\cos(60) & -\cos(19.47)\cos(60) & 0 \\ 0 & \cos(19.47)\cos(30) & -\cos(19.47)\cos(30) & 0 \\ -\sin(19.47) & -\sin(19.47) & -\sin(19.47) & 1 \end{bmatrix} \qquad (3.39)$$

which satisfies the conditions from (3.30) to (3.35).

In the case of distribution matrix derived in (3.39), the zeros indicate that some wheels do not have a contribution of torque on some body axes. To change this, the tetrahedron structure can simply be rotated in any direction relative to body frame. As an example, the tetrahedron structure can be rotated along z_b axis by an angle of Θ, which is shown in Figure 3.7. The relations between reaction wheel torques and the torques produced along the three body axes of the satellite can be derived as:

$$T_x = T_1 \cos(19.47) cos\theta - T_2 \cos(19.47) \cos(60 - \theta) - T_3 \cos(19.47) \cos(60 + \theta) \qquad (3.40)$$

$$T_y = T_1 \cos(19.47) sin\theta + T_2 \cos(19.47) \cos(30 + \theta) - T_3 \cos(19.47) \cos(30 - \theta) \qquad (3.41)$$

$$T_z = -T_1 \sin(19.47) - T_2 \sin(19.47) - T_3 \sin(19.47) + T_4 \qquad (3.42)$$
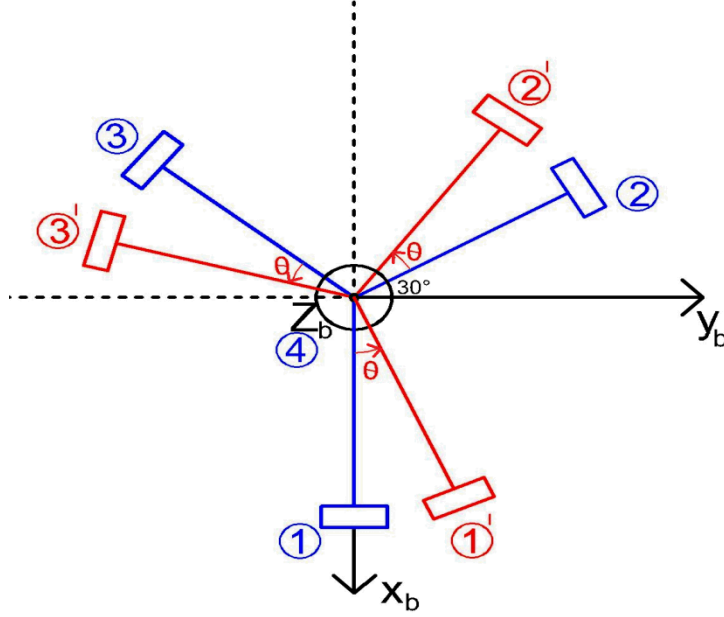
Figure 3.7 – Tetrahedron configuration rotation about z_b axis by an angle of ϴ

The resulting distribution matrix is:

$$L = \begin{bmatrix} \cos(19.47)\cos\theta & -\cos(19.47)\cos(60-\theta) & -\cos(19.47)\cos(60+\theta) & 0 \\ \cos(19.47)\sin\theta & \cos(19.47)\cos(30+\theta) & -\cos(19.47)\cos(30-\theta) & 0 \\ -\sin(19.47) & -\sin(19.47) & -\sin(19.47) & 1 \end{bmatrix} \quad (3.43)$$

It is clear that the wheel on the z_b axis, as a matter of course, does not have any torque contribution to other body axes. To change this, the structure also needs to be rotated along x_b and y_b axes. The following is one possible homogenous distribution matrix for tetrahedron configuration (Appendix B):

$$L = \begin{bmatrix} \sqrt{3}/3 & -\sqrt{3}/3 & -\sqrt{3}/3 & \sqrt{3}/3 \\ \sqrt{3}/3 & -\sqrt{3}/3 & \sqrt{3}/3 & -\sqrt{3}/3 \\ \sqrt{3}/3 & \sqrt{3}/3 & -\sqrt{3}/3 & -\sqrt{3}/3 \end{bmatrix} \quad (3.44)$$

3.5 Control Allocation

The controllers, which are mentioned in Chapter 4, provide the torques that need to be applied on satellite along three body axes. The attitude control by four reaction wheels is an overactuated system control, because three torques along three body axes need to be provided by four reaction wheels. In other words, the system has more actuators (r=4) than the degrees of freedom (n=3). The control problem is to find an cost effective torque distribution among the reaction wheels.

According to [5], a generalized force vector 'τ' needs to be distributed to input vector 'u'. The relation between generalized force vector and input vector is shown as:

$$\tau = T(\alpha) \underbrace{Ku}_{f} \tag{3.45}$$

where $\alpha \in \mathbb{R}^p$ and $u \in \mathbb{R}^r$ are defined as

$$\alpha = [\alpha_1, \dots, \alpha_p]^T, \quad u = [u_1, \dots, u_r]^T \tag{3.46}$$

$f = Ku \in \mathbb{R}^r$ is defined as a force vector, where K is a diagonal matrix $K = diag\{K_1, \dots, K_r\}$.

Allocation matrix is defined as

$$T(\alpha) = [t_1, \dots, t_r], \qquad T(\alpha) \in \mathbb{R}^{nxr}, \ t_i \in \mathbb{R}^n \tag{3.47}$$

According to [5], the generalized force vector 'τ' is distributed to input vector 'u' by minimizing the force vector $f = Ku$ as follows [5]:

$$J = min\{f^T W f\} \tag{3.48}$$

$$\tau - Tf = 0 \tag{3.49}$$

$$f = \underbrace{W^{-1}T^T(TW^{-1}T^T)^{-1}}_{T_w^\dagger} \tau \tag{3.50}$$

where W is a diagonal positive definite matrix and the matrix $T_w^\dagger = W^{-1}T^T(TW^{-1}T^T)^{-1}$ is called the generalized inverse matrix. If $W = I$ (unity matrix), all actuators get equal weight and the generalized inverse is reduced to *Moore-Penrose pseudo inverse* (Appendix D):

$$T_w^\dagger = T^T(TT^T)^{-1} \tag{3.51}$$

Therefore, from equation (3.45), the generalized force vector 'τ' is distributed to actuator input vector 'u' as follows:

$$u = K^{-1}T_w^\dagger \tau \tag{3.52}$$

This command is used to determine control signal for each reaction wheel torques which are applied to satellite dynamic equations. In simulation the following MATLAB function, which is formed by Thor I. Fossen for the allocation problem, is used in simulation as:

$$u = ucalloc(K, T, W, tau) \tag{3.53}$$

3.6 Electrical Model of Reaction Wheels

The reaction wheels are driven by brushless DC motors, which have parameters like inductance 'L_a', armature resistance 'R_a', current 'i_a', back EMF 'e_a', voltage 'u_a', as shown in Figure 3.8.
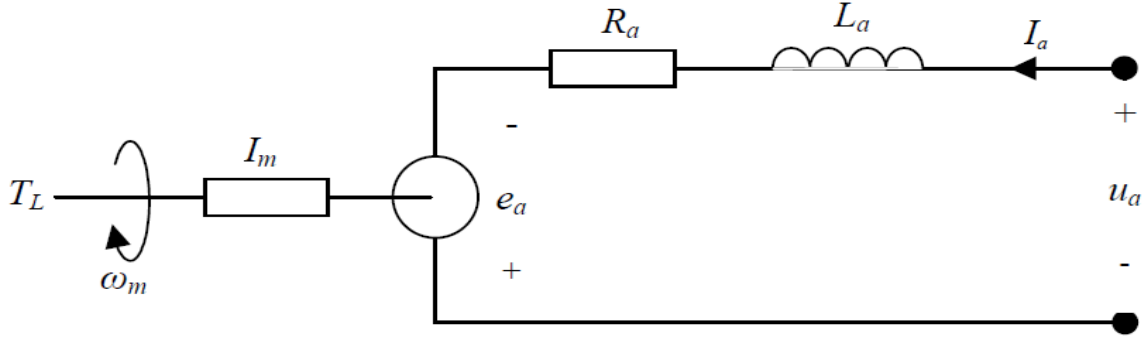
Figure 3.8 – Circuit diagram of a DC motor (Credits: [6])

From the Kirchoff's voltage law for the armature circuit, the following equation can be derived [6]:

$$L_a \frac{di_a}{dt} + R_a i_a - e_a = u_a \tag{3.54}$$

The torque produced by a DC-motor is proportional to the armature current 'i_a' as follows:

$$T = K_T i_a \tag{3.55}$$

where 'K_T' is the torque constant of the DC-motor.

The back EMF, according to Faraday's law of inductance, is as follows:

$$e_a = K_V \omega_m \tag{3.56}$$

where 'K_V' is the voltage constant of the DC-motor and 'ω_m' is the angular velocity of the rotor shaft.

The workload of the DC-motor consists of a reaction wheel mounted on the rotor shaft, resulting in the following workload torque:

$$T_L = I_w \dot{\omega}_w \tag{3.57}$$

where I_w is the moment of inertia of the wheel and ω_w is the angular velocity of the wheel. The rotor shaft of the motor, as a matter of course, has the same angular velocity and acceleration with the reaction wheel which is fixed to the rotor shaft. Therefore $\omega_w = \omega_m$ and $\dot{\omega}_w = \dot{\omega}_m$. The moment balance of the rotor shaft is given as [6]:

24

$$I_m \dot{\omega}_m = T - T_L \tag{3.58}$$

Substituting equation (3.57) into (3.58), with the fact that $\dot{\omega}_w = \dot{\omega}_m$ results in:

$$(I_m + I_w)\dot{\omega}_w = T \tag{3.59}$$

It is acceptable to assume that $I_w \gg I_m$ while the reaction wheel is added to the system to increase the moment of inertia. As a result, the following relation can be derived:

$$T = I_w \dot{\omega}_w \tag{3.60}$$
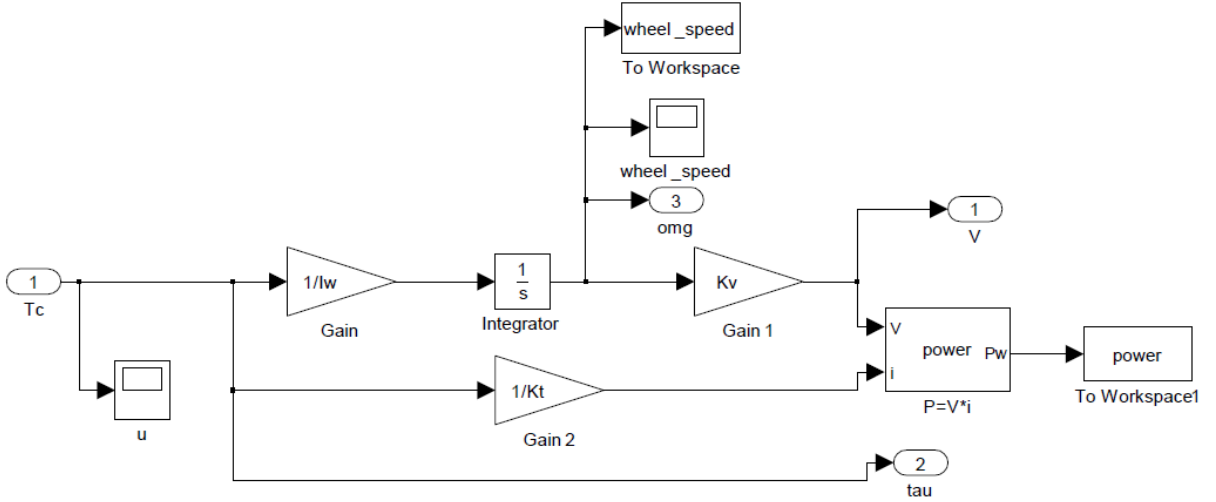
Figure 3.9 – DC-motor simulation block

In simulation, to keep the system simple, the settling time of the DC-motor is assumed to be negligible compared to maneuvers of the satellite. First, from the torque command to the motor, angular velocity of the rotor shaft is calculated from equation (3.60). Then, the voltage that needs to be applied to motor is calculated from the equation (3.56). The DC-motor block of the simulation is shown in Figure 3.9.

The power input to the DC-motors can be calculated as follows:

$$P_{in} = V \cdot i \tag{3.61}$$

In Appendix-A datasheet of a brushless DC servomotor is provided, from which some parameters for the simulation are used.

Chapter 4

Control Strategies

This chapter provides definitions and derivations of one linear and two non-linear control algorithms. First, reference trajectory that is employed with controllers is defined. Then, in sequence, LQR controller, Sliding Mode Controller and Integrator Backstepping Controller are presented.

4.1 Reference Trajectory

The reference model takes the step input and provides a smooth transition curve.[6] Tracking regulators rely on having a continuous and differentiable trajectory. In this thesis, a second-order filter for the reference model is employed, expressed as:

$$\frac{q_d}{q_r} = \frac{\omega_n^2}{s^2 + 2\zeta\omega_n + \omega_n^2} \tag{4.1}$$

where q_d is the desired quaternion and q_r is the reference quaternion, ω_n is the cross-over frequency and ζ is the relative damping factor. By adjusting the parameters ω_n and ζ, the desired response of the system can be achieved. The relative damping factor is selected as $\zeta = 1$, which leads to a critically damped output signal from the reference model.

4.2 Linear Quadratic Regulator (LQR) Controller

This control system is based on quaternion-feedback PD controller that is using a gain matrix which is determined by LQR algorithm.

The quaternion error, which is the difference between the attitude at some time and the reference attitude, can be derived as follows [9]:

$$\begin{bmatrix} q_{1e} \\ q_{2e} \\ q_{3e} \\ q_{4e} \end{bmatrix} = \begin{bmatrix} q_{4c} & q_{3c} & -q_{2c} & -q_{1c} \\ -q_{3c} & q_{4c} & q_{1c} & -q_{2c} \\ q_{2c} & -q_{1c} & q_{4c} & -q_{3c} \\ q_{1c} & q_{2c} & q_{3c} & q_{4c} \end{bmatrix} \begin{bmatrix} q_1 \\ q_2 \\ q_3 \\ q_4 \end{bmatrix} \tag{4.2}$$

where $q_{1c,..,4c}$ represents the reference quaternion and $q_{1,..,4}$ represents the measured quaternion.

The rate of change of quaternion error is given as:

$$\dot{q}_e = \frac{1}{2} \begin{bmatrix} q_{e4} & -q_{e3} & q_{e2} \\ q_{e3} & q_{e4} & -q_{e1} \\ -q_{e2} & q_{e1} & q_{e4} \\ -q_{e1} & -q_{e2} & -q_{e3} \end{bmatrix} \begin{bmatrix} \omega_{b1} \\ \omega_{b2} \\ \omega_{b3} \\ 0 \end{bmatrix} \tag{4.3}$$

where $\omega_b = [\omega_{b1}\ \omega_{b2}\ \omega_{b3}]^T$ is the angular velocity in body frame. From equation (3.15), the dynamics equation can be rewritten as follows:

$$\dot{\omega}_b = I^{-1}[-\omega_b(t) \times (I\omega_b + h_w) + T_d + T_c] \tag{4.4}$$

A quaternion feedback PD control scheme can be defined as follows:

$$T_{cx} = -k_{q1}q_{1e} - k_{\omega1}\omega_{b1} \tag{4.5}$$

$$T_{cy} = -k_{q2}q_{2e} - k_{\omega2}\omega_{b2} \tag{4.6}$$

$$T_{cz} = -k_{q3}q_{3e} - k_{\omega3}\omega_{b3} \tag{4.7}$$

where $T_c = [T_{cx}\ T_{cy}\ T_{cz}]^T$ is the command torque vector and k values are feedback coefficients. To apply a linear control algorithm, the system needs to be linearized. The following is the standard form of a linear state space system:

$$\dot{x}(t) = f(x, u, t) = Ax(t) + Bu(t) \tag{4.8}$$

$$y(t) = Cx(t) + Du(t) \tag{4.9}$$

where $x(t) = [q_{e1}\ q_{e2}\ q_{e3}\ \omega_{b1}\ \omega_{b2}\ \omega_{b3}]^T$ is the state vector of the system and $u(t) = [T_{cx}\ T_{cy}\ T_{cz}]^T$ is the control signal vector.

The linearized system matrices can be derived as follows:

$$A = \begin{bmatrix} \frac{\partial f_1}{\partial x_1} & \cdots & \frac{\partial f_1}{\partial x_n} \\ \vdots & \cdots & \vdots \\ \frac{\partial f_n}{\partial x_1} & \cdots & \frac{\partial f_n}{\partial x_n} \end{bmatrix} \qquad B = \begin{bmatrix} \frac{\partial f_1}{\partial u_1} & \cdots & \frac{\partial f_1}{\partial u_m} \\ \vdots & \cdots & \vdots \\ \frac{\partial f_n}{\partial u_1} & \cdots & \frac{\partial f_n}{\partial u_m} \end{bmatrix} \tag{4.10}$$

The system can be linearized at $q_0 = [0\ 0\ 0\ 1]^T$ and $\omega_0 = [0\ 0\ 0]^T$ as follows [9]:

$$A = \begin{bmatrix} \frac{\partial \dot{q}_e}{\partial q_e} & \frac{\partial \dot{q}_e}{\partial \omega_b} \\ \frac{\partial \dot{\omega}_b}{\partial q_e} & \frac{\partial \dot{\omega}_b}{\partial \omega_b} \end{bmatrix}_{q_0,\ \omega_0} = \begin{bmatrix} [0]_{3x3} & \frac{1}{2}[I]_{3x3} \\ [0]_{3x3} & I^{-1}S(h_w) \end{bmatrix} \tag{4.11}$$

$$B = \begin{bmatrix} \frac{\partial \dot{q}_e}{\partial T_c} \\ \frac{\partial \dot{\omega}_b}{\partial T_c} \end{bmatrix}_{q_0,\ \omega_0} = \begin{bmatrix} [0]_{3x3} \\ I^{-1} \end{bmatrix} \tag{4.12}$$

$$C = \begin{bmatrix} 1 & \cdots & 0 \\ \vdots & \ddots & \\ 0 & & 1 \end{bmatrix}_{6x6}, \qquad D = 0 \tag{4.13}$$

where $[I]_{3x3}$ is an identity matrix, I^{-1} is inverse of moment of inertia matrix and where S(.) is the cross-product operator.

The aim is to find a state-variable feedback control defined as follows [10]:

$$u(t) = -Kx(t) \tag{4.14}$$

where K is the feedback gain matrix. To find the control signal $'u'$ that minimizes the cost function, the following performance index (PI) is defined:

$$J(x,u) = \frac{1}{2}\int_0^\infty (x^T Q x + u^T R u)dt \tag{4.15}$$

Substituting (4.14) into this equation yields:

$$J = \frac{1}{2}\int_0^\infty x^T (Q + K^T R K)xdt \tag{4.16}$$

The performance index J can be interpreted as an energy function such that keeping it small minimizes the total energy of the closed-loop system. If J is minimized, and since it is an infinite integral of x(t), then x(t) goes to zero as t goes to infinity. This in turn guarantees that the closed-loop system is stable. [11]

The feedback gain matrix K has the form [10]:

$$K = R^{-1}B^T P \tag{4.17}$$

where P is the solution of algebraic Riccati equation:

$$A^T P + PA + Q - PBR^{-1}B^T P = 0 \tag{4.18}$$

The Q and R are defined as state and control weighting matrices. The selection of Q and R matrices are performed by adjusting them in simulations until the desired performance is achieved.

There are several procedures for solving algebraic Riccati equation. The feedback gain matrix K can be calculated in MATLAB using the following command:

$$K = lqr(A, B, Q, R) \tag{4.19}$$

4.3 Sliding Mode Controller

The Sliding Mode Controller tries to bring the system states to a manifold or surface where the states stay in that manifold as time goes to infinity. Once the system states are in the manifold, they converge to desired states. [18]

Equation (4.3) can be modified as follows:

$$\dot{\bar{q}}_e = \frac{1}{2} \begin{bmatrix} q_{e4} & -q_{e3} & q_{e2} \\ q_{e3} & q_{e4} & -q_{e1} \\ -q_{e2} & q_{e1} & q_{e4} \end{bmatrix} \begin{bmatrix} \omega_{bo1} \\ \omega_{bo2} \\ \omega_{bo3} \end{bmatrix} = \frac{1}{2} T(q_e) \omega_{bo} \tag{4.20}$$

The sliding surface is selected as [12]:

$$S = \omega_{bo} + K\bar{q}_e = 0 \tag{4.21}$$

where $\bar{q}_e = [q_{e1} \, q_{e2} \, q_{e3}]$, ω_{bo} denotes the angular velocity of body frame relative to orbit frame, and K is a positive definite diagonal matrix. By multiplying the equation (4.21) by $\frac{1}{2} T(q_e)$:

$$\frac{1}{2} T(q_e) \omega_{bo} + \frac{1}{2} T(q_e) K\bar{q}_e = 0 \tag{4.22}$$

Substituting equation (4.20) into (4.22) results in:

$$\dot{\bar{q}}_e + \frac{1}{2} T(q_e) K\bar{q}_e = 0 \tag{4.23}$$

The following Lyapunov function is selected [12]:

$$V_s = \frac{1}{2} S^T S \begin{cases} > 0 & S \neq 0 \\ = 0 & S = 0 \end{cases} \tag{4.24}$$

Differentiating Lyapunov function (4.24) results in:

$$\dot{V}_s = \frac{1}{2} \dot{S}^T S + \frac{1}{2} S^T \dot{S} = S^T \dot{S} \tag{4.25}$$

$$\dot{V}_s = S^T (\dot{\omega}_{bo} + K\dot{\bar{q}}_e) \tag{4.26}$$

Substituting equation (3.15) into (4.26) results in:

$$\dot{V}_s = S^T I^{-1} (-\omega_{bo} \times (I\omega_{bo} + h_w) + u + T_d + IK\dot{\bar{q}}_e) \tag{4.27}$$

Considering (4.27), the control law is selected as:

$$u = \omega_{bo} \times (I\omega_{bo} + h_w) - T_d - I\dot{\omega}_{bo} - IK\dot{\bar{q}}_e - IGsgn(S) \tag{4.28}$$

Substituting (4.28) into (4.27):

$$\dot{V}_s = -S^T (\dot{\omega}_{bo} + Gsgn(S)) \tag{4.29}$$

where G is a positive definite diagonal matrix and $sgn(S) = [sgn(S_1) \, sgn(S_2) \, sgn(S_3)]^T$.

For $G_i > |\dot{\omega}_{boi}|_{max}$ $(i = 1,2,3)$ the stability condition of sliding mode $\dot{V}_s < 0$ is satisfied.[12]
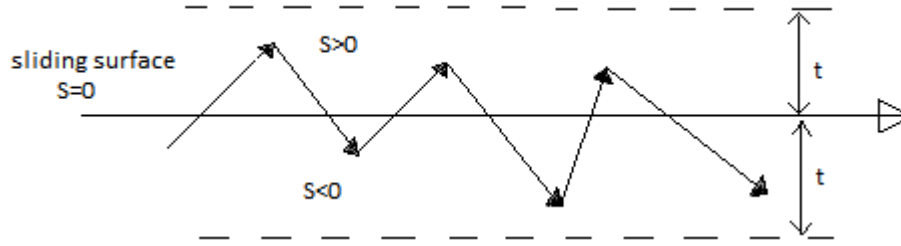
Figure 4.1 – Chattering along the sliding surface

The problem of sliding mode control is the chattering resulting from the sgn(S) function, as can be seen in Figure 4.1. In this case, the system states does not actually achieve the sliding surface, instead they oscillate within sliding thickness value. One common way of dealing with this issue is to replace the sign function with a smooth saturation function, like tanh function, as follows:

$$sat(S) = \tanh\left(\frac{S}{t}\right) \tag{4.30}$$

where t is the sliding thickness.
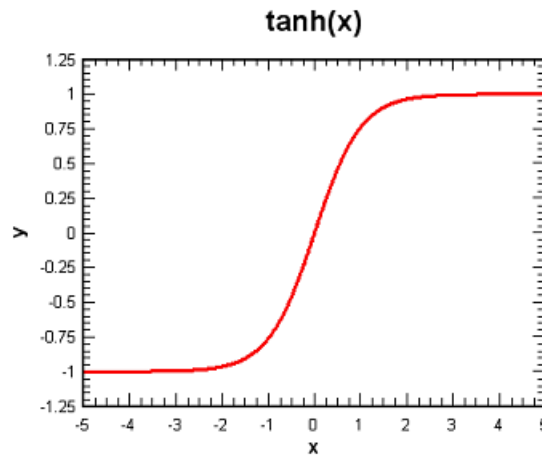
Figure 4.2 – tanh function

4.4 Integrator Backstepping Controller

Integrator Backstepping Control is a quaternion feedback control based on Lyapunov stability theory. The full-plant state vector is partitioned to some sub-levels. The controller stabilizes the entire plant recursively with the use of Lyapunov functions at each level. Cancellation of the nonlinearities at each level guarantees the negative definiteness of Lyapunov function ($\dot{V} < 0$). [13] The control torque is designed for each integrator level, which compensates for destabilizing nonlinearities. [8] In the end, a globally stable closed loop is obtained.

The kinematics equations (3.6) ,(3.7) and the dynamics equations (3.15) can be rewritten as:

$$\dot{\eta} = -\frac{1}{2}\epsilon^T \omega_{bo}^b \tag{4.31}$$

$$\dot{\epsilon} = \frac{1}{2}\eta\omega_{bo}^b - \frac{1}{2}\omega_{bo}^b \times \epsilon \tag{4.32}$$

$$I\dot{\omega}_b = -\omega_b(t) \times (I\omega_b + h_w) + T_d + T_c \tag{4.33}$$

Step 1:

The first virtual state variable z_1 as the attitude tracking error is defined as follows [8]:

$$z_1 = \begin{bmatrix} 1 - |\tilde{\eta}| \\ \tilde{\epsilon} \end{bmatrix} \tag{4.34}$$

$$\begin{bmatrix} \tilde{\eta} \\ \tilde{\epsilon} \end{bmatrix} = \begin{bmatrix} \eta_d \\ \epsilon_d \end{bmatrix} \otimes \begin{bmatrix} \eta \\ -\epsilon \end{bmatrix} = \begin{bmatrix} \eta_d\eta + \epsilon_d^T\epsilon \\ \eta_d\epsilon - \eta\epsilon_d - S(\epsilon_d)\epsilon \end{bmatrix} \tag{4.35}$$

where $\otimes$ denotes quaternion multiplication and S(.) is the cross product operator given by:

$$S(\omega) = \begin{bmatrix} 0 & -\omega_z & \omega_y \\ \omega_z & 0 & -\omega_x \\ -\omega_y & \omega_x & 0 \end{bmatrix} \tag{4.36}$$

Substituting (4.35) into (4.34):

$$z_1 = \begin{bmatrix} 1 - |\eta_d\eta + \epsilon_d^T\epsilon| \\ \eta_d\epsilon - \eta\epsilon_d - S(\epsilon_d)\epsilon \end{bmatrix} \tag{4.37}$$

A virtual control input is defined as:

$$\alpha_1 = \omega_{ob}^b - z_2 \tag{4.38}$$

which forms a link between first and second steps. z_2 is the second back-stepping state vector.

Taking derivative of z_1:

$$\dot{z}_1 = \begin{bmatrix} -sgn(\tilde{\eta}) \left[\eta_d\dot{\eta} + \epsilon_d^T\dot{\epsilon} \right] \\ \eta_d\dot{\epsilon} - \dot{\eta}\epsilon_d - S(\epsilon_d)\dot{\epsilon} \end{bmatrix} \tag{4.39}$$

Substitution of (4.31) and (4.32) into (4.39) results in:

$$\dot{z}_1 = \frac{1}{2}\begin{bmatrix} sgn(\tilde{\eta})[\eta_d\epsilon^T - \epsilon_d^T[\eta I + S(\epsilon)]] \\ [\eta_d I - S(\epsilon_d)][\eta I + S(\epsilon)] + \epsilon_d\epsilon^T \end{bmatrix} \omega_{ob}^b \tag{4.40}$$

Substituting (4.35) and (4.38) :

$$\dot{z}_1 = \frac{1}{2}G^T(\tilde{q})(\alpha_1 + z_2) \tag{4.41}$$

$$\text{where} \quad G^T(\tilde{q}) = \begin{bmatrix} sgn(\tilde{\eta})\tilde{\epsilon} \\ \tilde{\eta}I + S(\tilde{\epsilon}) \end{bmatrix} \tag{4.42}$$

$$sgn(x) = \begin{cases} -1, & x < 0 \\ 1, & x \geq 0 \end{cases} \tag{4.43}$$

A Lyapunov function can be defined as [8]:

$$V_1 = z_1^T z_1 \tag{4.44}$$

$$\dot{V}_1 = 2z_1^T \dot{z}_1 = z_1^T G^T(\tilde{q})(\alpha_1 + z_2) \tag{4.45}$$

The stabilizing function α_1 can be selected as follows:

$$\alpha_1 = -K_1 G(\tilde{q}) z_1 \tag{4.46}$$

where $K_1 = K_1^T > 0$ is a feedback gain matrix. Substituting (4.46) into (4.45):

$$\dot{V}_1 = -z_1^T \underbrace{G^T K_1 G}_{\substack{symmetric \\ positive \\ semidefinite}} z_1 + z_1^T G^T z_2 \tag{4.47}$$

In this equation, the quadratic term related to the variable z_1 is negative definite (with symmetric positive definite inner matrix). The remaining cross term is eliminated in the next step.

Moreover, substituting (4.46) into (4.41) results in following z_1-system:

$$\dot{z}_1 = -\frac{1}{2}G^T K_1 G z_1 + \frac{1}{2}G^T z_2 \tag{4.48}$$

Step 2 :

In the second step, the dynamics related to the second virtual state variable z_2 is stabilized. To do that, the second back - stepping state variable is derived from equations (3.5) and (4.38) as follows:

$$\omega_{ob}^b = \alpha_1 + z_2 = \omega_{ib}^b + \omega_o c_2 \tag{4.49}$$

$$\dot{z}_2 = \dot{\omega}_{ib}^b + \omega_o \dot{c}_2 - \dot{\alpha}_1 \tag{4.50}$$

Multiplying both sides by inertia matrix I :

$$I\dot{z}_2 = I\dot{\omega}_{ib}^b + \omega_o I \dot{c}_2 - I\dot{\alpha}_1 \tag{4.51}$$

Substitution of (4.33) results in:

$$I\dot{z}_2 = T_c + T_d - \omega_{ib}^b \times (I\omega_b + h_w) + \omega_o I \dot{c}_2 - I\dot{\alpha}_1 \tag{4.52}$$

From equation (3.2) the time derivative of the directional cosines can be found as:

$$\dot{c}_i = S(c_i)\omega_{ob}^b \tag{4.53}$$

$$\dot{c}_2 = S(c_2)\omega_{ob}^b = S(c_2)\big[\omega_{ib}^b + \omega_o c_2\big] = S(c_2)\omega_{ib}^b \tag{4.54}$$

Substituting this into (4.52):

$$I\dot{z}_2 = T_c + T_d - \omega_{ib}^b \times (I\omega_b + h_w) + \omega_o IS(c_2)\omega_{ib}^b - I\dot{\alpha}_1 \tag{4.55}$$

The second Lyapunov function V_2 can be defined as [8]:

$$V_2 = V_1 + \frac{1}{2}z_2^T I z_2 \tag{4.56}$$

$$\dot{V}_2 = \dot{V}_1 + z_2^T I \dot{z}_2 \tag{4.57}$$

Substituting (4.47) and (4.55) into (4.57) results in:

$$\dot{V}_2 = -z_1^T G^T K_1 G z_1 + z_1^T G^T z_2 + z_2^T \underbrace{\big[T_c + T_d - \omega_{ib}^b \times (I\omega_b + h_w) + \omega_o IS(c_2)\omega_{ib}^b - I\dot{\alpha}_1\big]}_{[-K_2 z_2 - G z_1]}$$

In this equation, the terms related to the variable z_2 needs to be converted to some negative definite quadratic functions in order to make the dynamics related to z_1 and z_2 globally stable. Therefore, the actuator torque can be selected as:

$$T_c = -K_2 z_2 - G z_1 + \omega_{ib}^b \times (I\omega_b + h_w) - \omega_o IS(c_2)\omega_{ib}^b + I\dot{\alpha}_1 - T_d \tag{4.59}$$

where $K_2 = K_2^T > 0$ is a feedback gain matrix. Substituting this torque command into $\dot{V}_2$ results in:

$$\dot{V}_2 = -z_1^T G^T K_1 G z_1 - z_2^T K_2 z_2 \le 0 \tag{4.60}$$

Therefore, the Lyapunov function provides a stable control law (torque command) with the following closed-loop dynamics:

$$\dot{z}_1 = -\frac{1}{2}G^T K_1 G z_1 + \frac{1}{2}G^T z_2 \tag{4.61}$$

$$I\dot{z}_2 = -K_2 z_2 - G z_1 \tag{4.62}$$

The expressions $-K_2 z_2$ and $\dot{\alpha}_1$ are included in torque command (4.59), which can be defined as :

$$-K_2 z_2 = -K_2\big(\omega_{ob}^b - \alpha_1\big) = -K_2(\omega_{ob}^b + K_1 G(\tilde{q})z_1) \tag{4.63}$$

$$\dot{\alpha}_1 = -K_1\big[\dot{G}(\tilde{q})z_1 + G(\tilde{q})\dot{z}_1\big] \tag{4.64}$$

where $\dot{G}(\tilde{q})$ can be expressed as:

$$\dot{G}(\tilde{q}) = \frac{\partial G}{\partial \eta}\dot{\eta} + \frac{\partial G}{\partial \epsilon}\dot{\epsilon} \tag{4.65}$$

$$\frac{\partial G}{\partial \eta} \dot{\eta} = \begin{bmatrix} -sgn(\tilde{\eta}) \epsilon_d^T \dot{\eta} \\ [\eta_d I - S(\epsilon_d)] \dot{\eta} \end{bmatrix}^T \qquad (4.66)$$

$$\frac{\partial G}{\partial \epsilon} \dot{\epsilon} = \begin{bmatrix} sgn(\tilde{\eta})[\eta_d \dot{\epsilon}^T - \epsilon_d^T[\eta I + S(\dot{\epsilon})]] \\ [\eta_d I - S(\epsilon_d)]S(\dot{\epsilon}) + \epsilon_d \dot{\epsilon}^T \end{bmatrix}^T \qquad (4.67)$$

Chapter 5

Simulations and Results

In this chapter, simulation results of the control strategies mentioned in Chapter 4 with different reaction wheel configurations (e.g. tetrahedron configuration, pyramid configuration, standard orthogonal 3-wheel configuration) are presented and compared. The mathematical models presented in this thesis are implemented in MATLAB/SIMULINK. In simulations, it is assumed that the attitude of the satellite is continuously provided by determination system without errors. Since the real test system is under development, the spacecraft parameters are all assumptions used for comparison purposes between different controllers and different scenarios.

Parameter	Value
Satellite Weight	60 kg
Satellite Inertia Matrix	$\mathrm{diag}(4, 4, 3)$ kgm^2
Orbit	600 km
Reaction wheel inertia	$5x10^{-4}$ kgm^2 (one wheel)

Table 5.1 – Satellite simulation parameters

The simulation results for three different reaction wheel configurations, namely tetrahedron configuration, pyramid configuration and standard 3-axis configuration, are presented. On tetrahedron and pyramid configurations (Figure 5.1), four reaction wheels are employed and failure of one of the wheels is investigated. Standard orthogonal 3-wheel configuration (Figure 5.2) employs three reaction wheels inserted on each body axis.
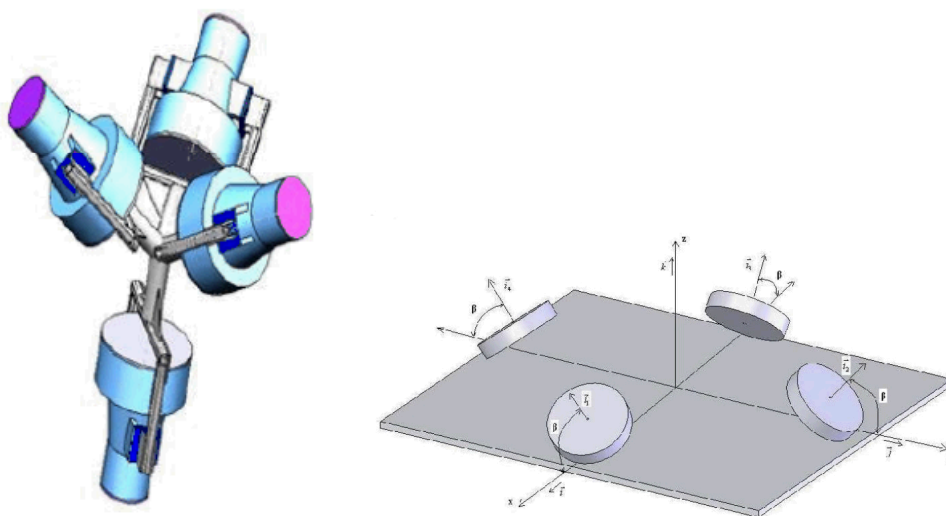
Figure 5.1 - Tetrahedron configuration (left) and Pyramid configuration(right) of reaction wheels (Credits: [5],[14])
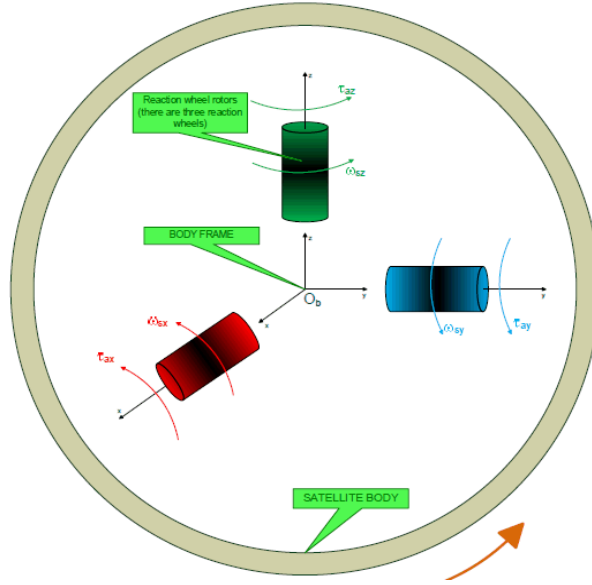
Figure 5.2 – Standard orthogonal 3-wheel configuration (Credits: [13])

In the following sub-chapters, the following reaction wheel distribution matrices are used to get the resulting graphs. Different possible configuration results are also tabulated and compared at the end of this chapter.

For pyramid configuration:

$$L = \begin{bmatrix} cos\beta cos\theta & -cos\beta sin\theta & -cos\beta cos\theta & cos\beta sin\theta \\ cos\beta sin\theta & cos\beta cos\theta & -cos\beta sin\theta & -cos\beta cos\theta \\ sin\beta & sin\beta & sin\beta & sin\beta \end{bmatrix} \quad (5.1)$$

where $\theta = 45^o$, $\beta = 45^o$.

For tetrahedron configuration:

$$L = \begin{bmatrix} cos(19.47)\,cos\theta & -cos(19.47)cos(60-\theta) & -cos(19.47)cos(60+\theta) & 0 \\ cos(19.47)sin\theta & cos(19.47)cos(30+\theta) & -cos(19.47)cos(30-\theta) & 0 \\ -sin(19.47) & -sin(19.47) & -sin(19.47) & 1 \end{bmatrix} \quad (5.2)$$

where $\theta = 0$.

In the following simulations, the noise effects are not considered.

,5.1 Linear Quadratic Regulator (LQR) Simulation Results

Control input for linear quadratic regulator controller is defined in Chapter 4 as:

$$u(t) = -Kx(t) \qquad (5.3)$$

The feedback gain matrix K can be calculated in MATLAB using the following command:

$$K = lqr(A, B, Q, R) \qquad (5.4)$$

which calculates the optimal gain matrix K such that the state-feedback law (5.3) minimizes the quadratic cost function. Controller parameters used in the simulation are given below:

Parameter	Value
Initial Angular Velocity	$\omega_{bo}^{b} = [0\ 0\ 0]^{T}$
Initial Euler Angles	$[\varnothing\ \theta\ \Psi] = [0\ 0\ 0]^{T}$
Control Weighting Matrices	Q = eye(6)
	R = 100*eye(3)
Desired Euler Angles	$[\varnothing\ \theta\ \Psi] = [30\ 20\ 40]^{T}$
Cross-over frequency	$\omega_n = 0.02$
Relative damping factor	$\zeta = 1$
Maximum Wheel Torque	5 mNm

Table 5.2 – Simulation parameters of LQR controller

Implementation of the controller can be shown in flow chart as follows:
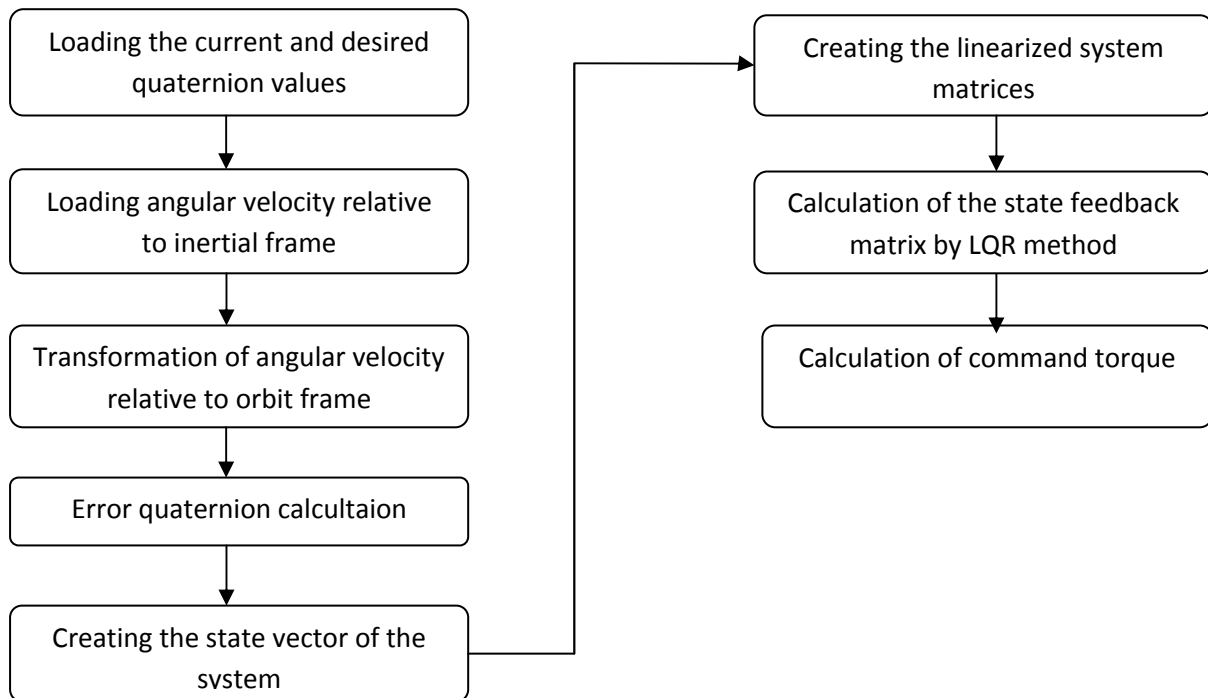
5.1.1 Pyramid Configuration
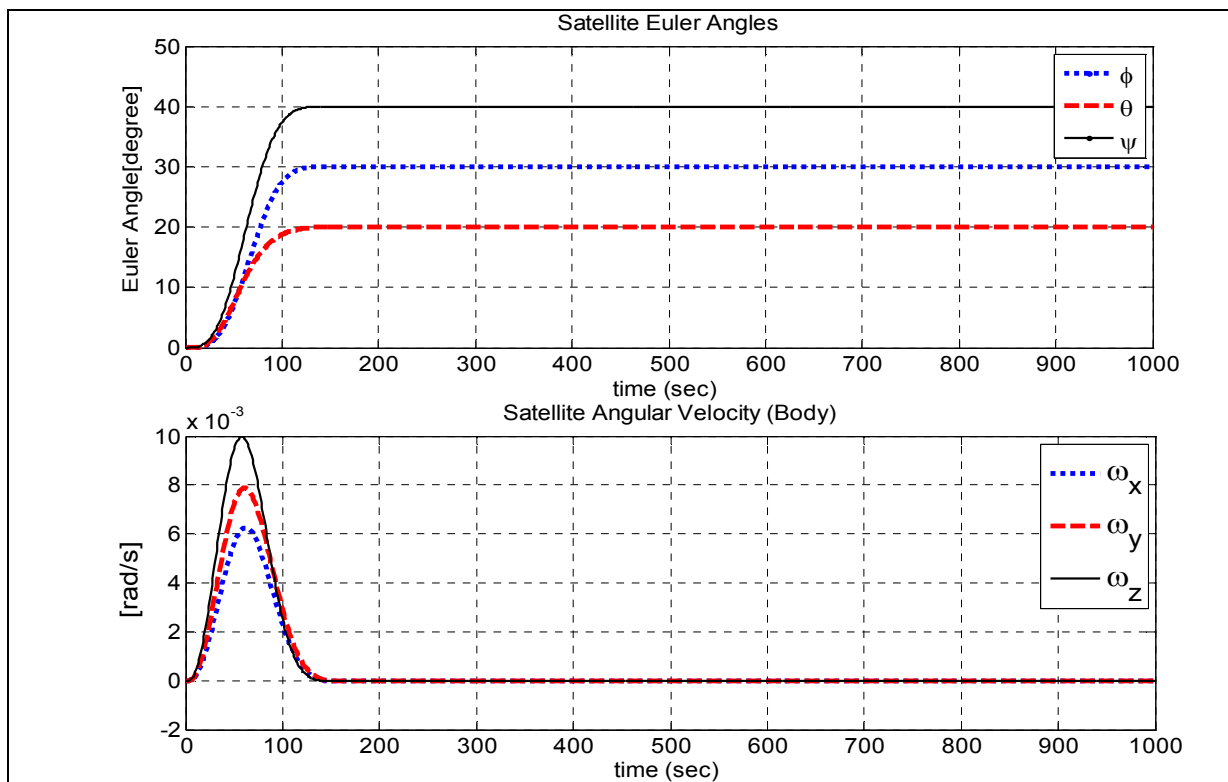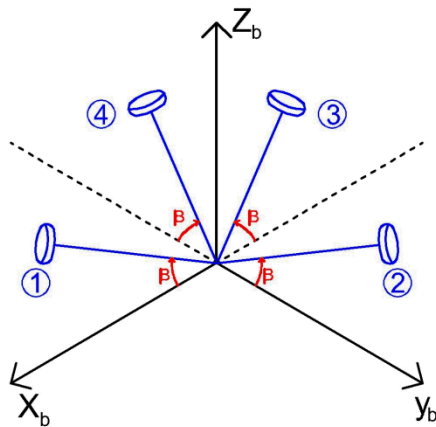
Figure 5.3 – System response of LQR for pyramid configuration

The system reaches to desired Euler angles in 164 seconds. The settling time for the satellite angular velocity is 174 seconds. These values can be modified for different mission requirements by adjusting the control weighting matrices Q and R and/or the cross-over frequency ω_n.
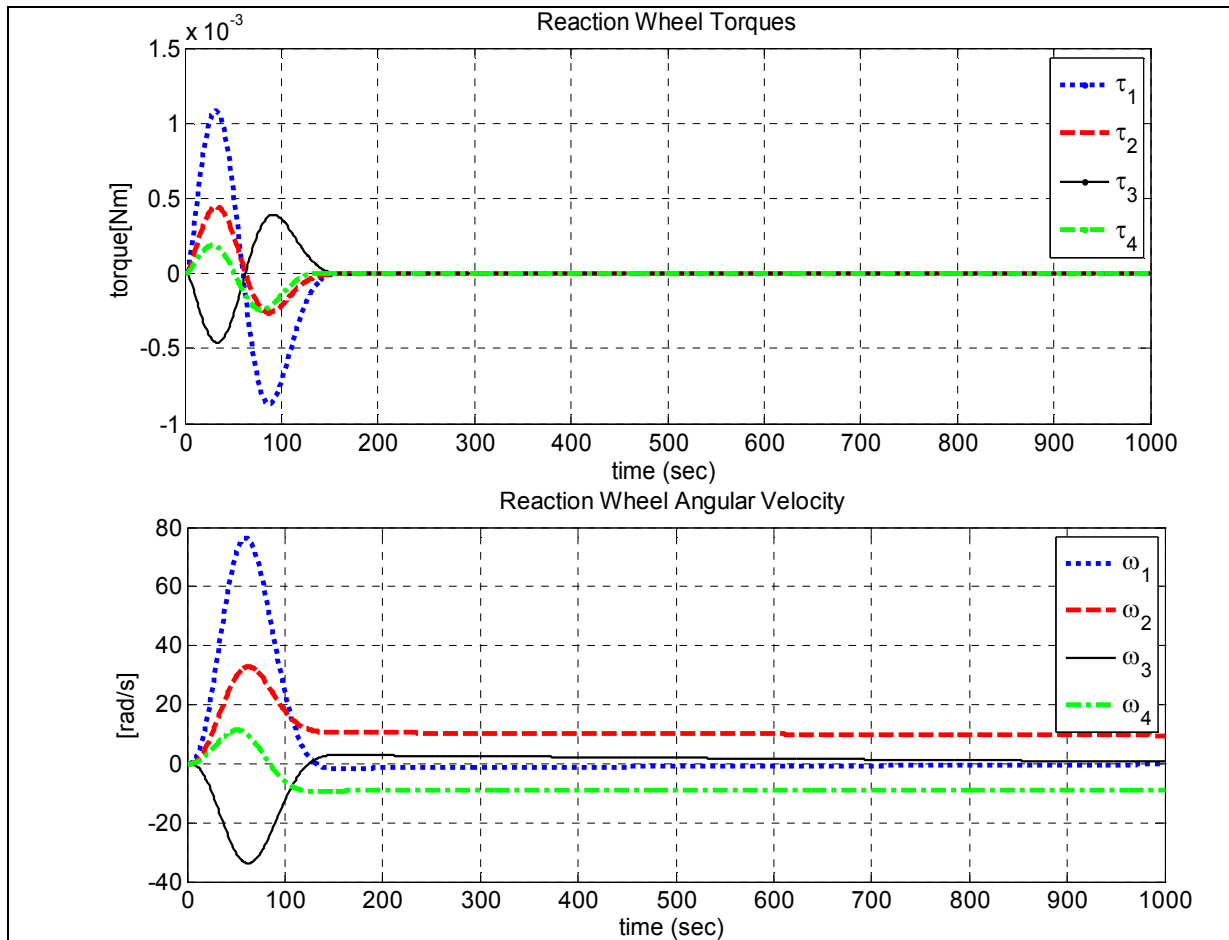
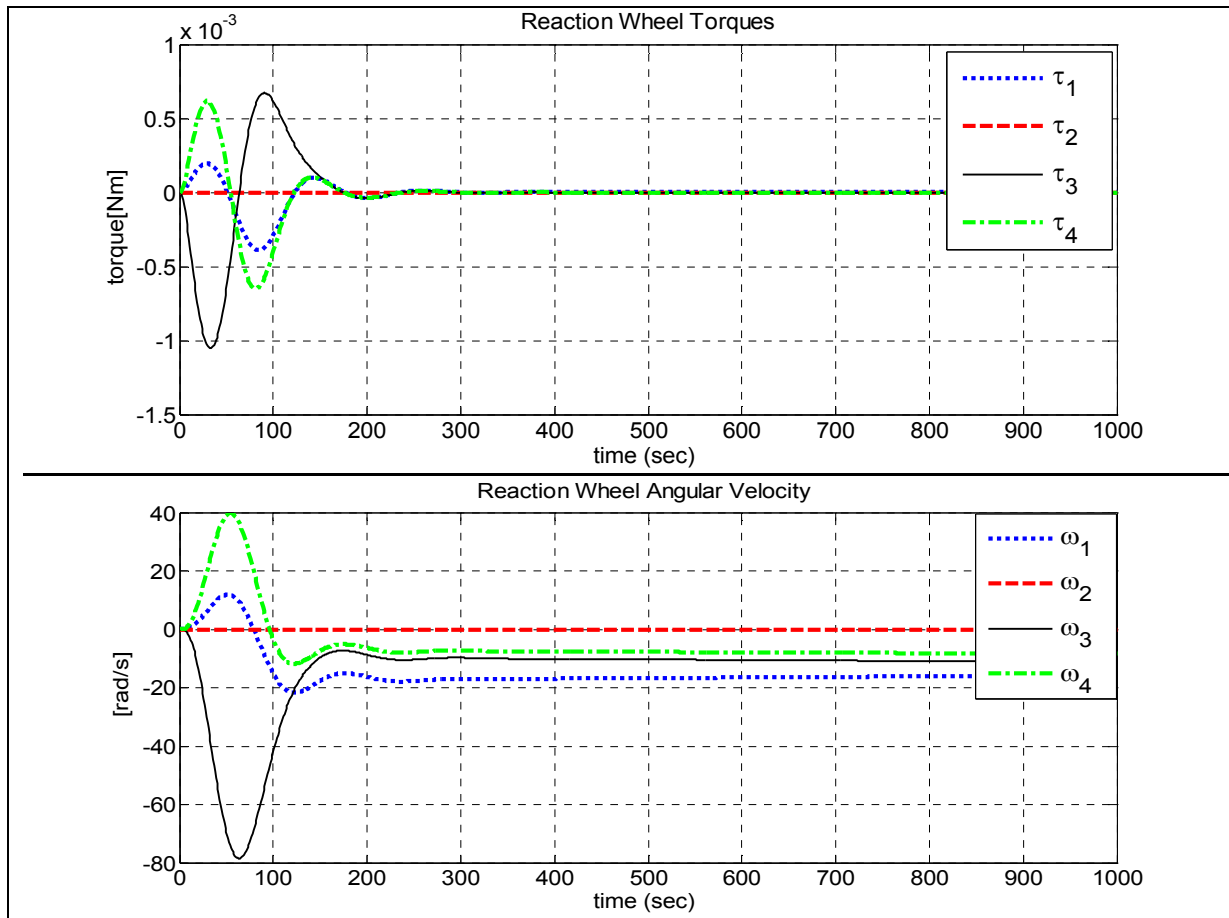**Figure 5.4** – Reaction wheel torques and angular velocities of LQR for pyramid configuration

Reaction wheel torques reaches to zero after 155 seconds. Maximum reaction wheel velocity is 76 rad/s. The total power consumption for this configuration and indicated parameters is 0.0041 W.

5.1.1.1 Reaction Wheel-1 Failure
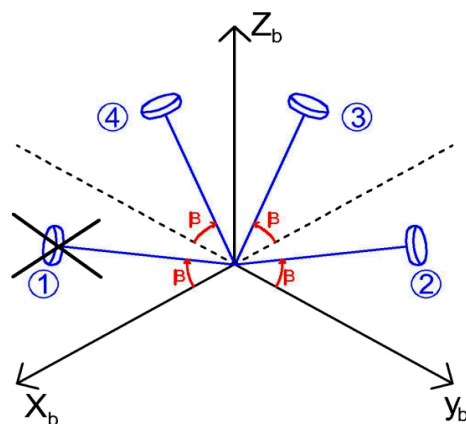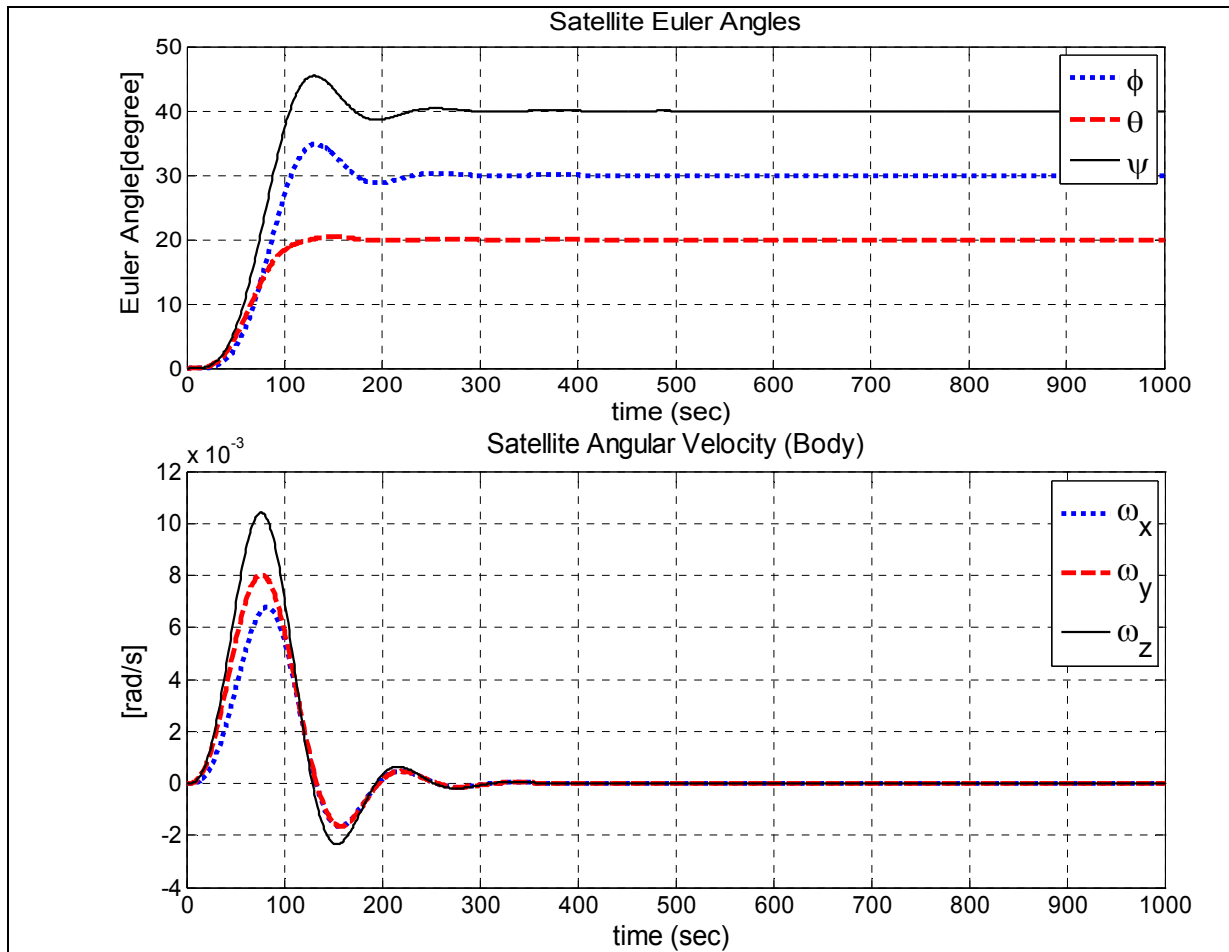
Figure 5.5 – System response of LQR for pyramid configuration when wheel-1 disabled

The system reaches to desired Euler angles in 350 seconds. The settling time for the satellite angular velocity is 365 seconds. It is clear that, the settling times get much higher in the case of loss of one actuator. Moreover, loss of one actuator results in 13.625% overshoot in yaw axis and 16% overshoot in roll axis.
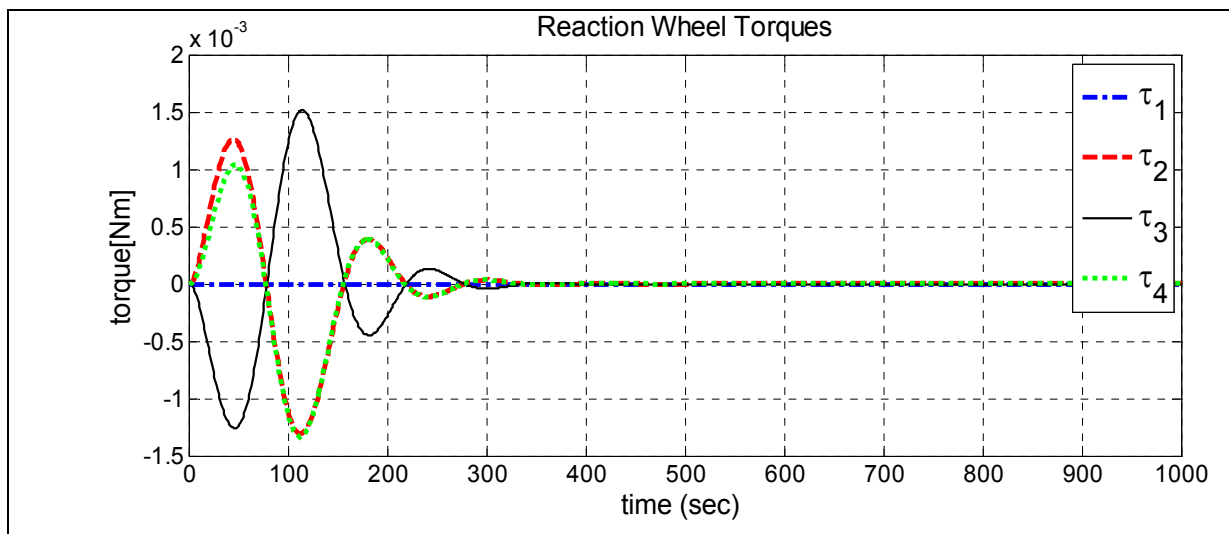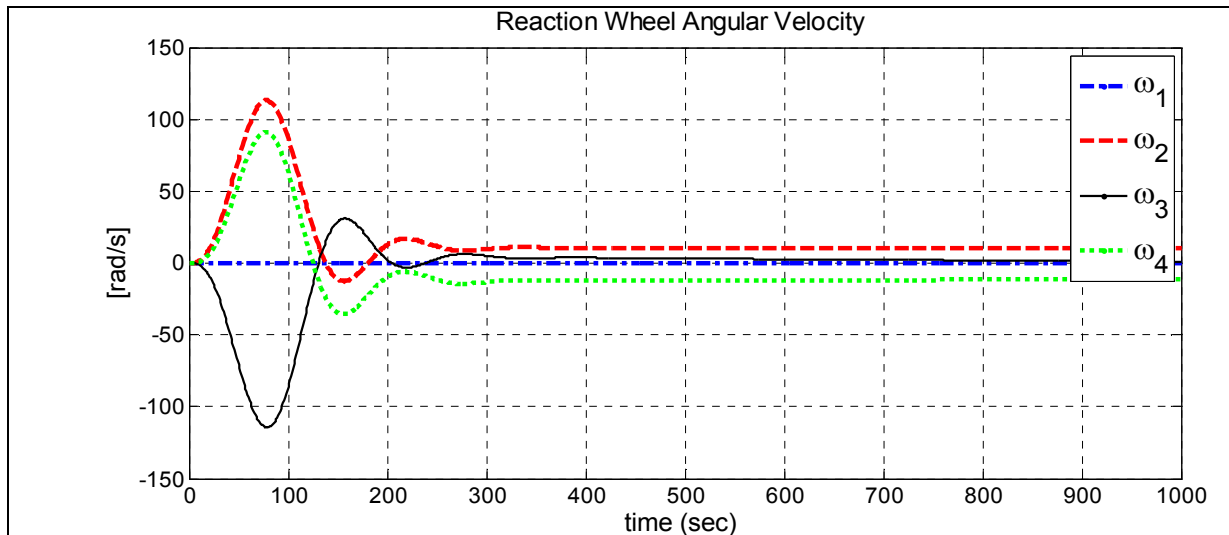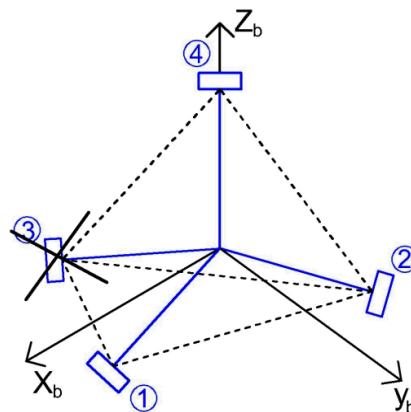
Figure 5.6 – Reaction wheel torques and angular velocities of LQR for pyramid configuration when wheel-1 disabled

Reaction wheel torques reaches to zero after 340 seconds. Maximum reaction wheel velocity is 114 rad/s, which is higher compared to 4-wheel case. As a result, for the case of loss of an actuator the power consumption also increases, which becomes 0.0185 W.
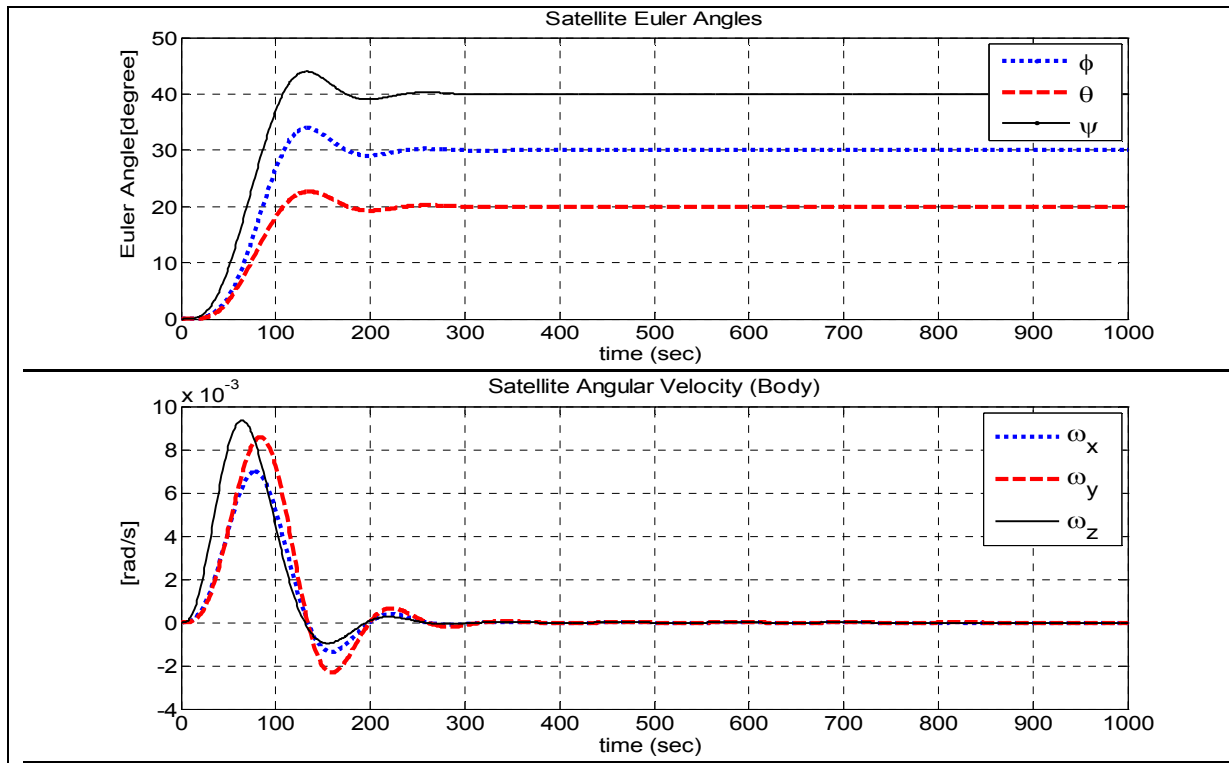
5.1.1.2 Reaction Wheel-2 Failure
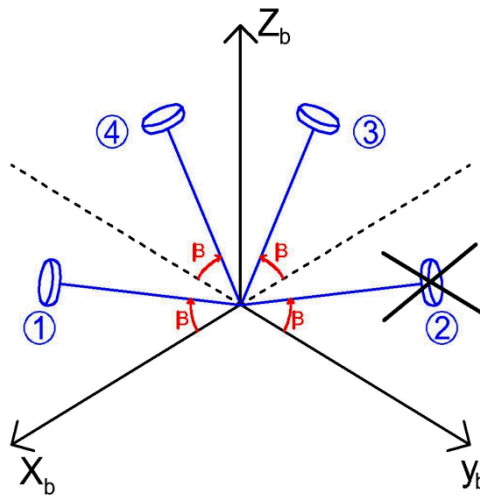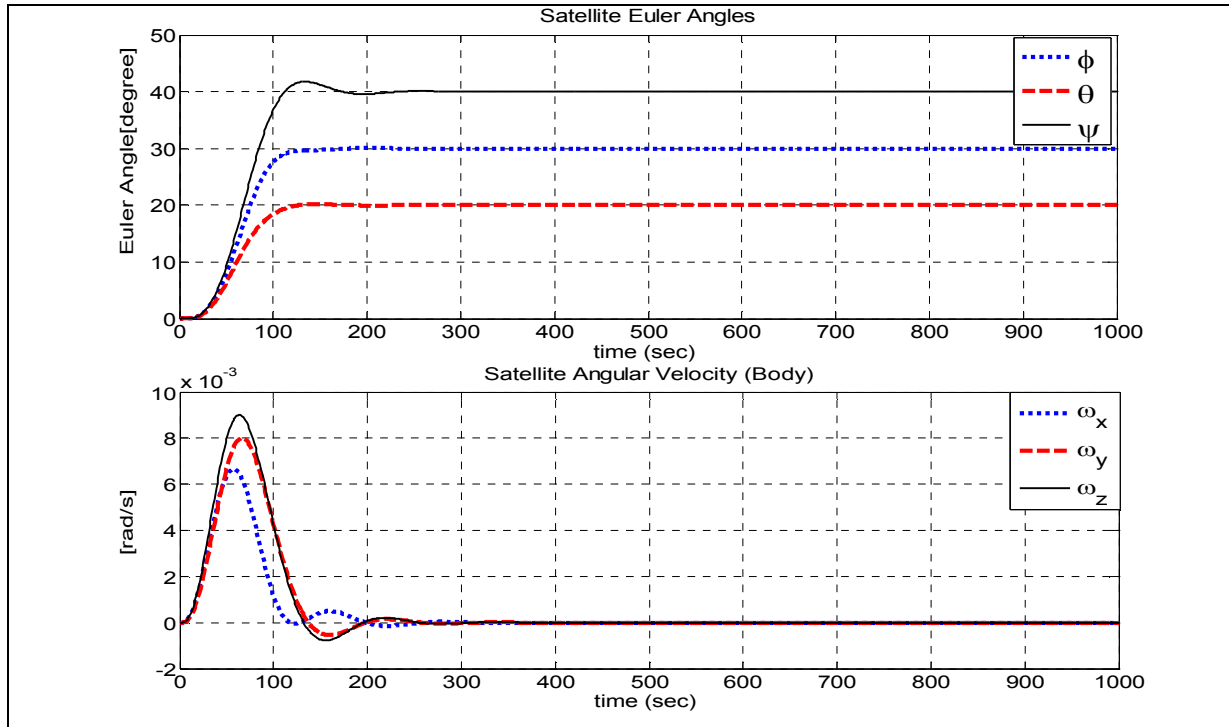
Figure 5.7 – System response of LQR for pyramid configuration when wheel-2 disabled

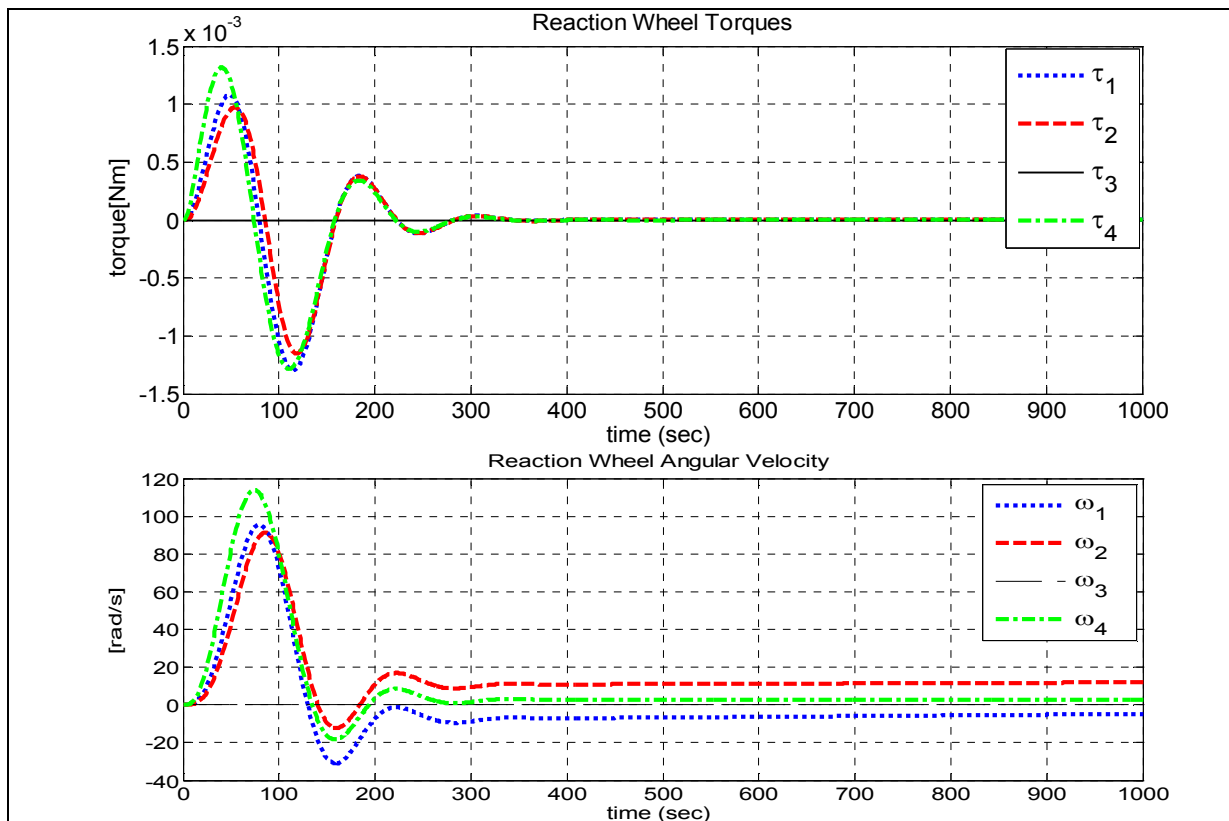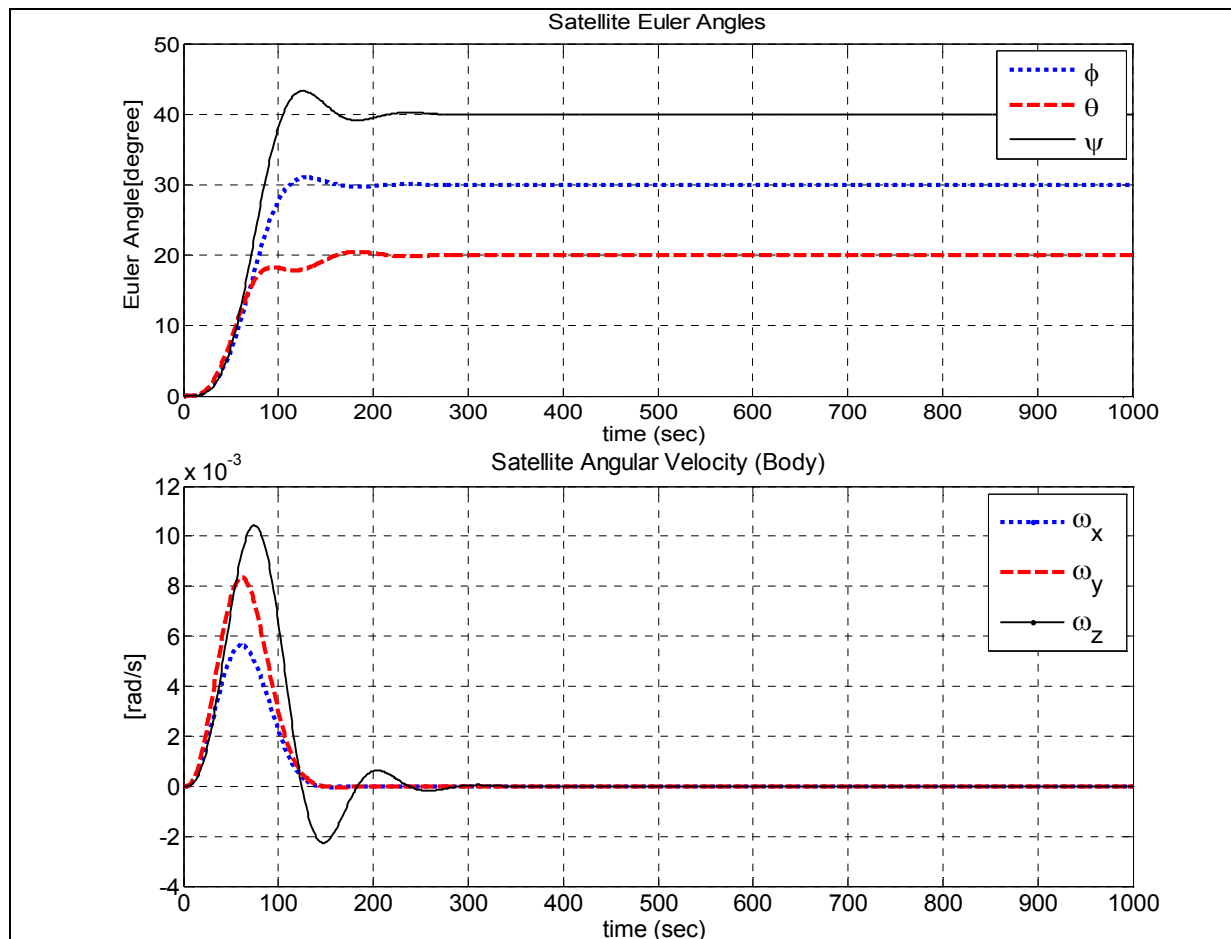The system reaches to desired Euler angles in 340 seconds. The settling time for the satellite angular velocity is 355 seconds. It can be observed that the settling times are lower compared to the case wheel-1 is disabled.
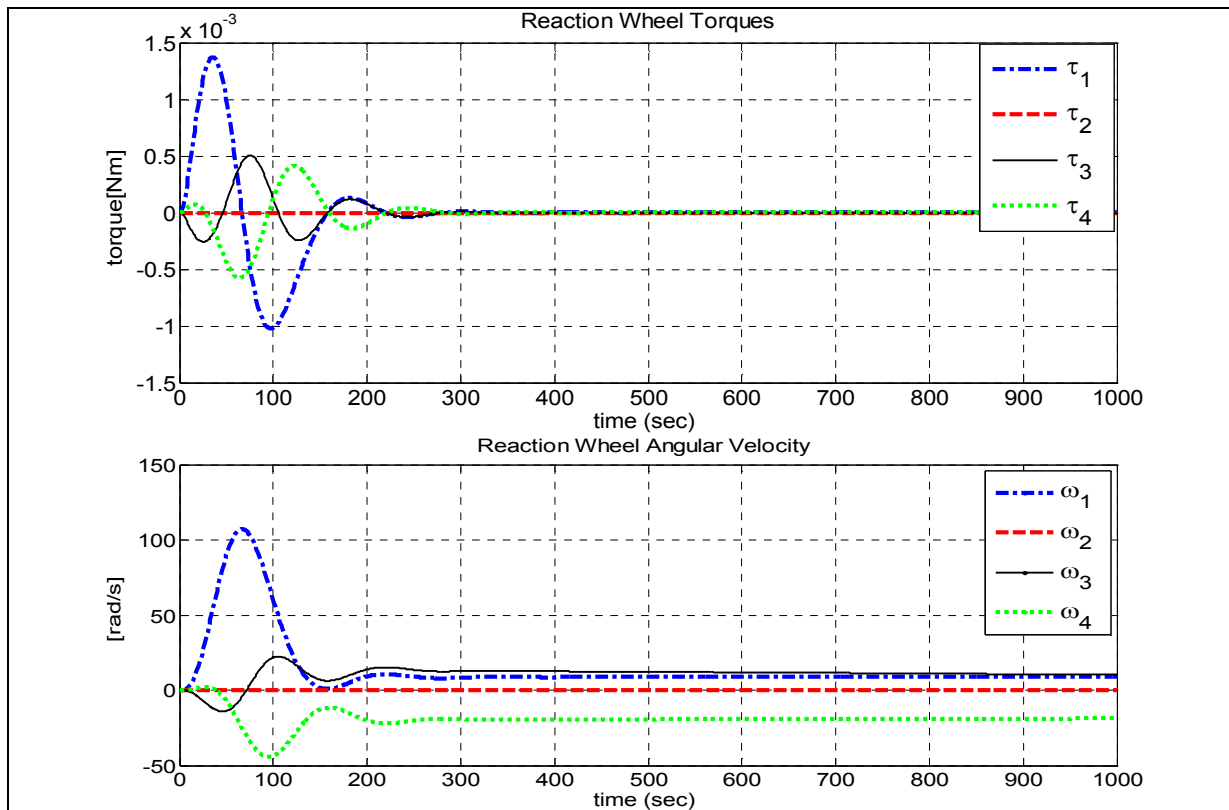
Figure 5.8 – Reaction wheel torques and angular velocities of LQR for pyramid configuration when wheel-2 disabled

Reaction wheel torques reaches to zero after 312 seconds. Maximum reaction wheel velocity is 107 rad/s. It can be seen that, in the case of wheel-2 failure, reaction wheel-1 produces most of the torque compared to wheel-3 and wheel-4. In the case of wheel-1 failure, however, all remaining three wheels were active in producing torques. As a result, the power consumption is lower compared to wheel-1 failure, which is 0.0073 W.
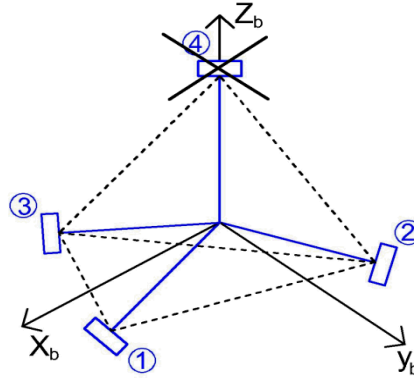
5.1.1.3 Reaction Wheel-3 Failure
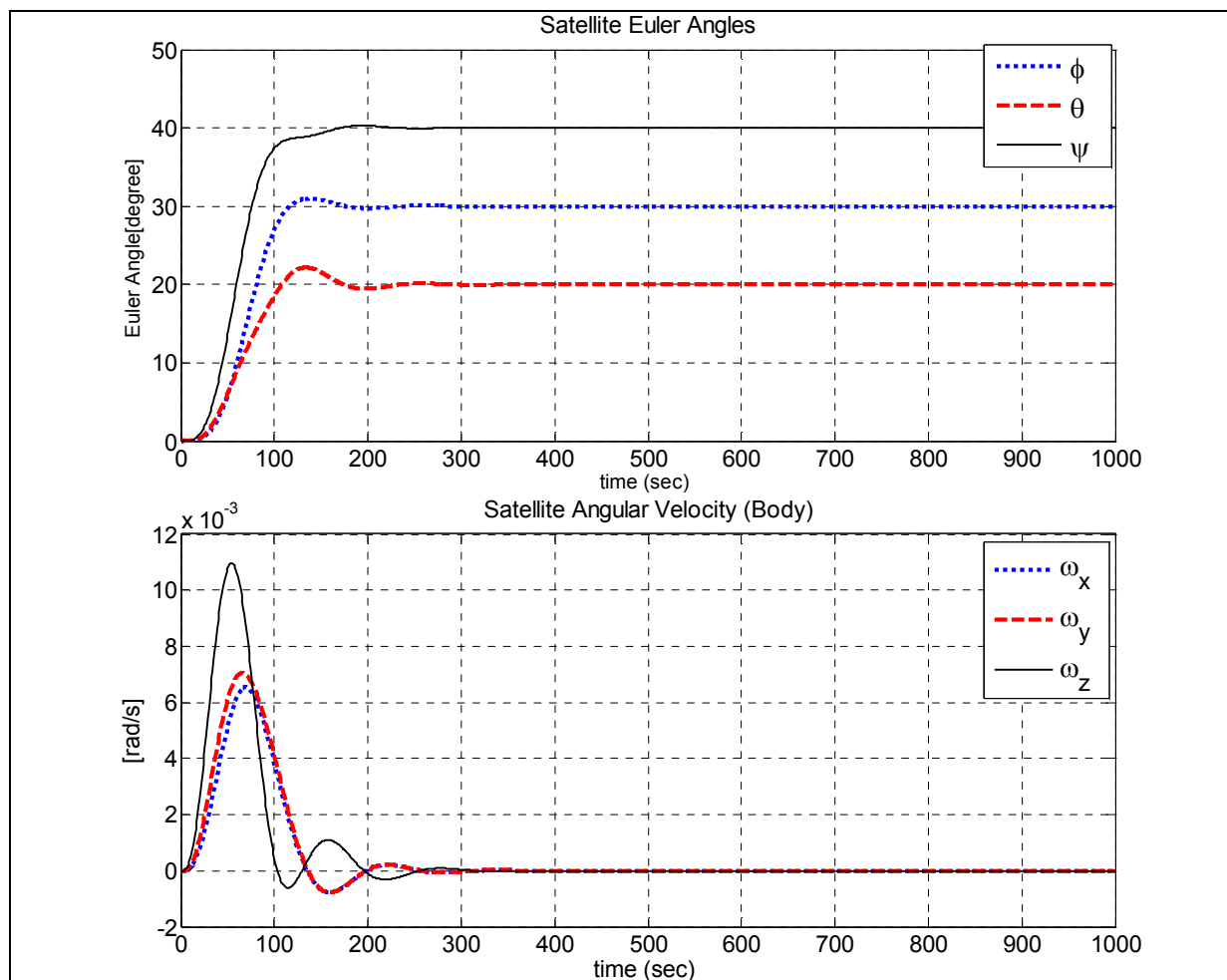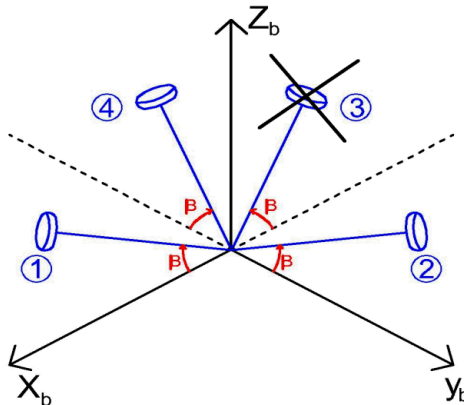
Figure 5.9 – System response of LQR for pyramid configuration when wheel-3 disabled

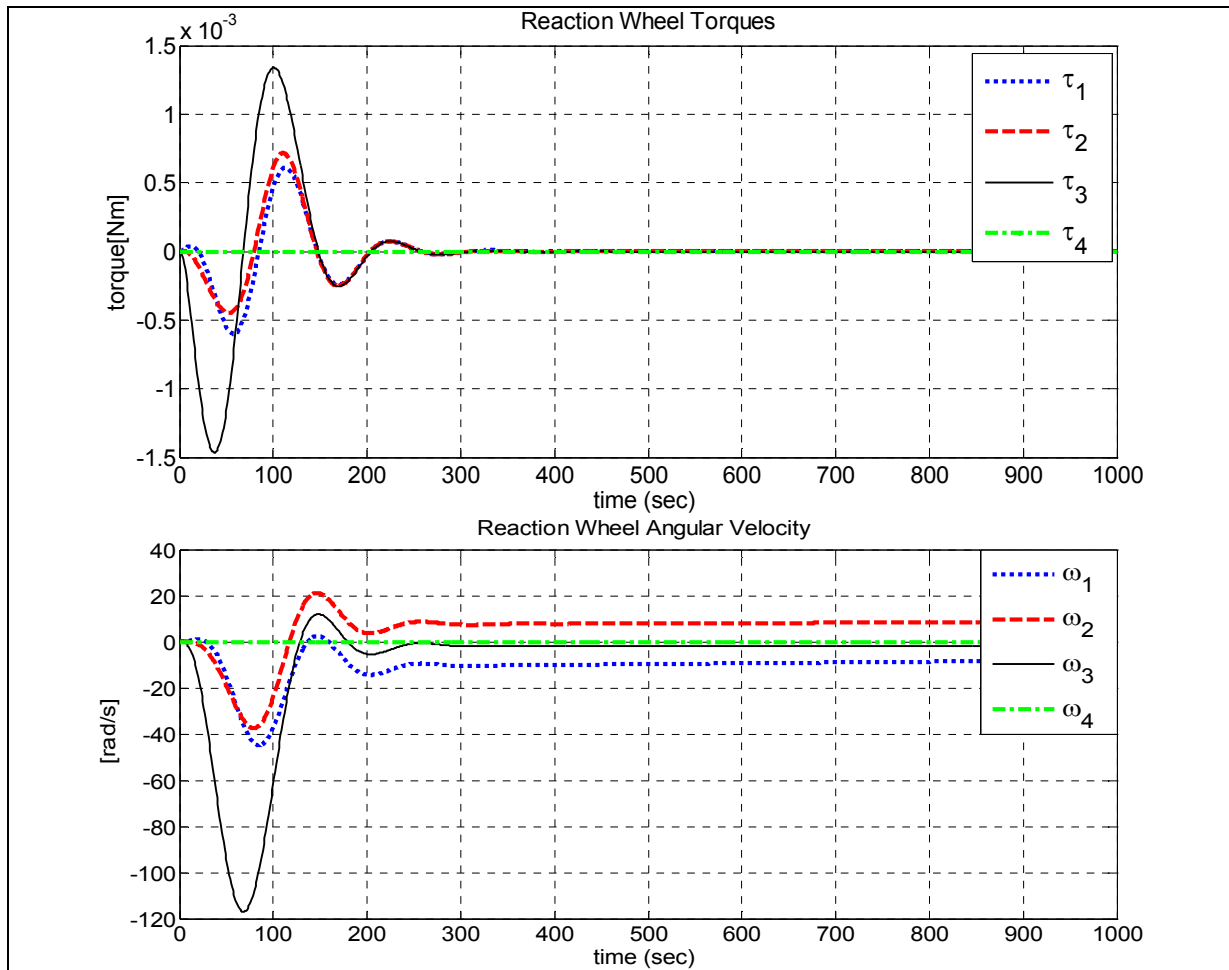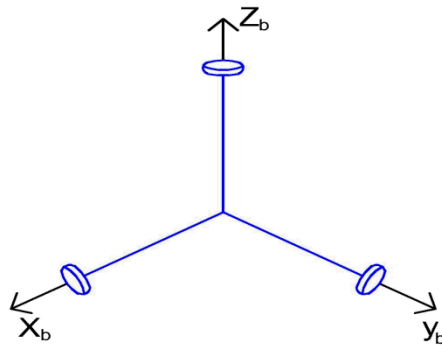The system reaches to desired Euler angles in 348 seconds. The settling time for the satellite angular velocity is 361 seconds. While the settling times are similar to wheel-1 failure case, the oscillations are less than wheel-1 failure case.
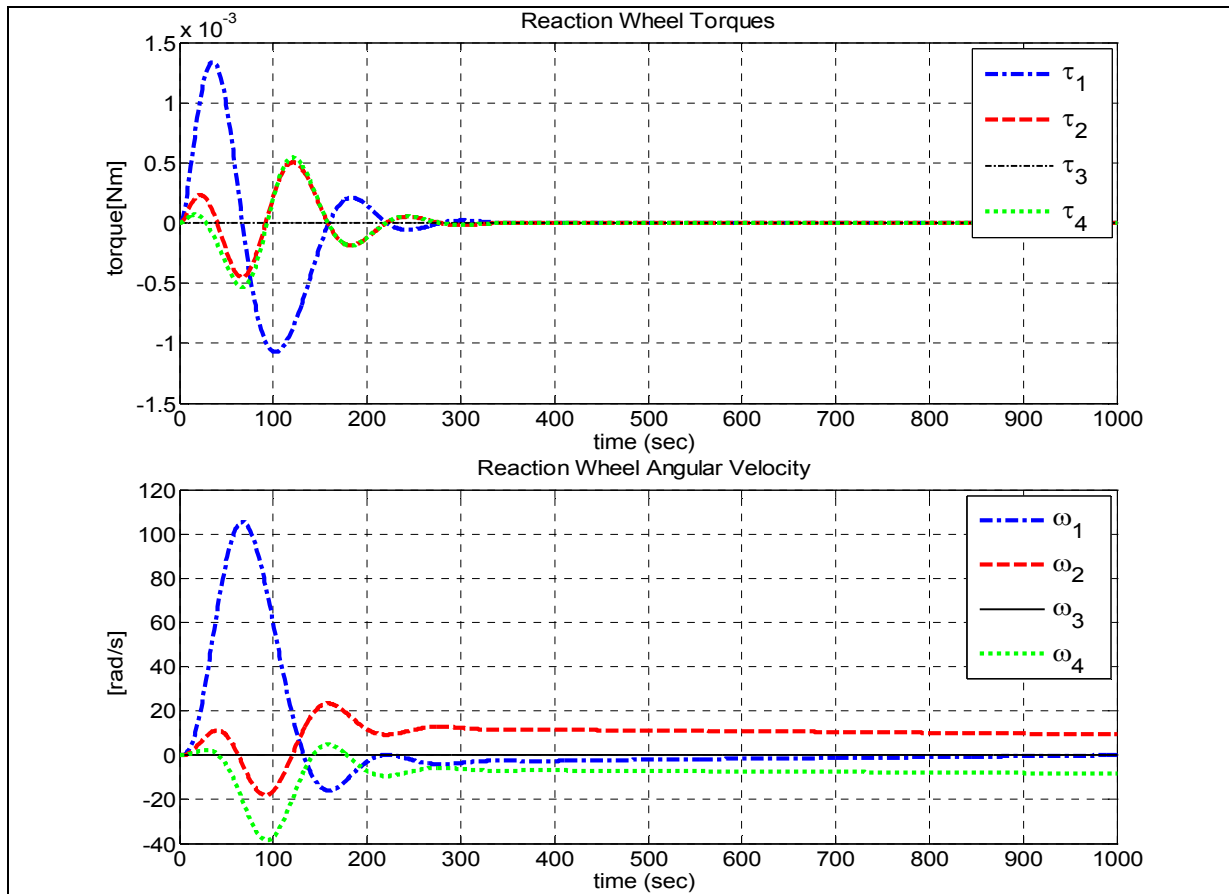
Figure 5.10 – Reaction wheel torques and angular velocities of LQR for pyramid configuration when wheel-3 disabled

Reaction wheel torques reaches to zero after 325 seconds. Maximum reaction wheel velocity is 105 rad/s. The power consumption is 0.0070 W.

5.1.1.4 Reaction Wheel-4 Failure
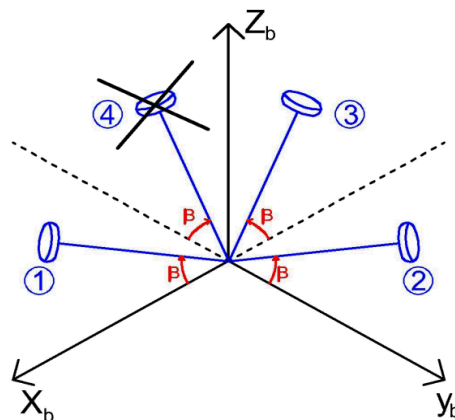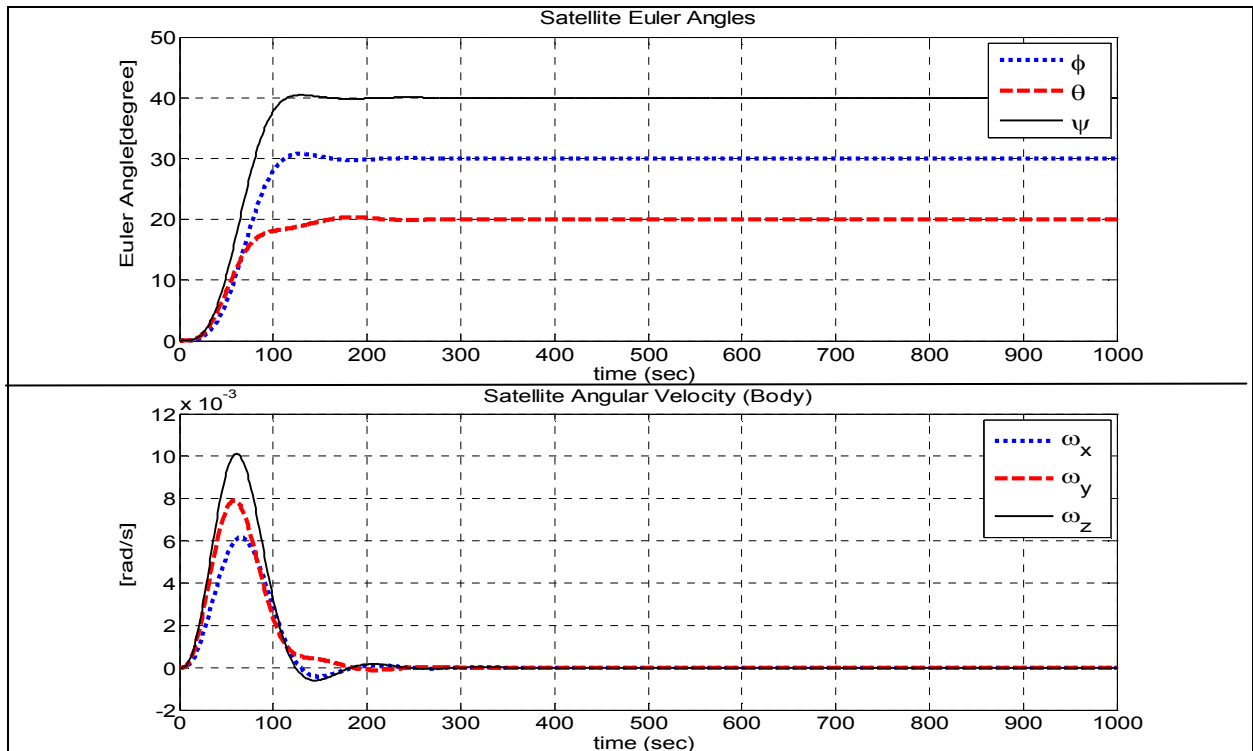
Figure 5.11 – System response of LQR for pyramid configuration when wheel-4 disabled

The system reaches to desired Euler angles in 327seconds. The settling time for the satellite angular velocity is 300 seconds.
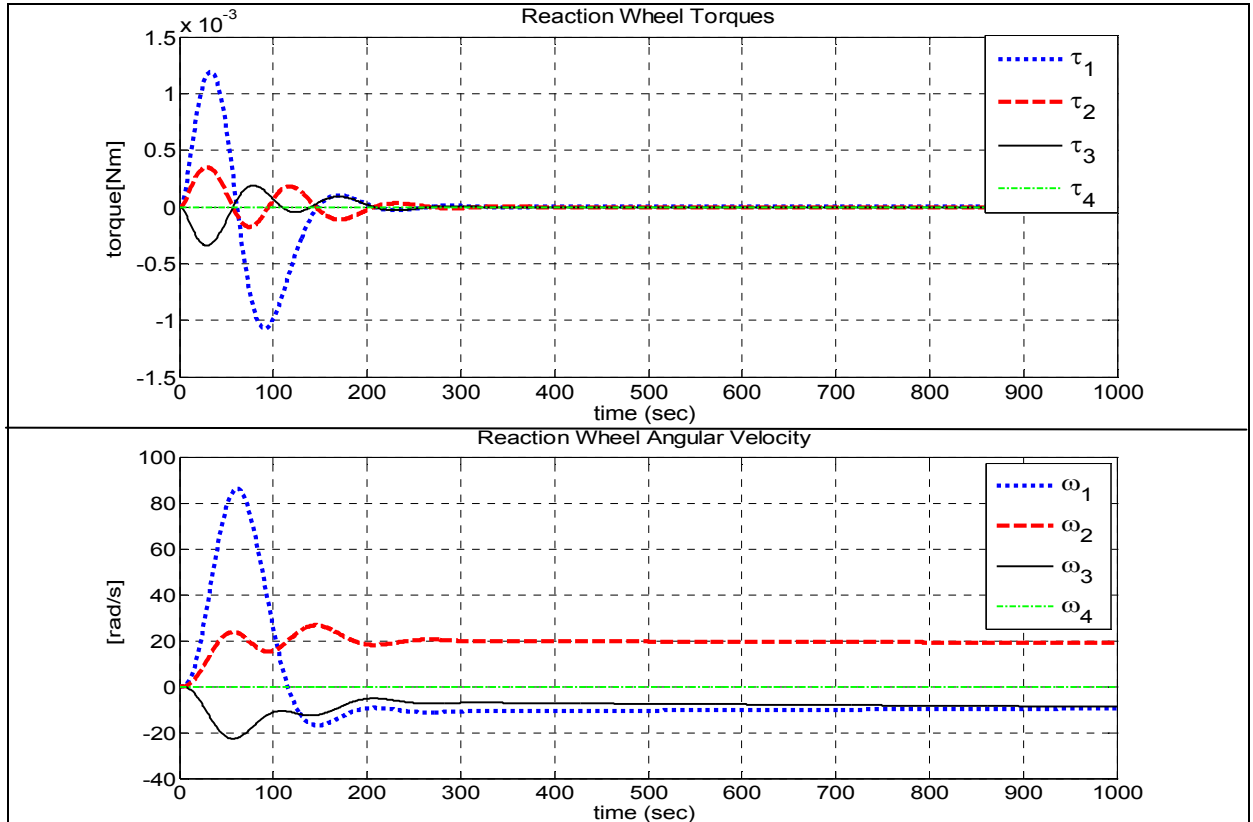
Figure 5.12 – Reaction wheel torques and angular velocities of LQR for pyramid configuration when wheel-4 disabled

45

Reaction wheel torques reaches to zero after 258 seconds. Maximum reaction wheel velocity is 86 rad/s. The total power consumption is 0.0046 W, which is lower compared to other wheel failure cases.

5.1.2 Tetrahedron Configuration
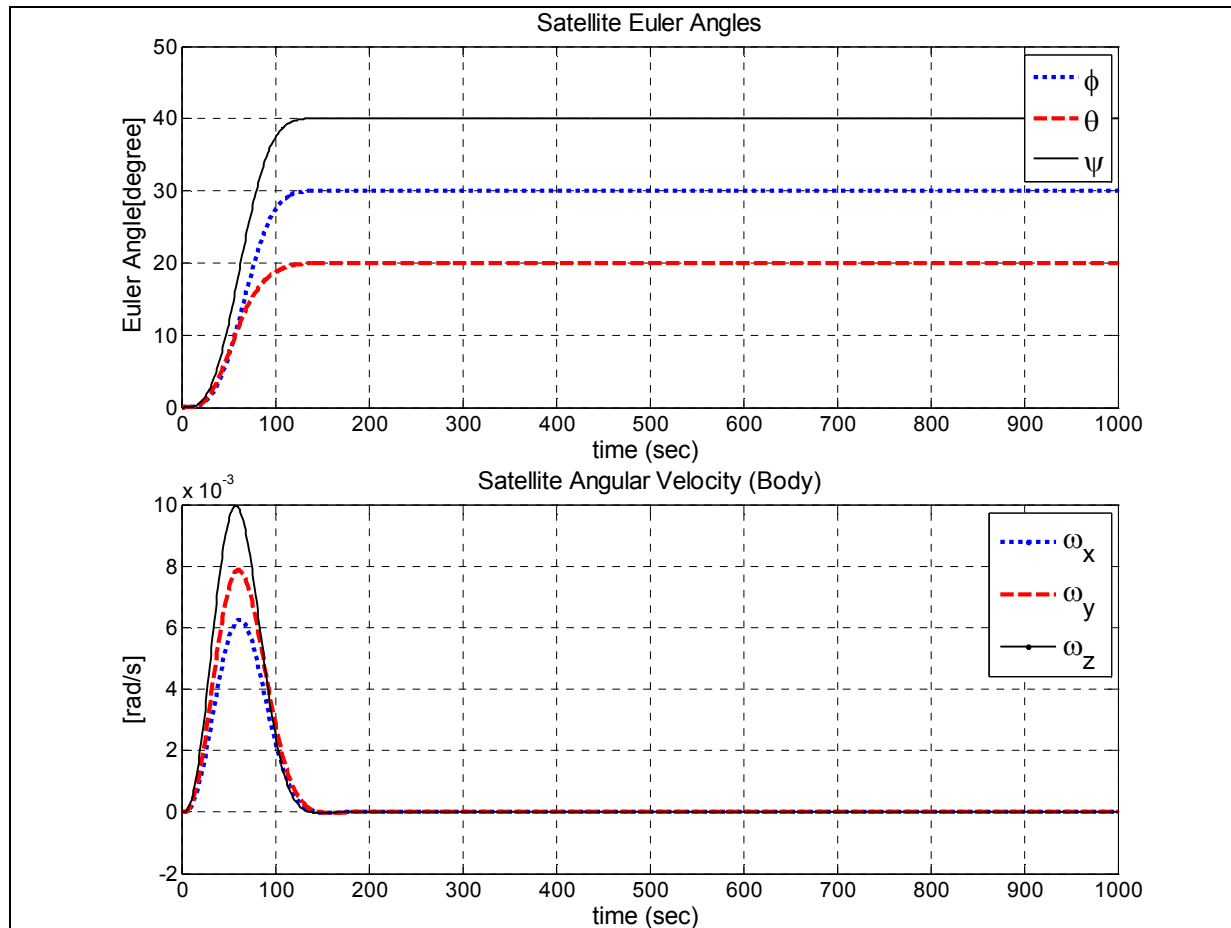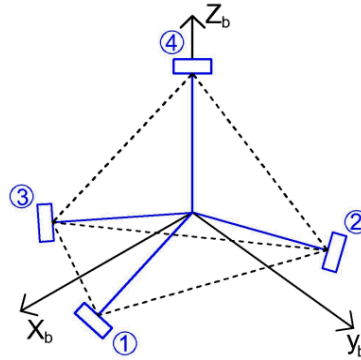
Figure 5.13 – System response of LQR for tetrahedron configuration

The system reaches to desired Euler angles in 162 seconds. The settling time for the satellite angular velocity is 174 seconds. The settling times compared to pyramid configuration is almost the same.
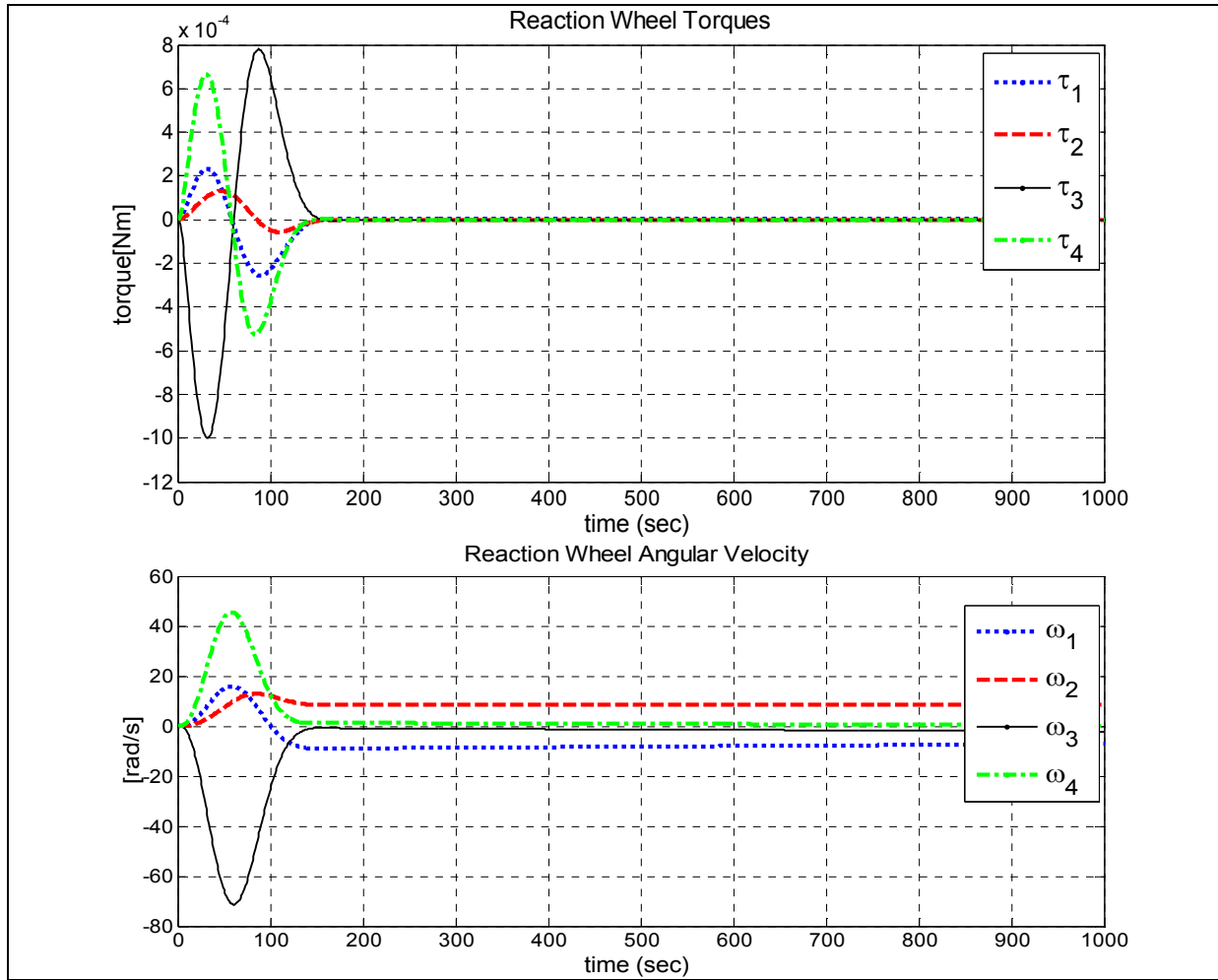
Figure 5.14 – Reaction wheel torques and angular velocities of LQR for tetrahedron configuration

Reaction wheel torques reaches to zero after 155 seconds. Maximum reaction wheel velocity is 71 rad/s. The power consumption for this configuration and indicated parameters is 0.0038 W, which is lower compared to pyramid configuration.

5.1.2.1 Reaction Wheel-1 Failure
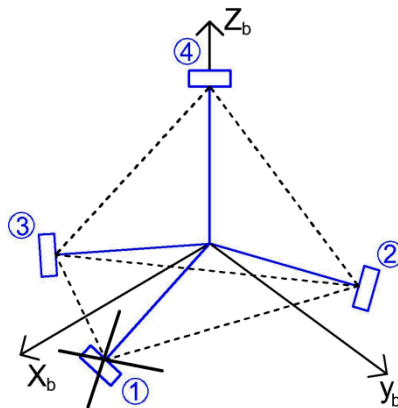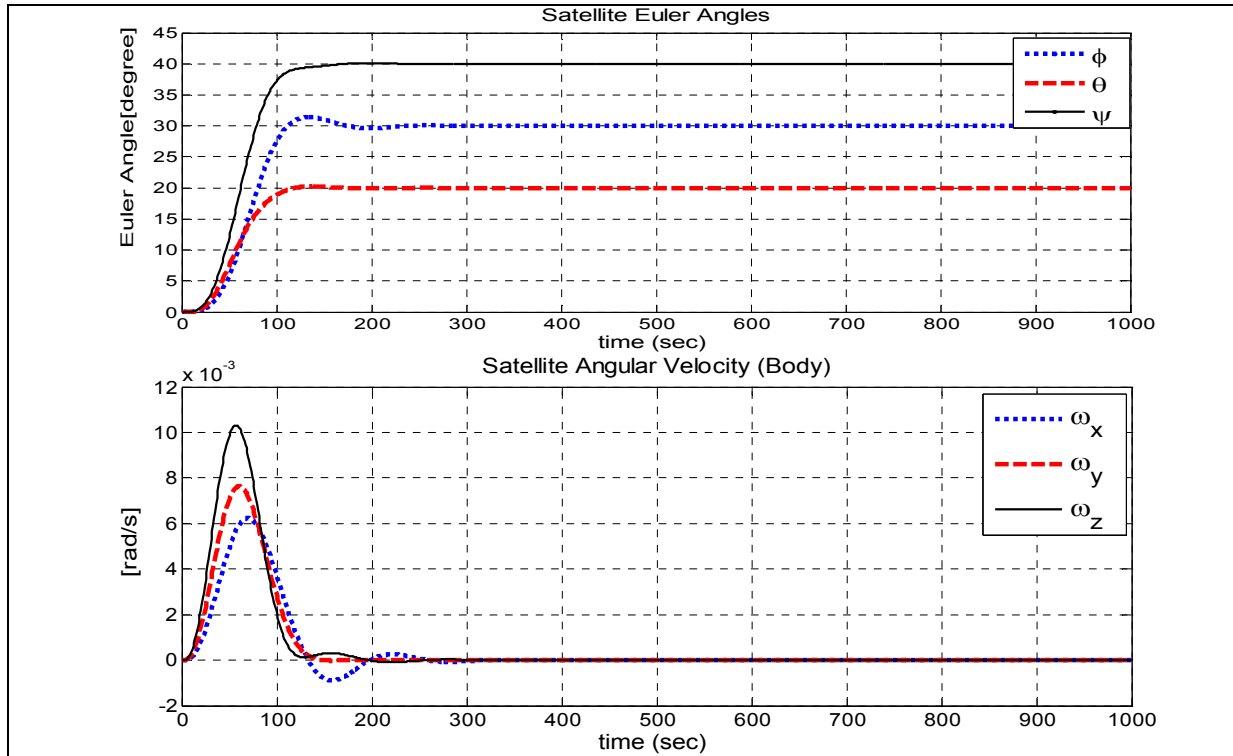
Figure 5.15 – System response of LQR for tetrahedron configuration when wheel-1 disabled

The system reaches to desired Euler angles in 352 seconds. The settling time for the satellite angular velocity is 365 seconds. It is clear that, the settling times get higher in the case of loss of one actuator. Moreover, loss of wheel-1 results in 4.66% overshoot in roll axis.
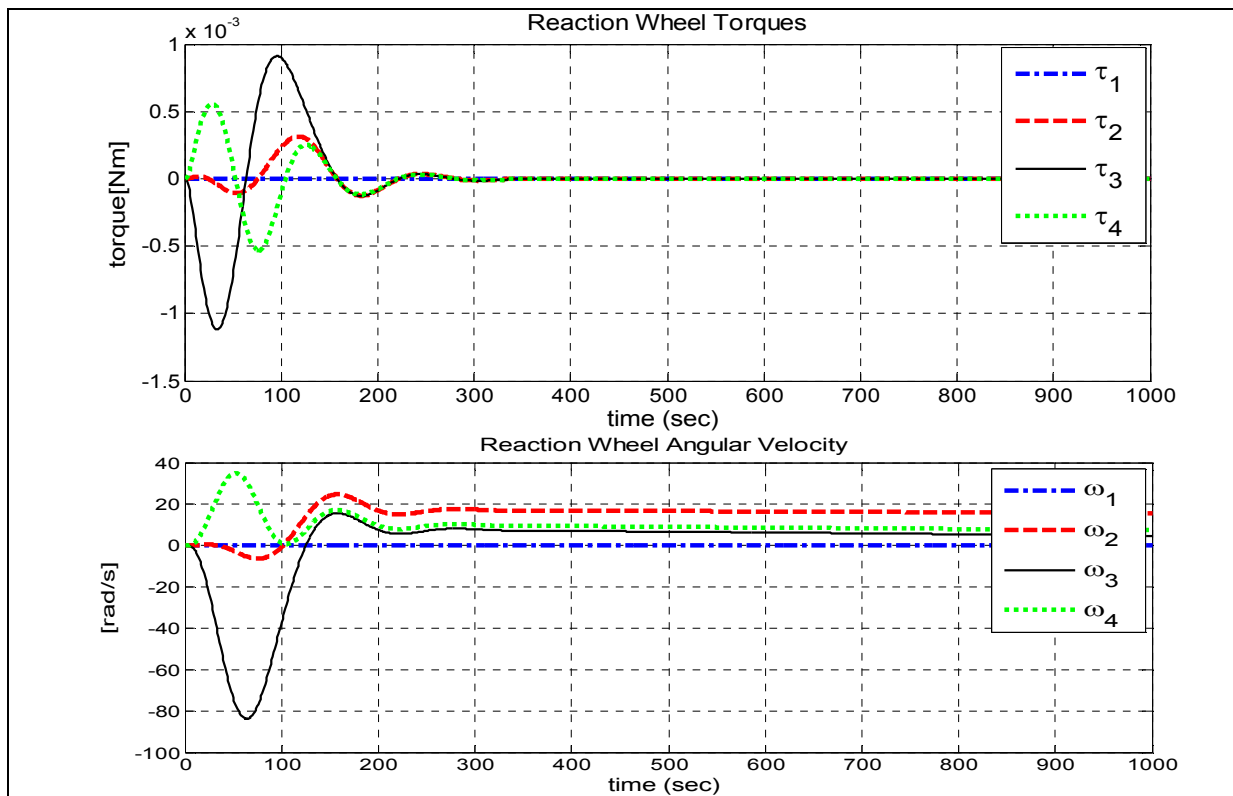
Figure 5.16 – Reaction wheel torques and angular velocities of LQR for tetrahedron configuration when wheel-1 disabled

48

Reaction wheel torques reaches to zero after 330 seconds. Maximum reaction wheel velocity is 84 rad/s, which is lower compared to pyramid configuration wheel-1 failure case. Therefore total power consumption is much lower compared to pyramid configuration wheel-1 failure case, which becomes 0.0047 W.

5.1.2.2 Reaction Wheel-2 Failure
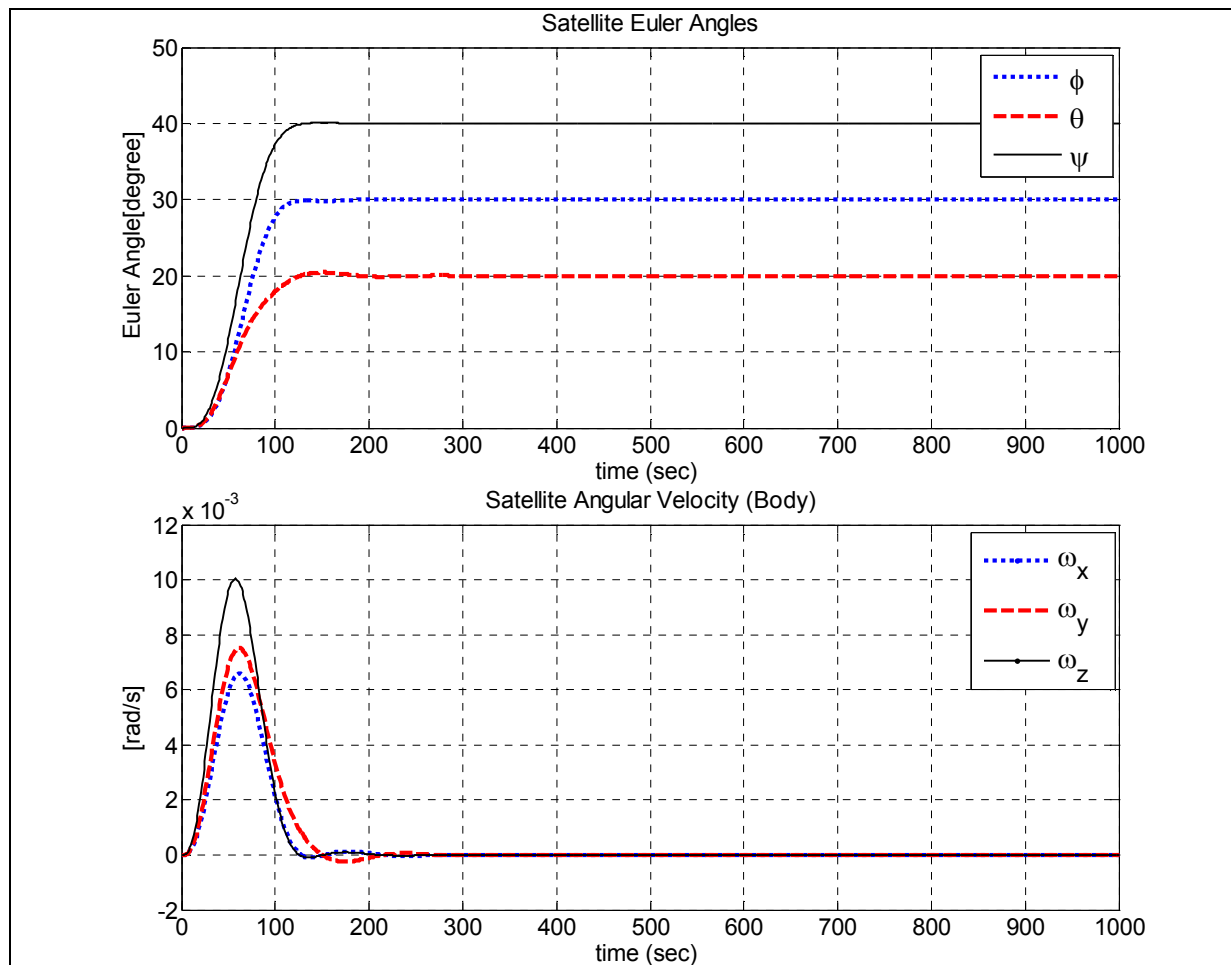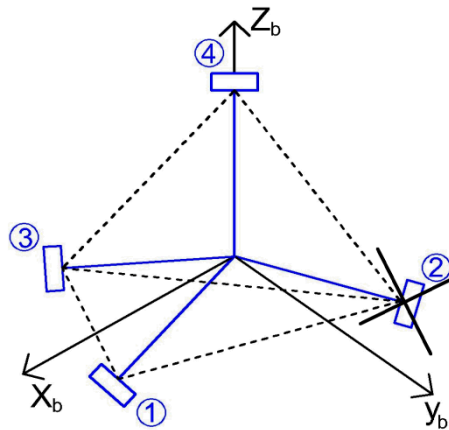
Figure 5.17 – System response of LQR for tetrahedron configuration when wheel-2 disabled

The system reaches to desired Euler angles in 300 seconds. The settling time for the satellite angular velocity is 320 seconds. It can be seen that, settling times are lower compared to wheel-1 failure case.

Figure 5.18 – Reaction wheel torques and angular velocities of LQR for tetrahedron configuration when wheel-2 disabled

Reaction wheel torques reaches to zero after 275 seconds. Maximum reaction wheel velocity is 78 rad/s. The total power consumption is 0.0043 W.

5.1.2.3 Reaction Wheel-3 Failure

Figure 5.19 – System response of LQR for tetrahedron configuration when wheel-3 disabled

The system reaches to desired Euler angles in 354 seconds. The settling time for the satellite angular velocity is 374 seconds.

Figure 5.20 – Reaction wheel torques and angular velocities of LQR for tetrahedron configuration when wheel-3 disabled

Reaction wheel torques reaches to zero after 345 seconds. Maximum reaction wheel velocity is 113 rad/s. The total power consumption is 0.0162 W, which is much higher compared to other wheel failure cases.
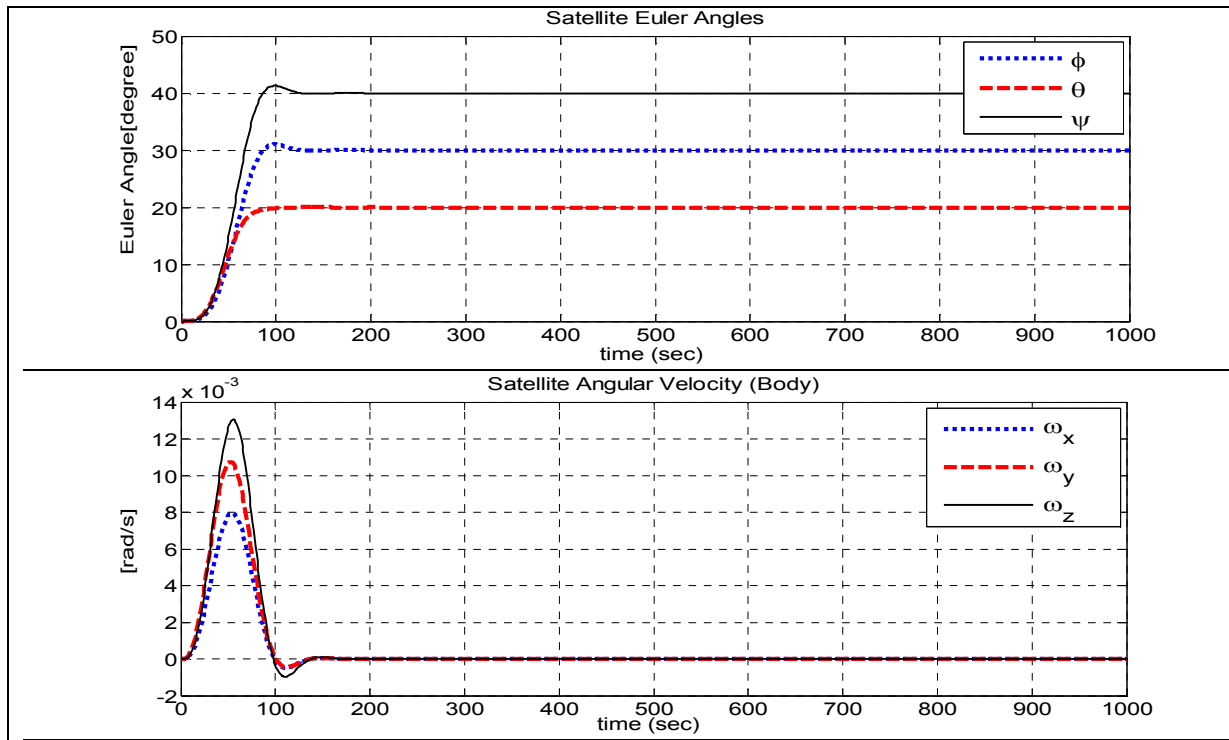
5.1.2.4 Reaction Wheel-4 Failure

Figure 5.21 – System response of LQR for tetrahedron configuration when wheel-4 disabled

The system reaches to desired Euler angles in 318 seconds. The settling time for the satellite angular velocity is 340 seconds.
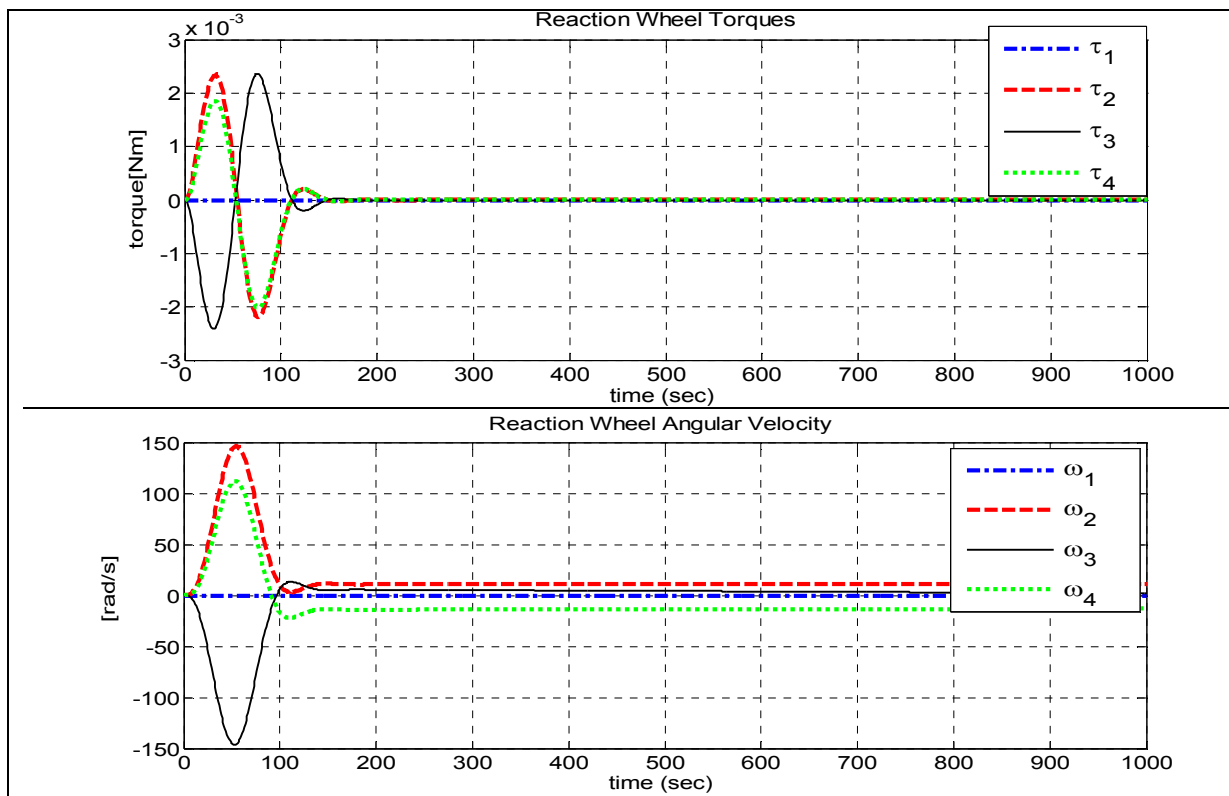
Figure 5.22 – Reaction wheel torques and angular velocities of LQR for tetrahedron configuration when wheel-4 disabled

Reaction wheel torques reaches to zero after 300 seconds. Maximum reaction wheel velocity is 116 rad/s. The total power consumption is 0.0090 W.

5.1.3 Standard 3-wheel Configuration
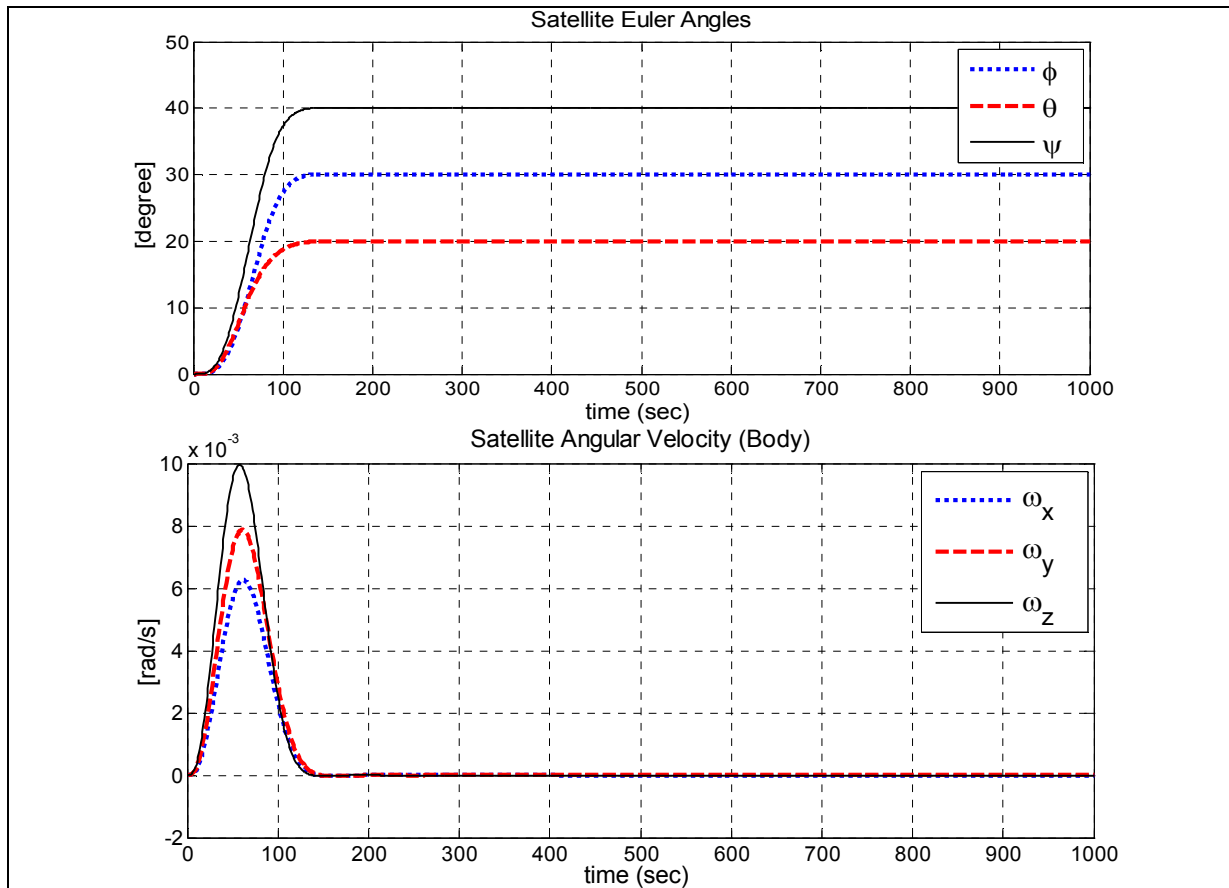
Figure 5.23 – System response of LQR for standard 3-wheel configuration

The system reaches to desired Euler angles in 164 seconds. The settling time for the satellite angular velocity is also 174 seconds. The settling times are almost the same compared to pyramid and tetrahedron configurations.
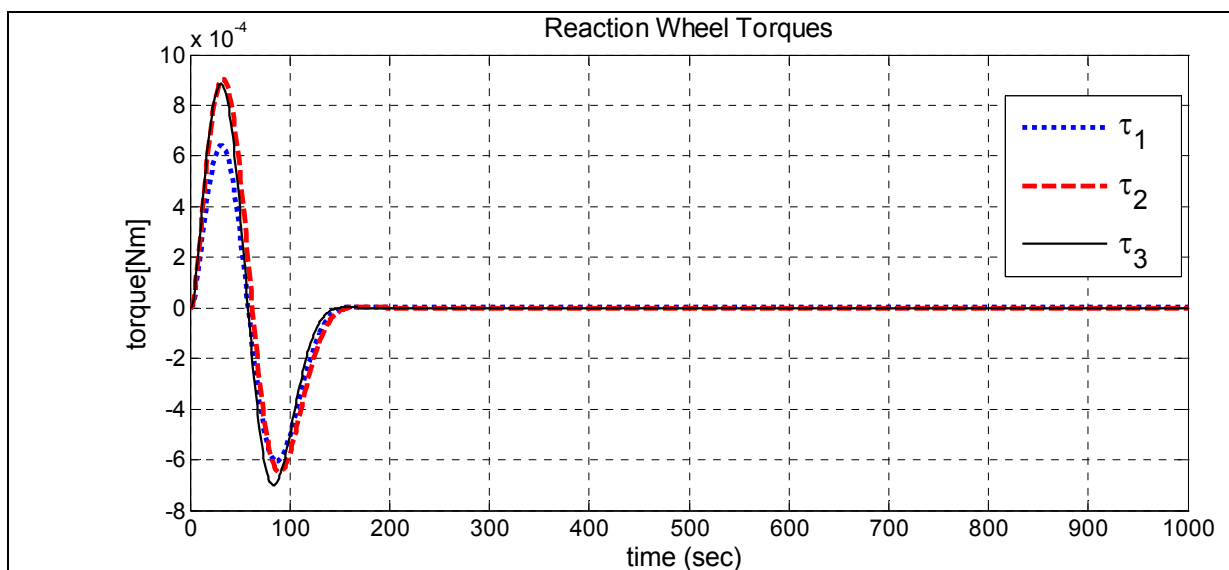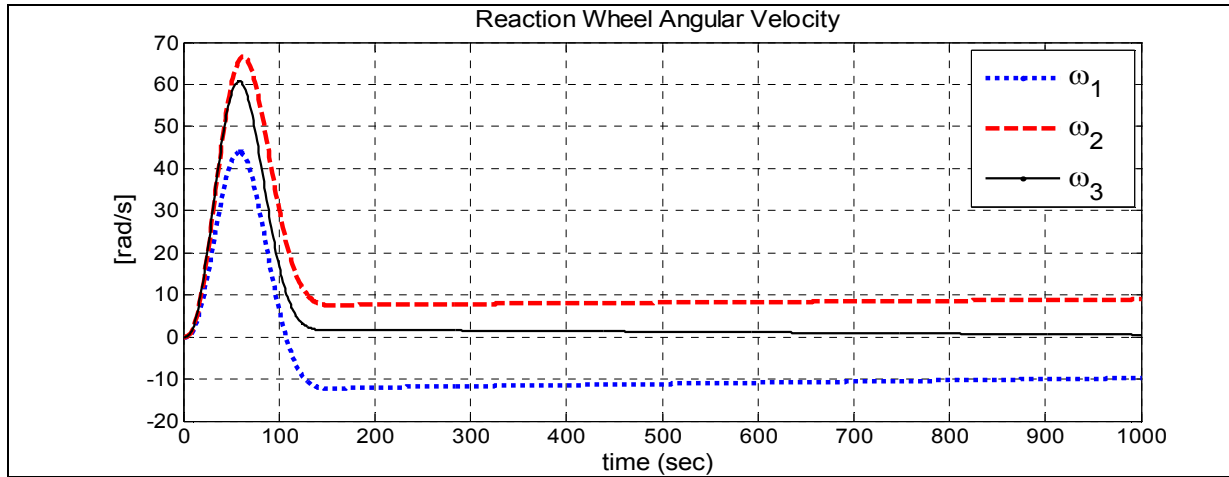
**Figure 5.24** – Reaction wheel torques and angular velocities of LQR for 3-wheel configuration

Maximum reaction wheel velocity is 66 rad/s. The power consumption 0.0051 W, which is higher compared to pyramid and tetrahedron configurations without wheel failure.

It can be concluded that, for a given cross-over frequency and weighting matrices, the system tends to keep the settling times at the same values while the power consumption changes with different reaction wheel configurations. In the case of wheel failures, however, settling times and power consumptions increase. Tetrahedron configuration resulted in the lowest power consumption while 3-wheel configuration resulted in highest power consumption.

The following table illustrates the effect of weighting matrix Q over the system performances:

Parameter	Q = 0.1*eye(6)	Q = eye(6)
Euler angle settling time	230 s	160 s
Body rate settling time	247 s	170 s
Power consumption	0.0024 W	0.0041 W

Table 5.3 – System performance comperison for different Q matrices (pyramid config.)

It is clear that as the settling time gets shorter, power consumption gets higher.
(*eye(n)*) is n-by-n identity matrix function in MATLAB)

5.2 Sliding Mode Controller Simulation Results

Control input for linear quadratic regulator controller is defined in Chapter 4 as:

$$u = \omega_{bo} \times (I\omega_{bo} + h_w) - T_d - I\dot{\omega}_{bo} - IK\dot{q}_e - IGsgn(S) \tag{5.5}$$

Controller parameters used in the simulation are given in Table 5.3 as follows:

Parameter	Value
Initial Angular Velocity	$\omega_{bo}^{b} = [0\ 0\ 0]^{T}$
Initial Euler Angles	$[\varnothing\ \theta\ \Psi] = [0\ 0\ 0]^{T}$
Control Weighting Matrices	K = 0.3*eye(3);
	G = 0.1*eye(3);
Desired Euler Angles	$[\varnothing\ \theta\ \Psi] = [30\ 20\ 40]^{T}$
Cross-over frequency	$\omega_{n} = 0.02$
Relative damping factor	$\zeta = 1$
Maximum Wheel Torque	5 mNm

Table 5.3 - Simulation parameters of Sliding Mode Control

Implementation of the controller can be shown in flow chart as follows:

```
┌─────────────────────────────┐
│  Loading the current and     │
│  desired quaternion values   │
└─────────────────────────────┘
              │
              ▼
┌─────────────────────────────┐
│  Loading the current and     │
│  desired quaternion values   │
└─────────────────────────────┘
              │
              ▼
┌─────────────────────────────┐
│  Loading angular velocity    │
│  relative to inertial frame  │
└─────────────────────────────┘
              │
              ▼
┌─────────────────────────────┐
│  Transformation of angular   │
│  velocity relative to orbit  │
│  frame                       │
└─────────────────────────────┘
              │
              ▼
┌─────────────────────────────┐
│  Calculation of error        │
│  quaternion                  │
└─────────────────────────────┘
              │
              ▼
┌─────────────────────────────┐
│  Creating control weight     │
│  matrices                    │
└─────────────────────────────┘
              │
              ▼
┌─────────────────────────────┐
│  Creating sliding manifold   │
└─────────────────────────────┘
              │
              ▼
┌─────────────────────────────┐
│  Calculating angular         │
│  momentum of reaction wheels │
└─────────────────────────────┘
              │
              ▼
┌─────────────────────────────┐
│  Calculating command torque  │
└─────────────────────────────┘
```
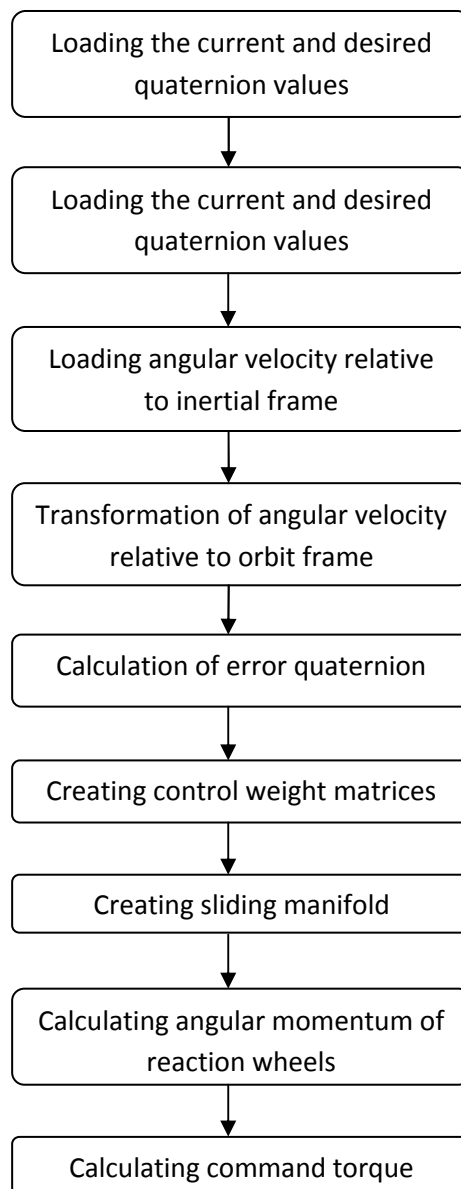
5.2.1 Pyramid Configuration
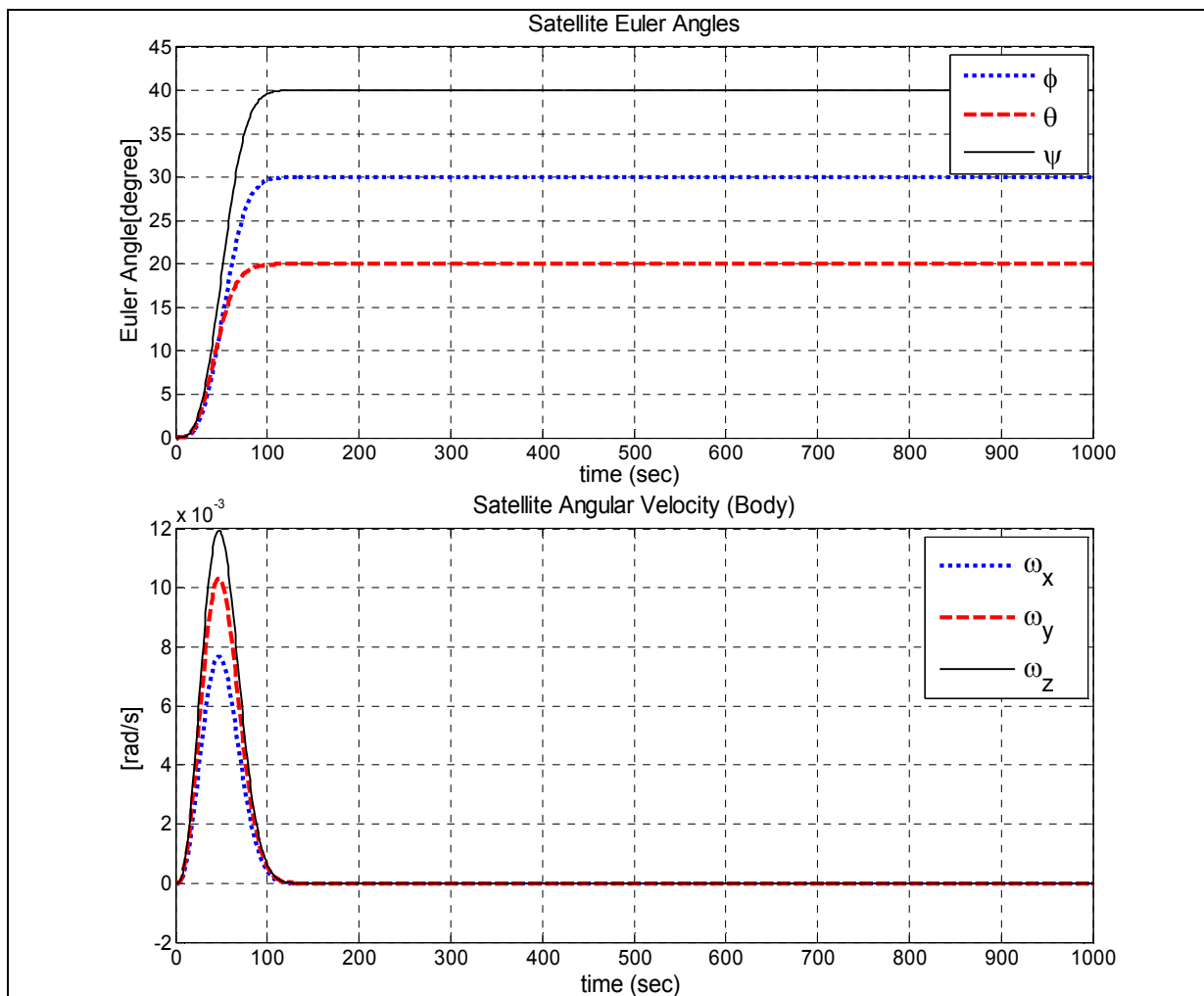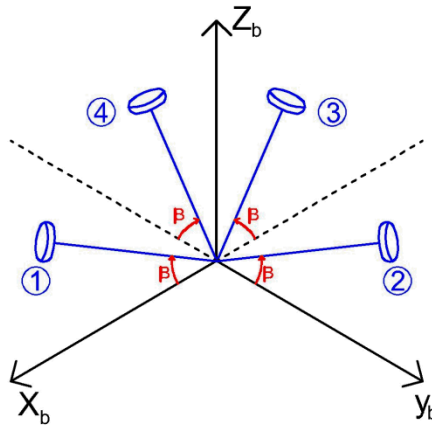
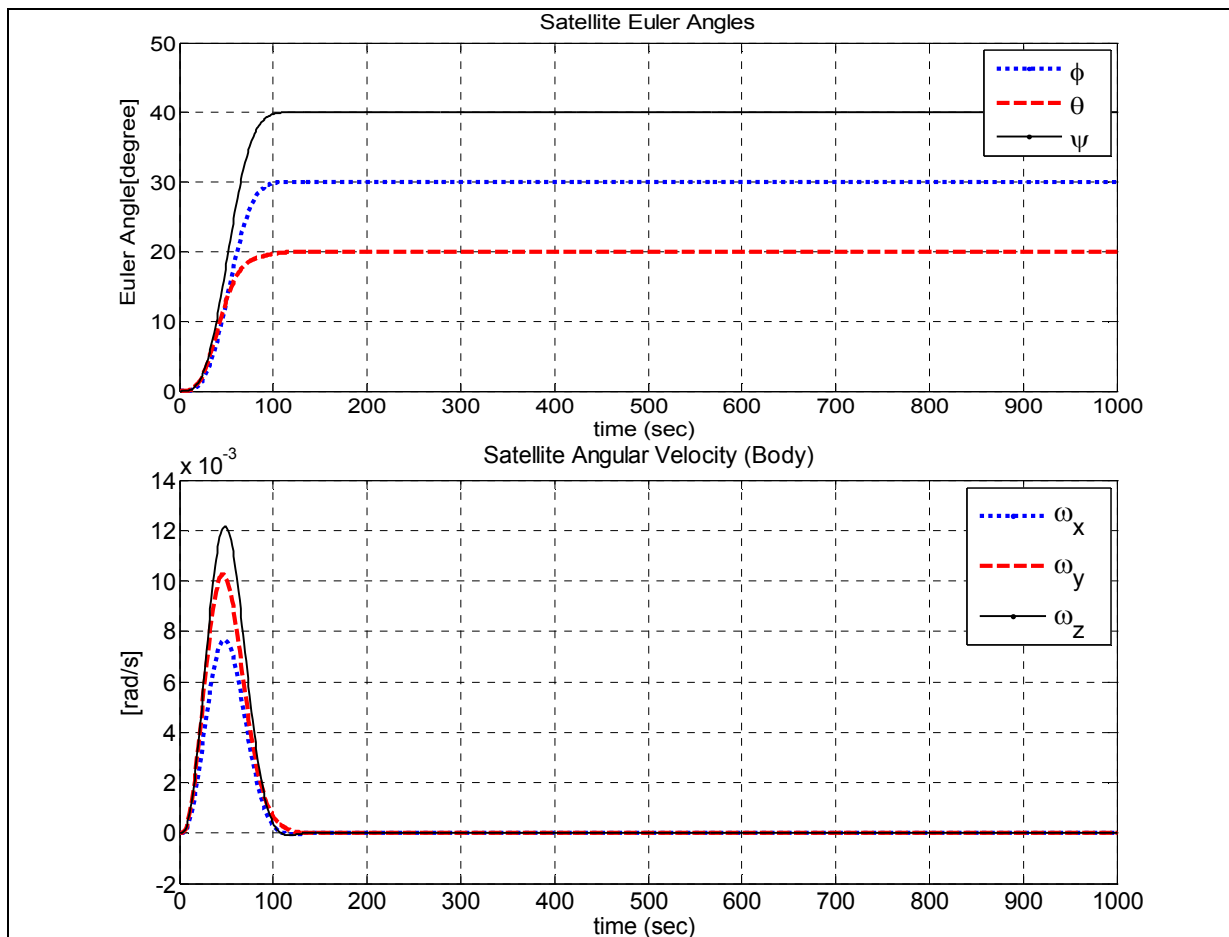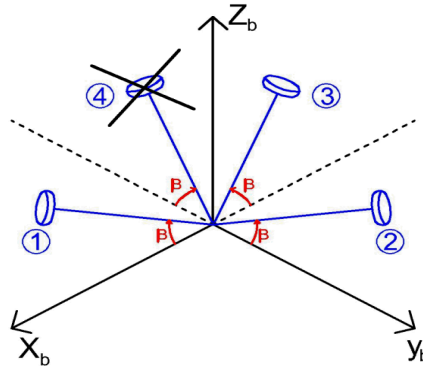**Figure 5.25** – System response of Sliding Mode for pyramid configuration

The system reaches to desired Euler angles in 122 seconds. The settling time for the satellite angular velocity is 128 seconds. These settling times are lower compared to LQR pyramid configuration.
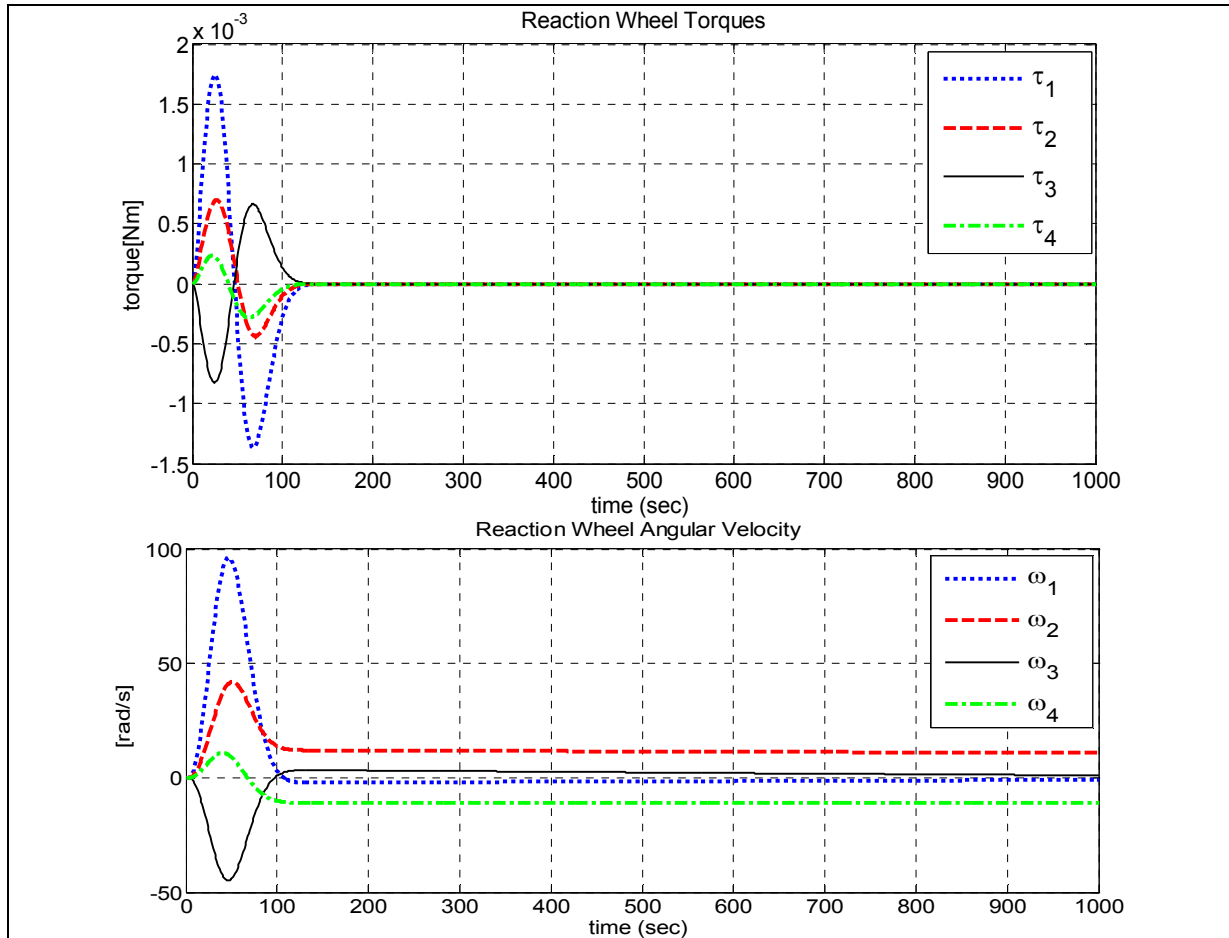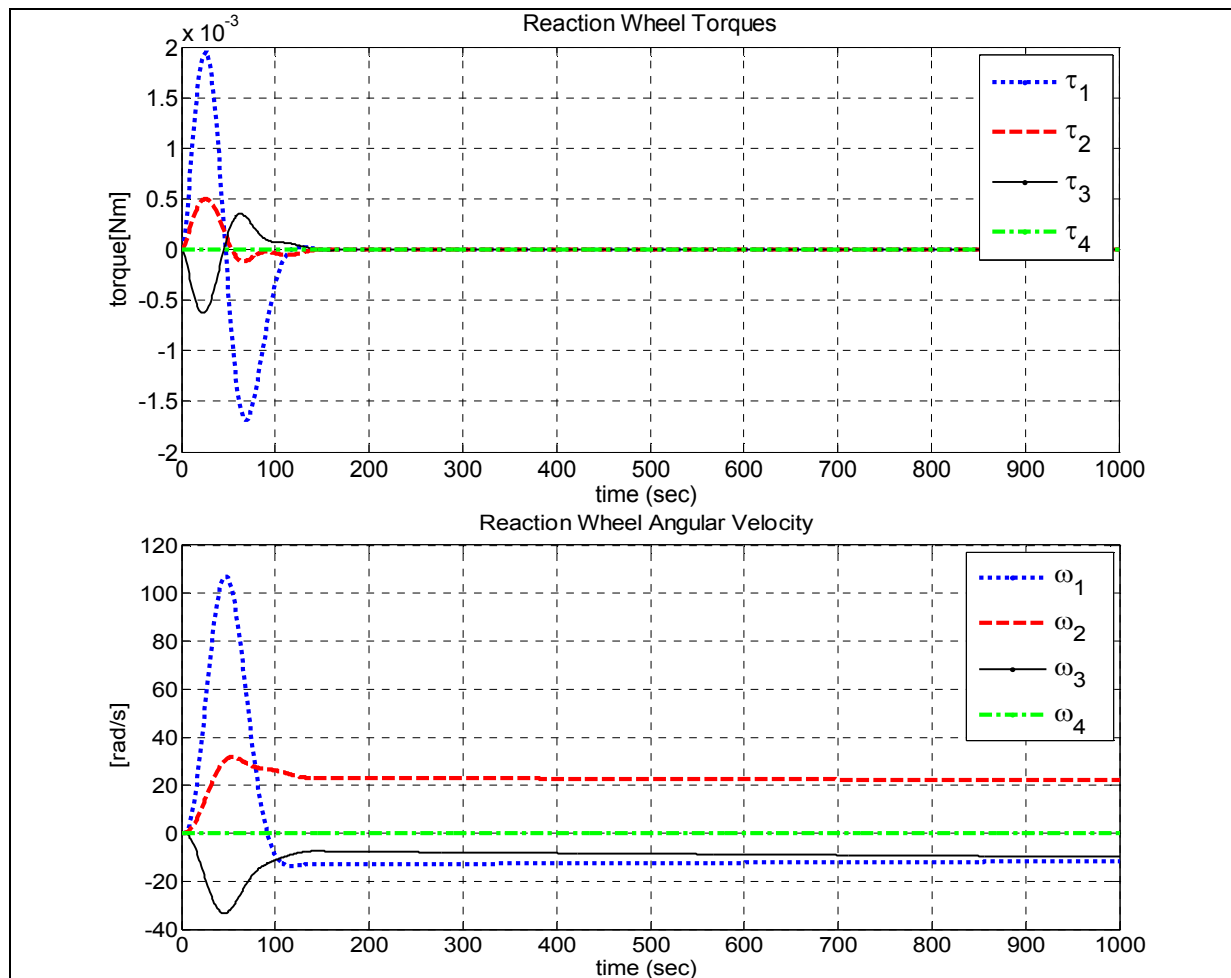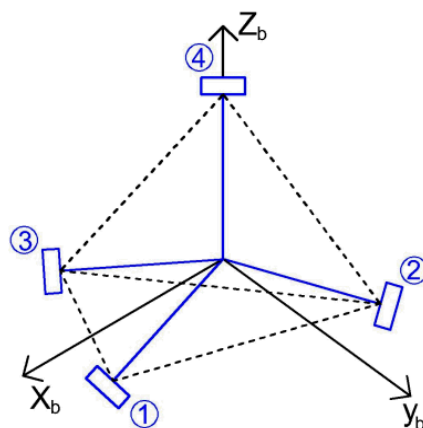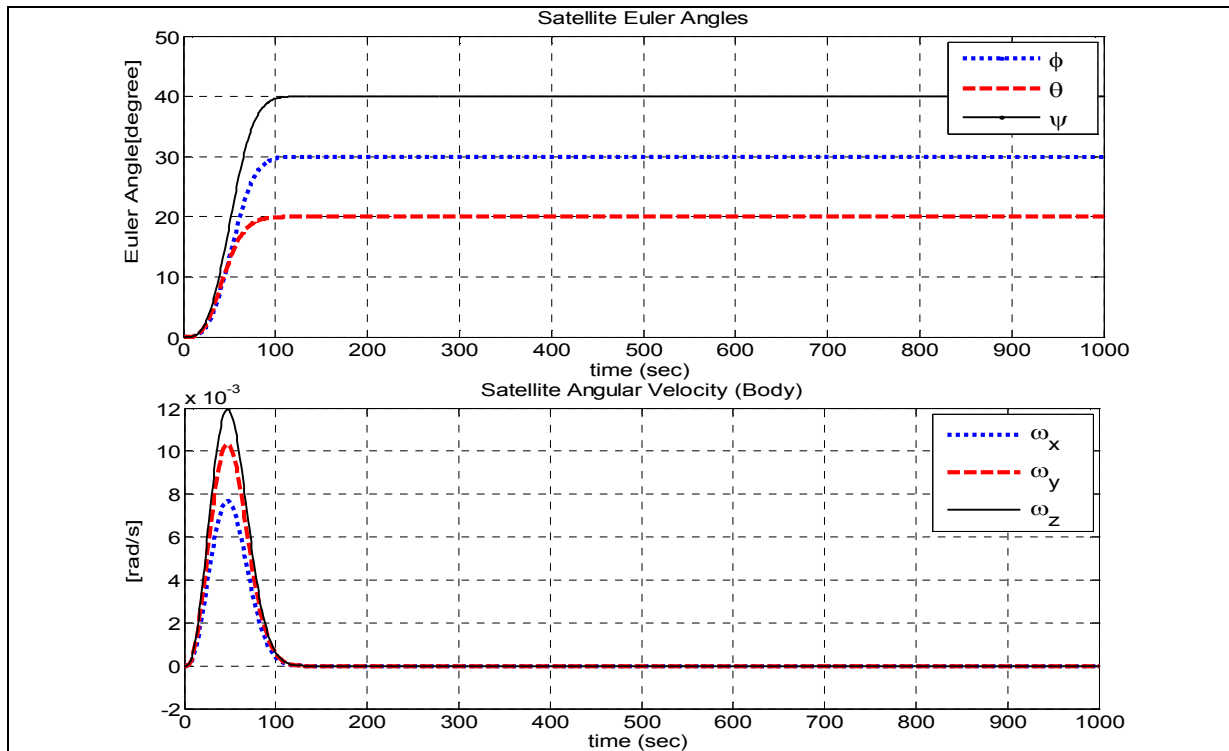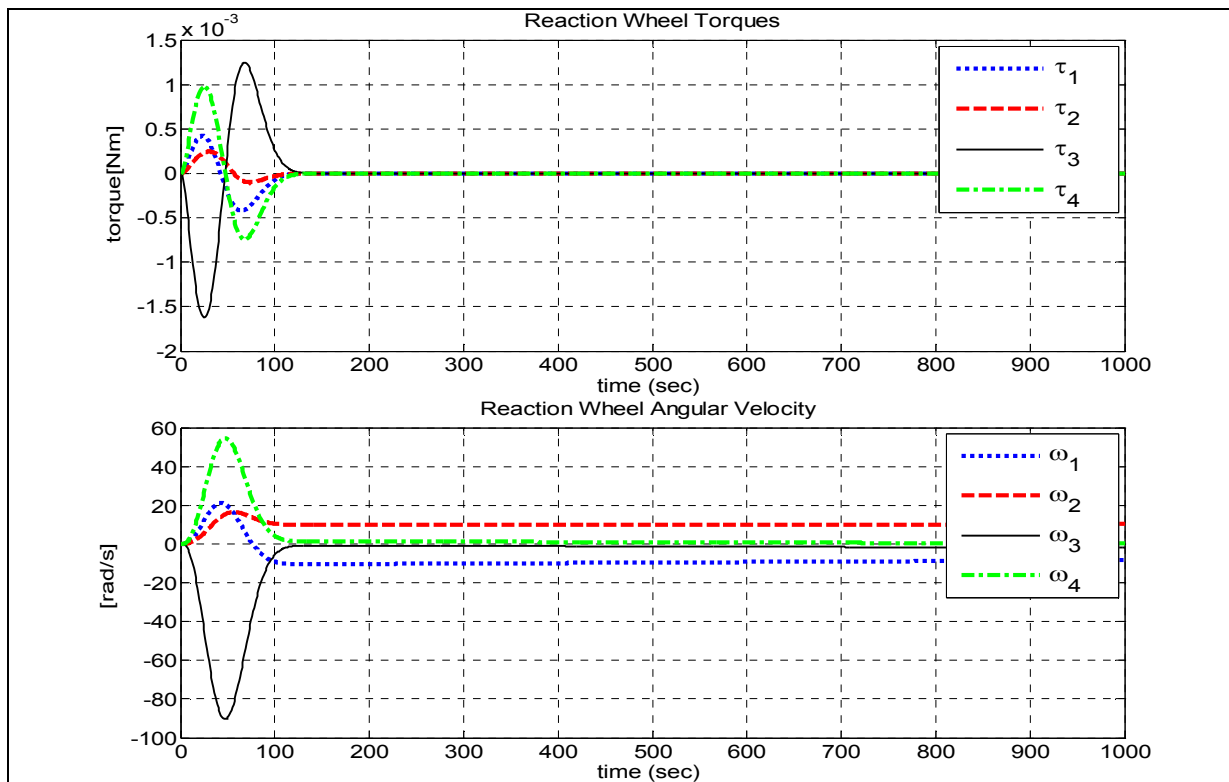
Figure 5.26 – Reaction wheel torques and angular velocities of Sliding Mode for pyramid configuration

Reaction wheel torques reaches to zero after 127 seconds. Maximum reaction wheel velocity is 96 rad/s, which is higher than LQR controller. Consequently, power consumption is also higher compared to LQR controller, which is 0.0066 W.

5.2.1.1 Reaction Wheel-1 Failure
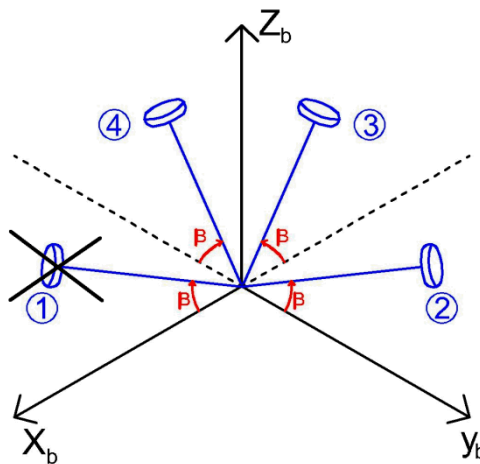
Figure 5.27 – System response of Sliding Mode for pyramid configuration, wheel-1 disabled

The system reaches to desired Euler angles in 159 seconds. The settling time for the satellite angular velocity is 169 seconds. It is clear that the settling times get longer in the case of loss of one actuator.
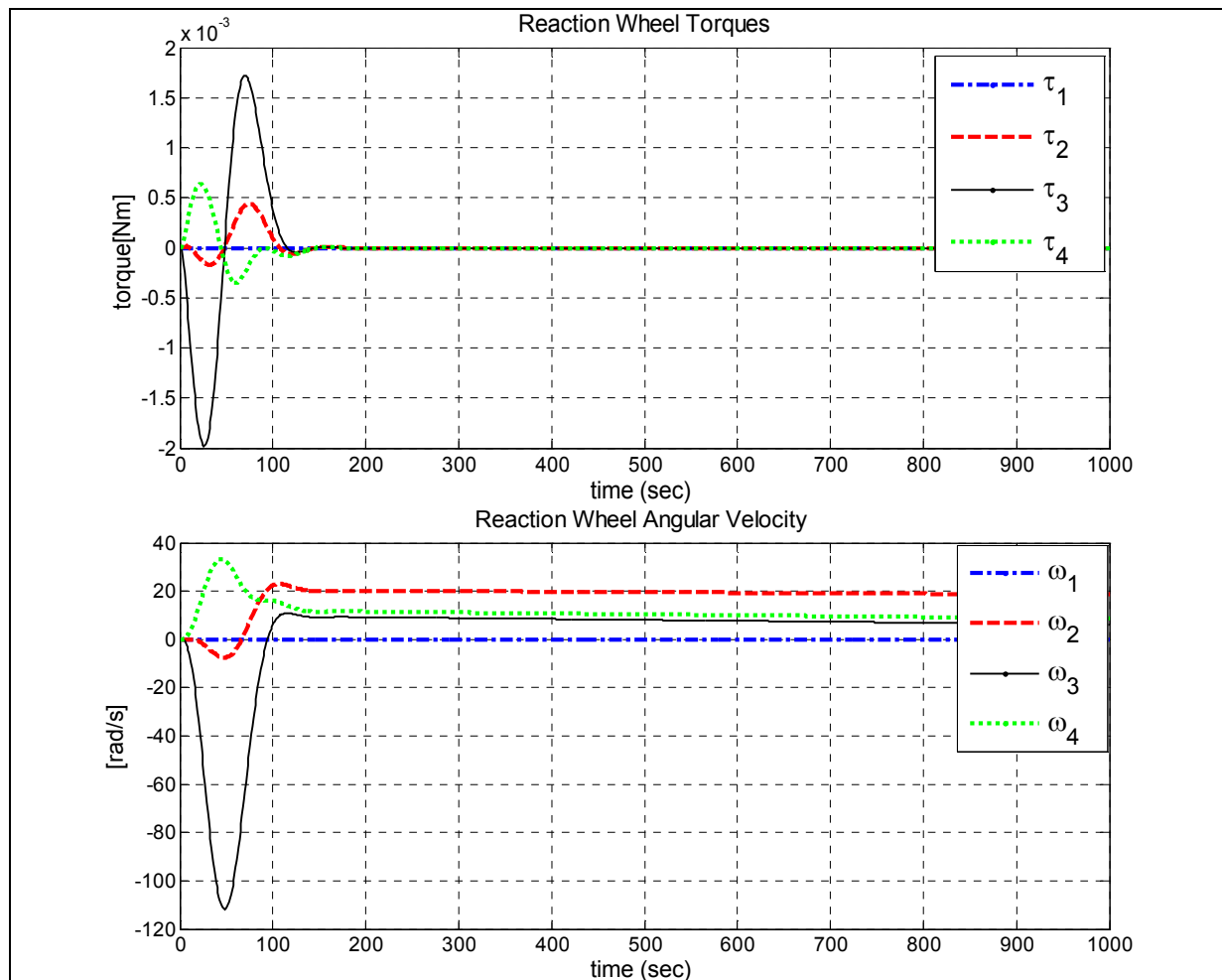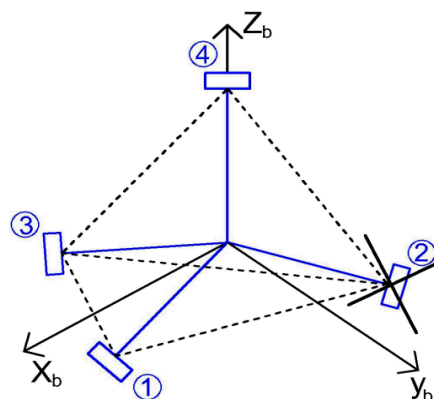

Figure 5.28 – Reaction wheel torques and angular velocities of Sliding Mode for pyramid configuration when wheel-1 disabled

Reaction wheel torques reaches to zero after 173 seconds. Maximum reaction wheel velocity is 146 rad/s, which is higher compared to the case without actuator loss. As a result the power consumption also increases, which is 0.0280 W.
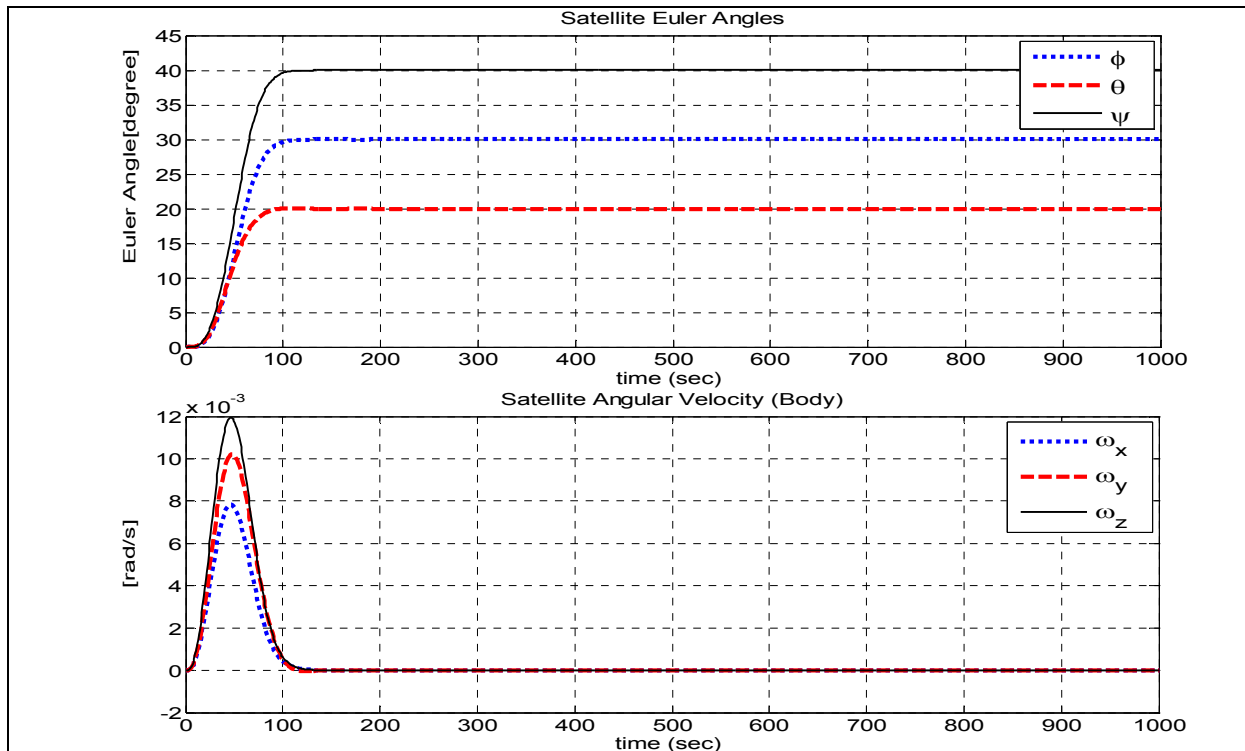
5.2.1.2 Reaction Wheel-2 Failure
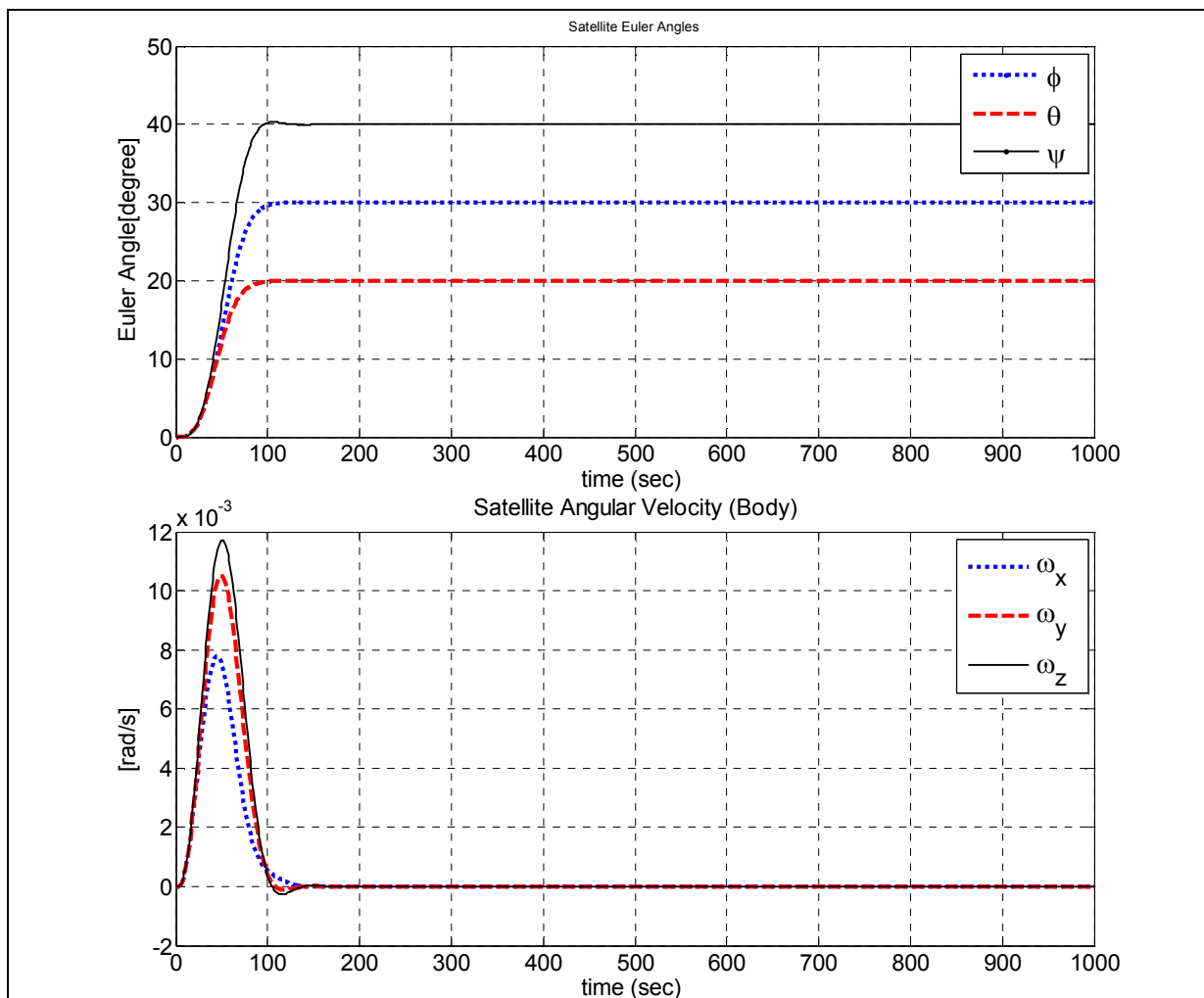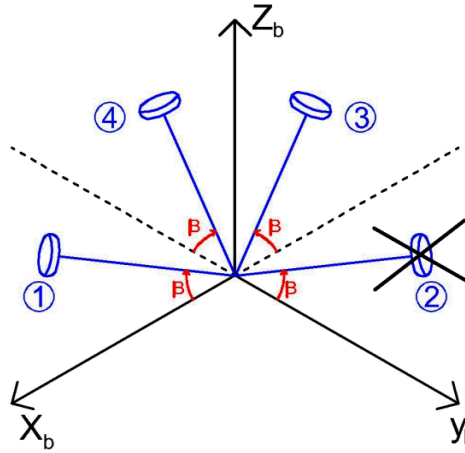
Figure 5.29 – System response of Sliding Mode for pyramid configuration when wheel-2 disabled

The system reaches to desired Euler angles in 156 seconds. The settling time for the satellite angular velocity is 166 seconds.
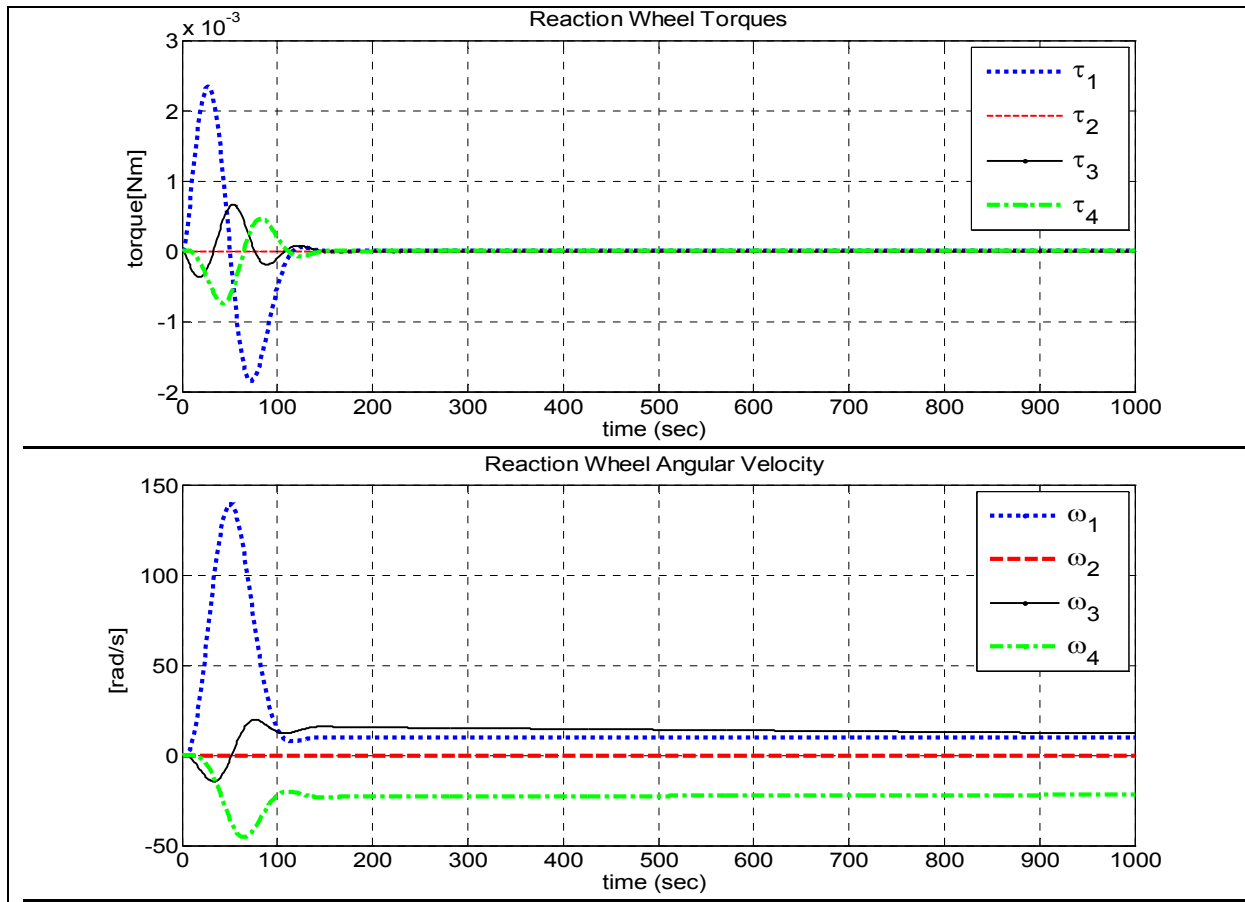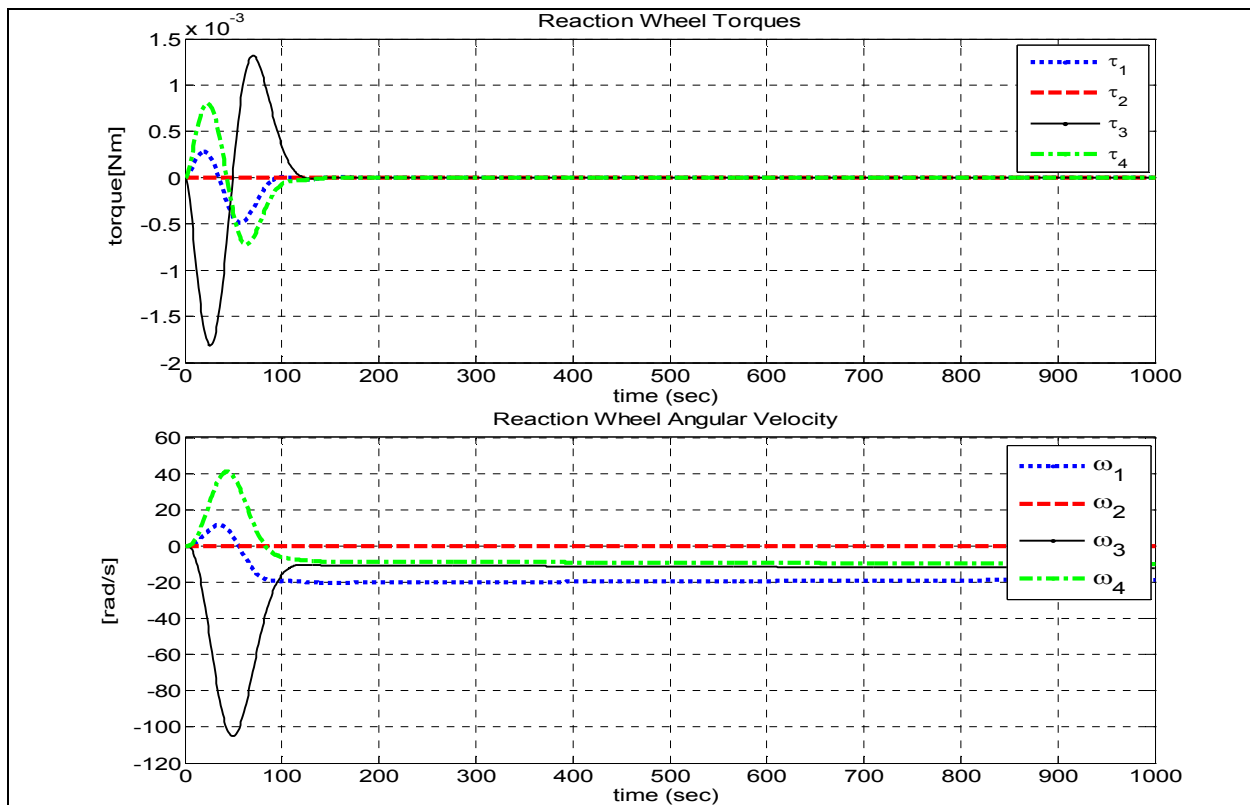

. **Figure 5.30** – Reaction wheel torques and angular velocities of Sliding Mode for pyramid configuration when wheel-2 disabled

Reaction wheel torques reaches to zero after 150 seconds. Maximum reaction wheel velocity is 138 rad/s. The total power consumption is 0.0109 W, which is much lower compared to the wheel-1 failure case.
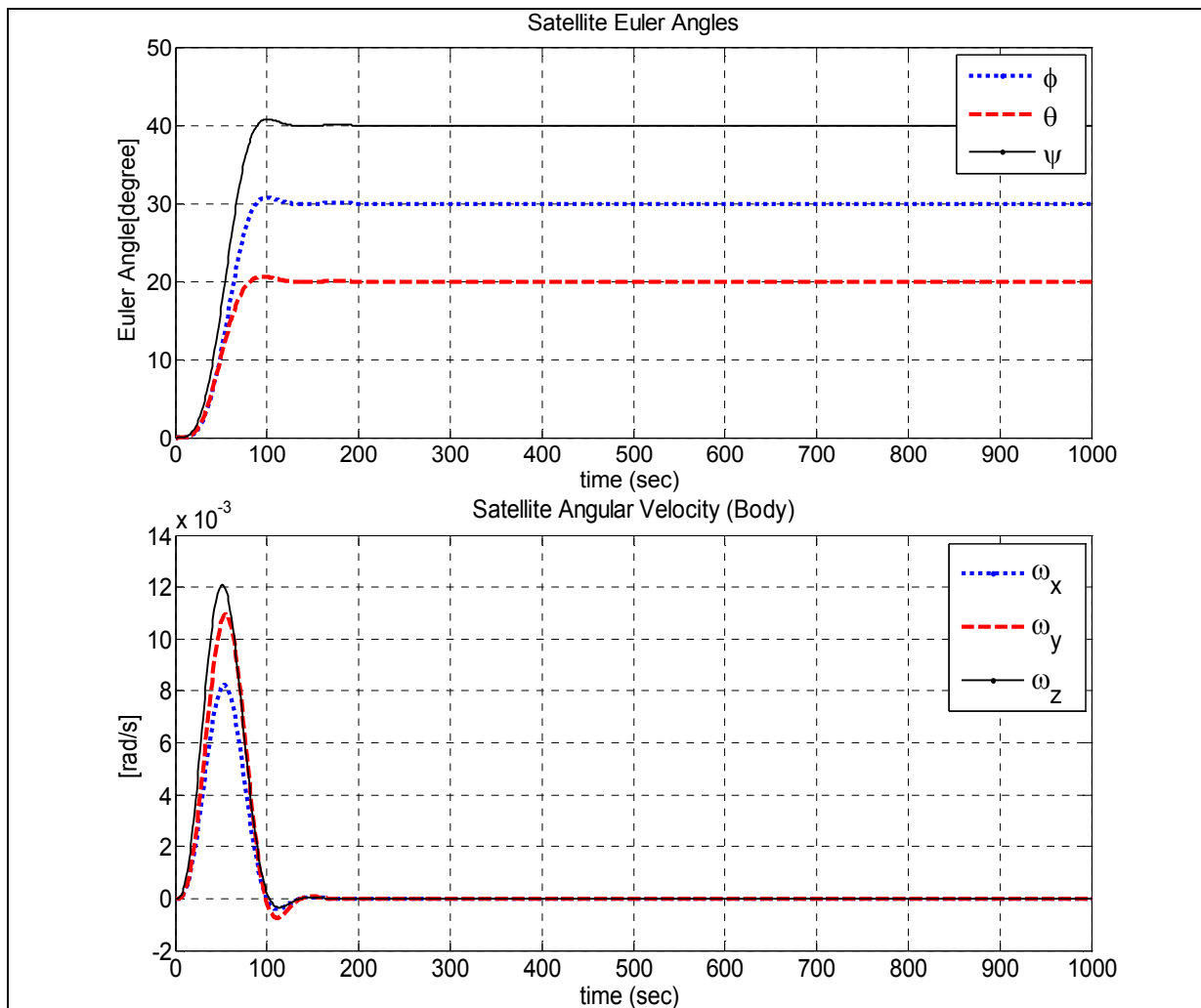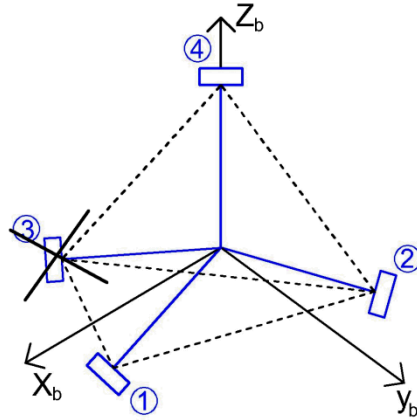
5.2.1.3 Reaction Wheel-3 Failure
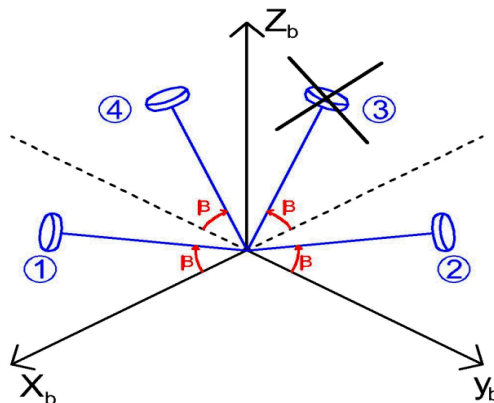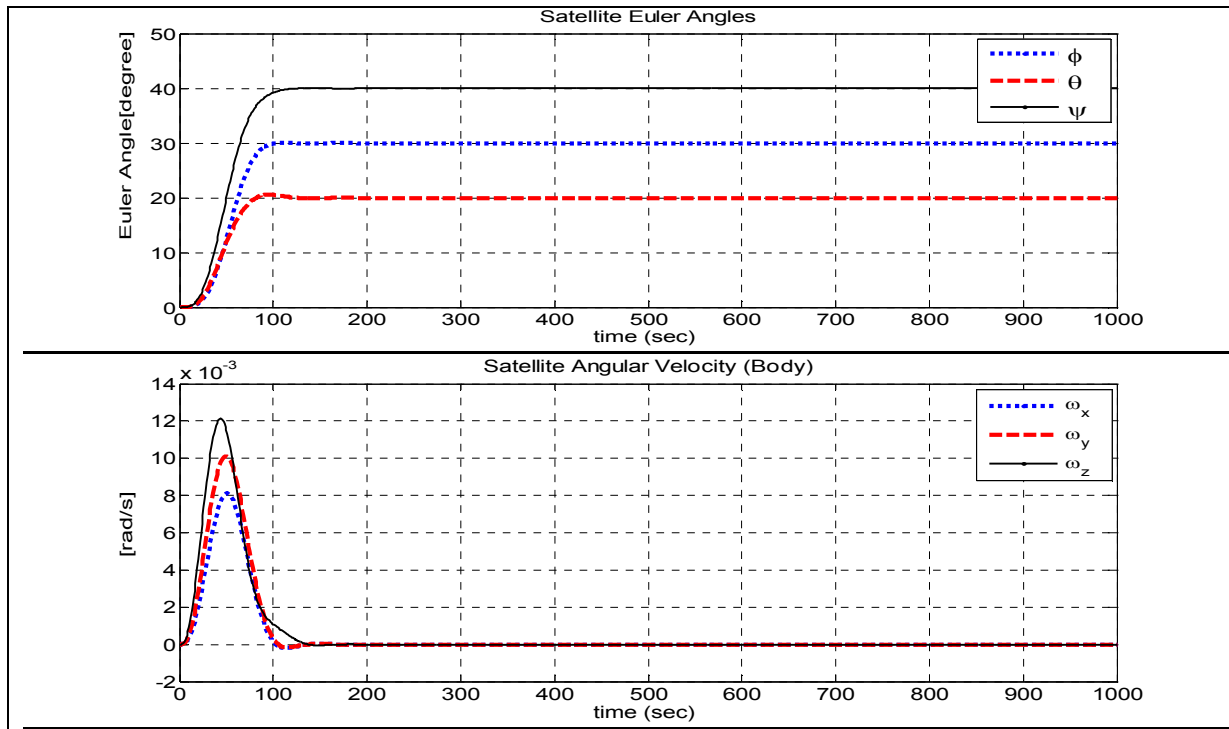
Figure 5.31 – System response of Sliding Mode for pyramid configuration when wheel-3 disabled

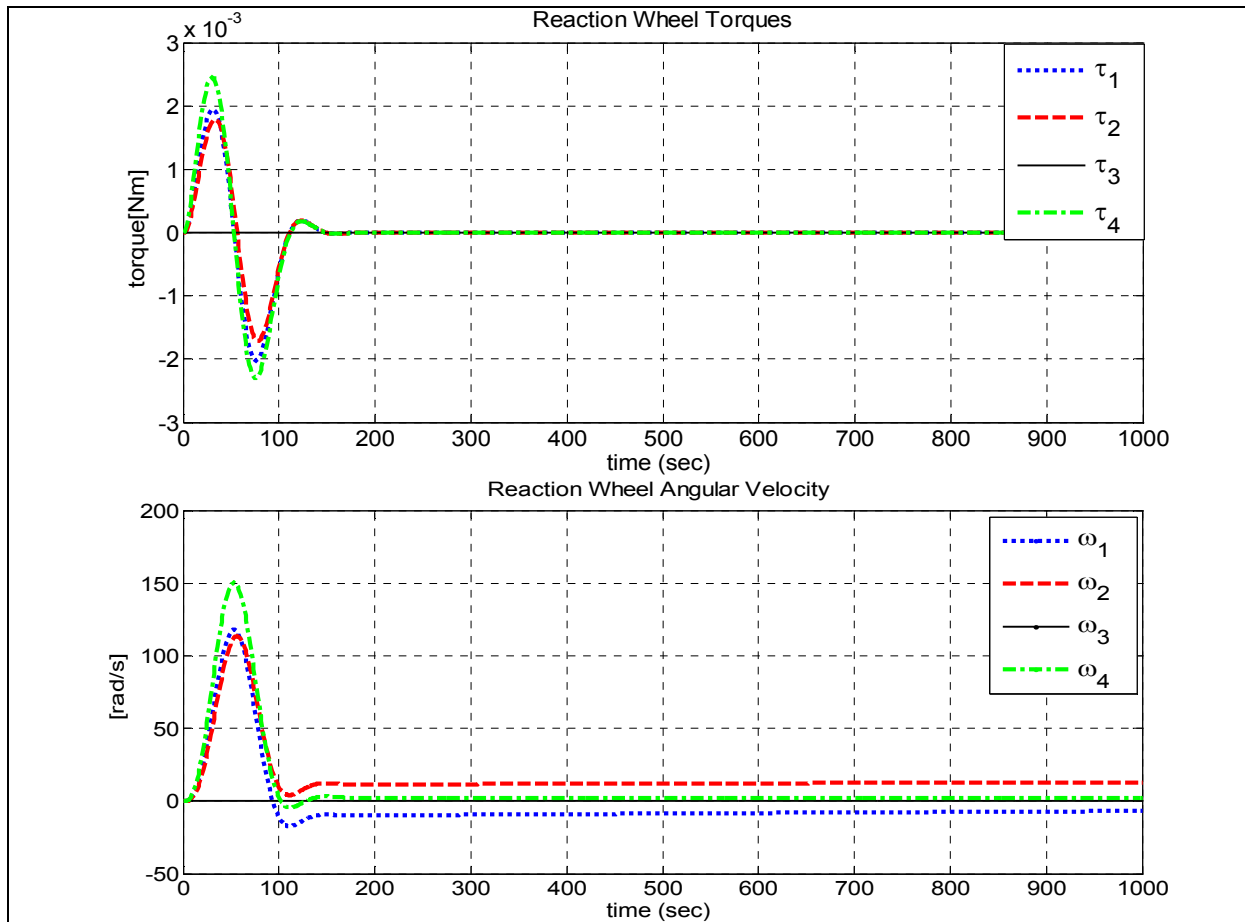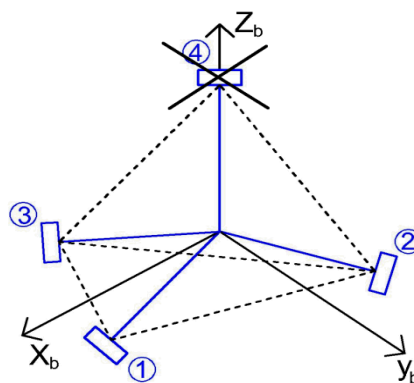The system reaches to desired Euler angles in 156 seconds. The settling time for the satellite angular velocity is 166 seconds. These settling times are the same with wheel-2 failure case.
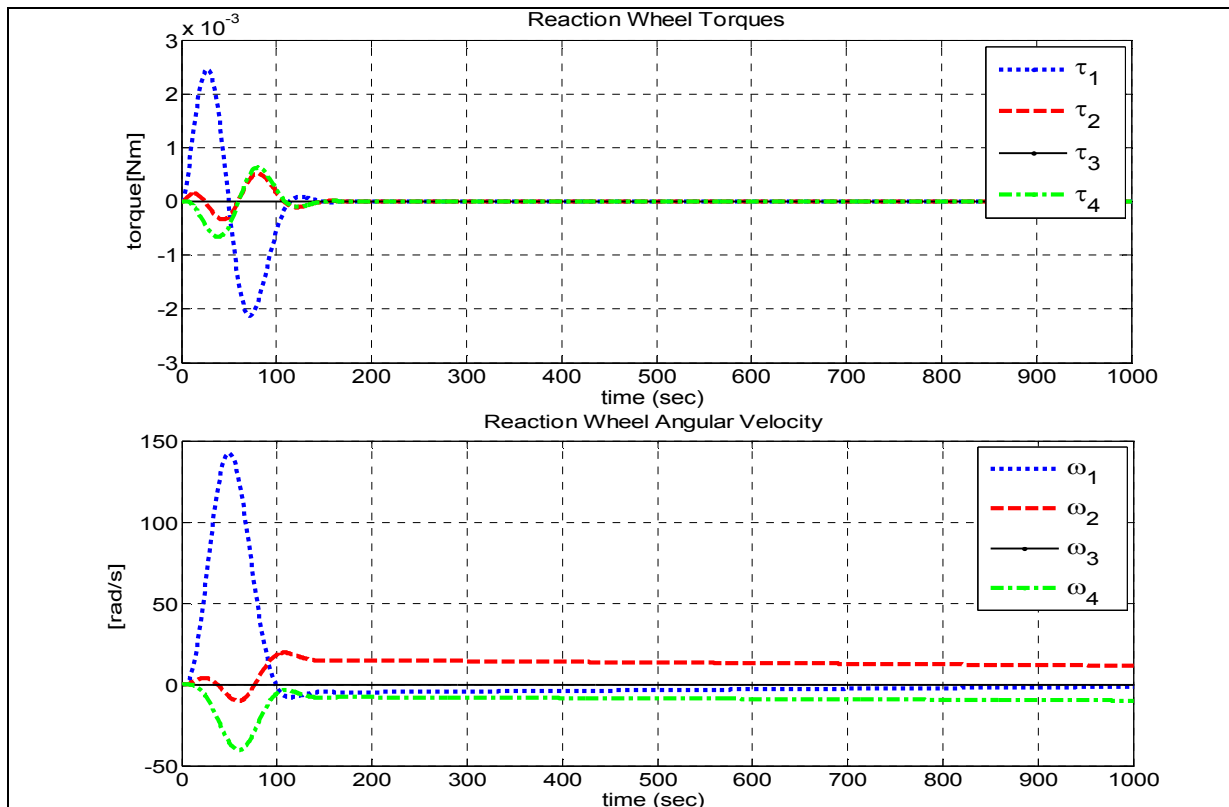
Figure 5.32 – Reaction wheel torques and angular velocities of Sliding Mode for pyramid configuration when wheel-3 disabled

Reaction wheel torques reaches to zero after 161 seconds. Maximum reaction wheel velocity is 142 rad/s. The total power consumption is 0.0112 W, which is very close to wheel-2 failure case.
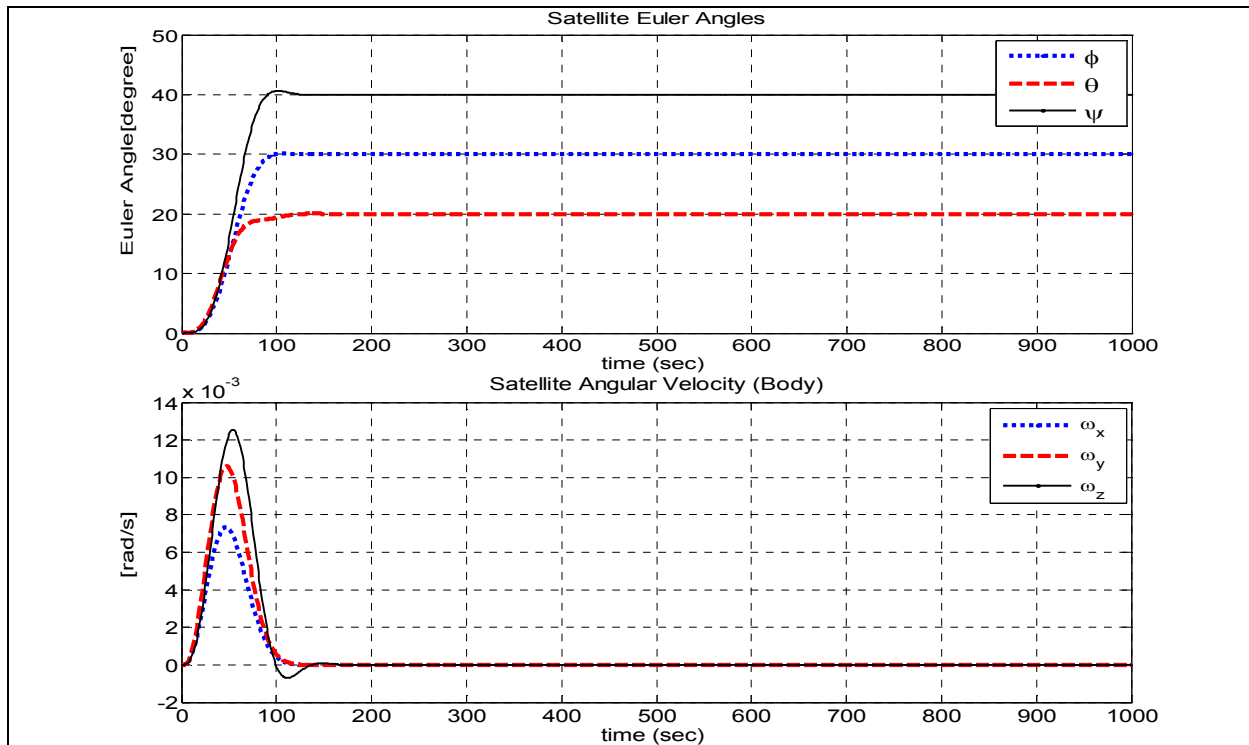
5.2.1.4 Reaction Wheel-4 Failure

Figure 5.33 – System response of Sliding Mode for pyramid configuration when wheel-4 disabled

The system reaches to desired Euler angles in 147 seconds, which is lower than other wheel failure cases. The settling time for the satellite angular velocity is 158 seconds.
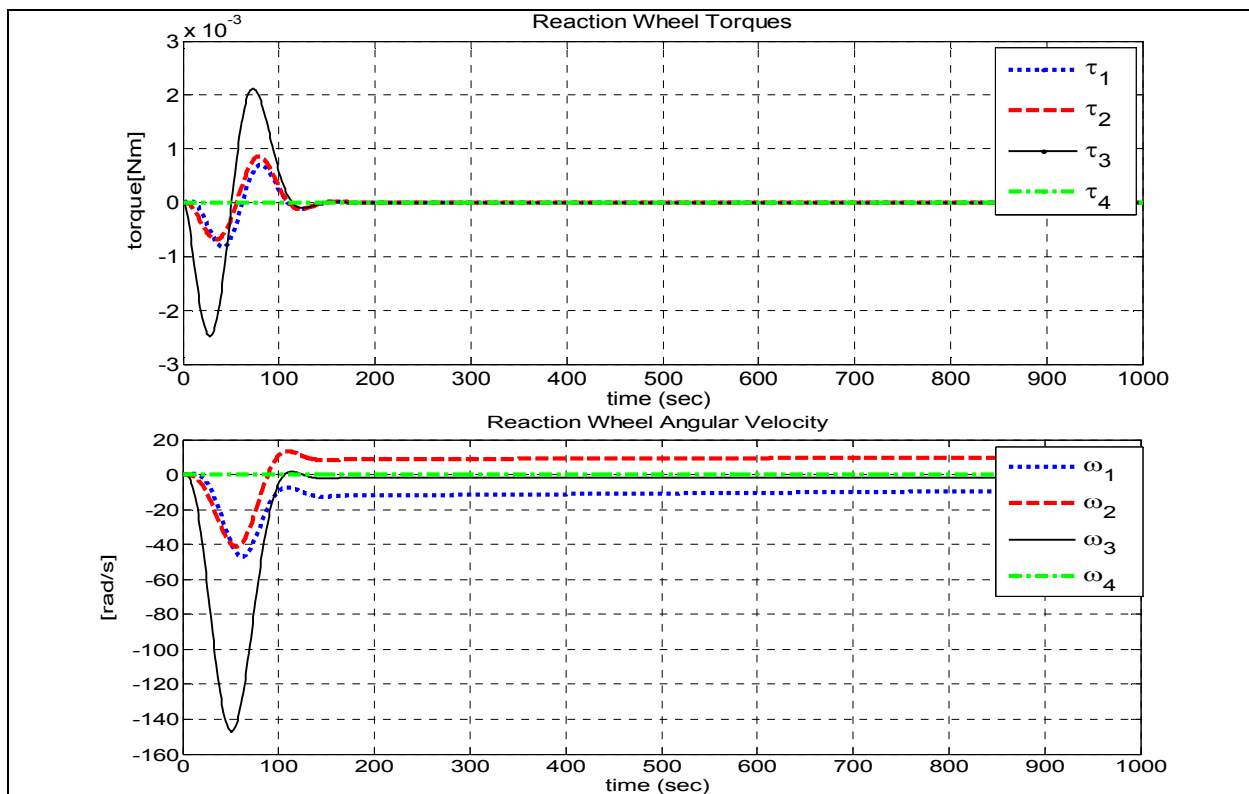
Figure 5.34 – Reaction wheel torques and angular velocities of Sliding Mode for pyramid configuration when wheel-4 disabled

Reaction wheel torques reaches to zero after 140 seconds. Maximum reaction wheel velocity is 107 rad/s, which is lower than other wheel failure case. Therefore total power consumption is also lower, which is 0.0067 W.
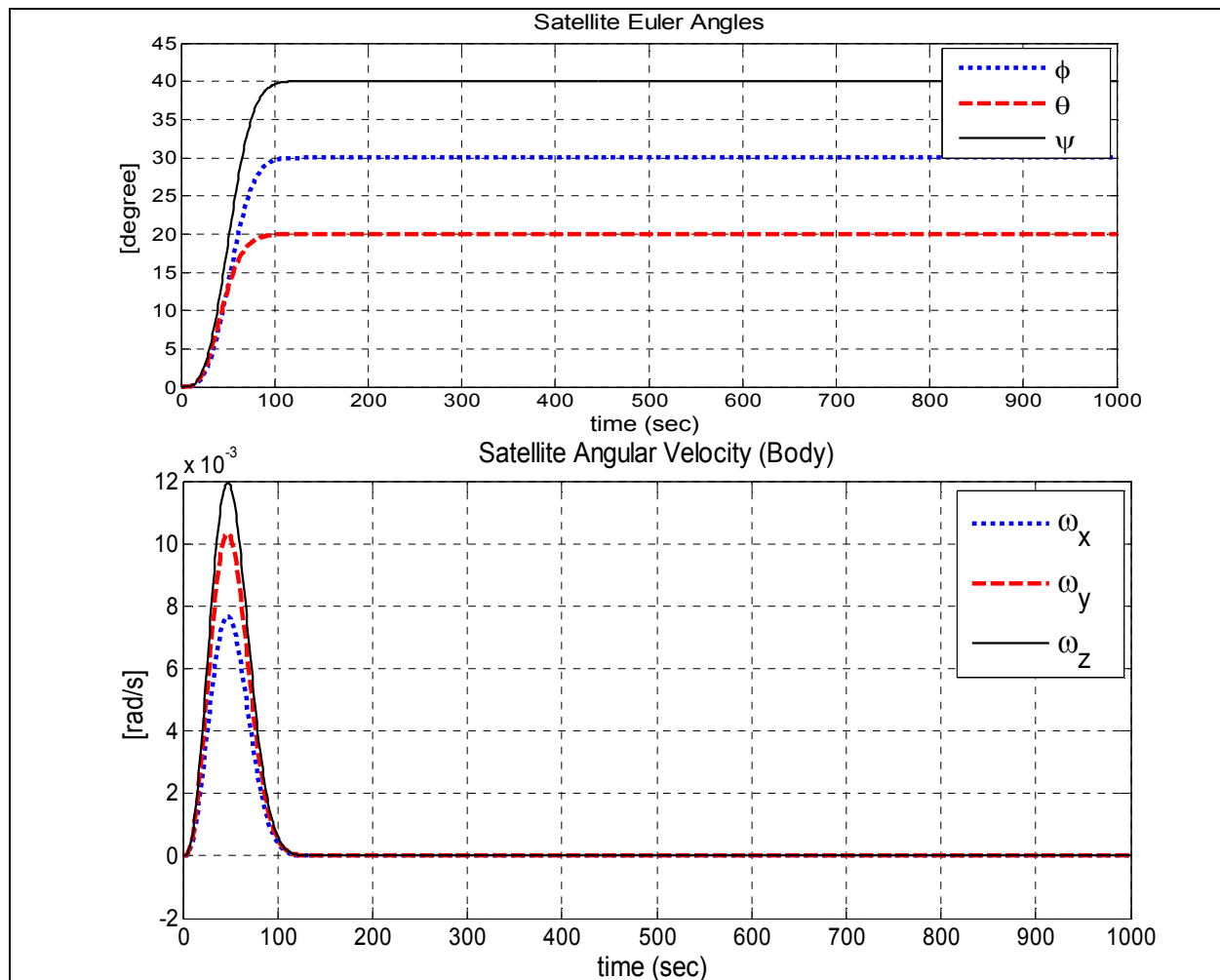
5.2.2 Tetrahedron Configuration

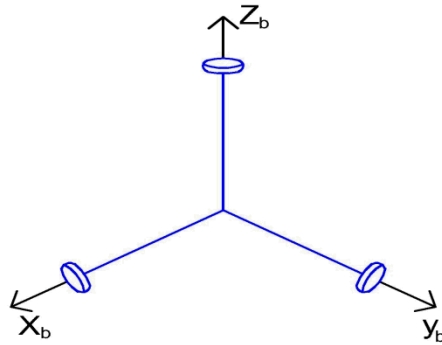**Figure 5.35** – System response of Sliding Mode for tetrahedron configuration

The system reaches to desired Euler angles in 122 seconds. The settling time for the satellite angular velocity is 128 seconds. These settling times are lower compared to LQR tetrahedron configuration.
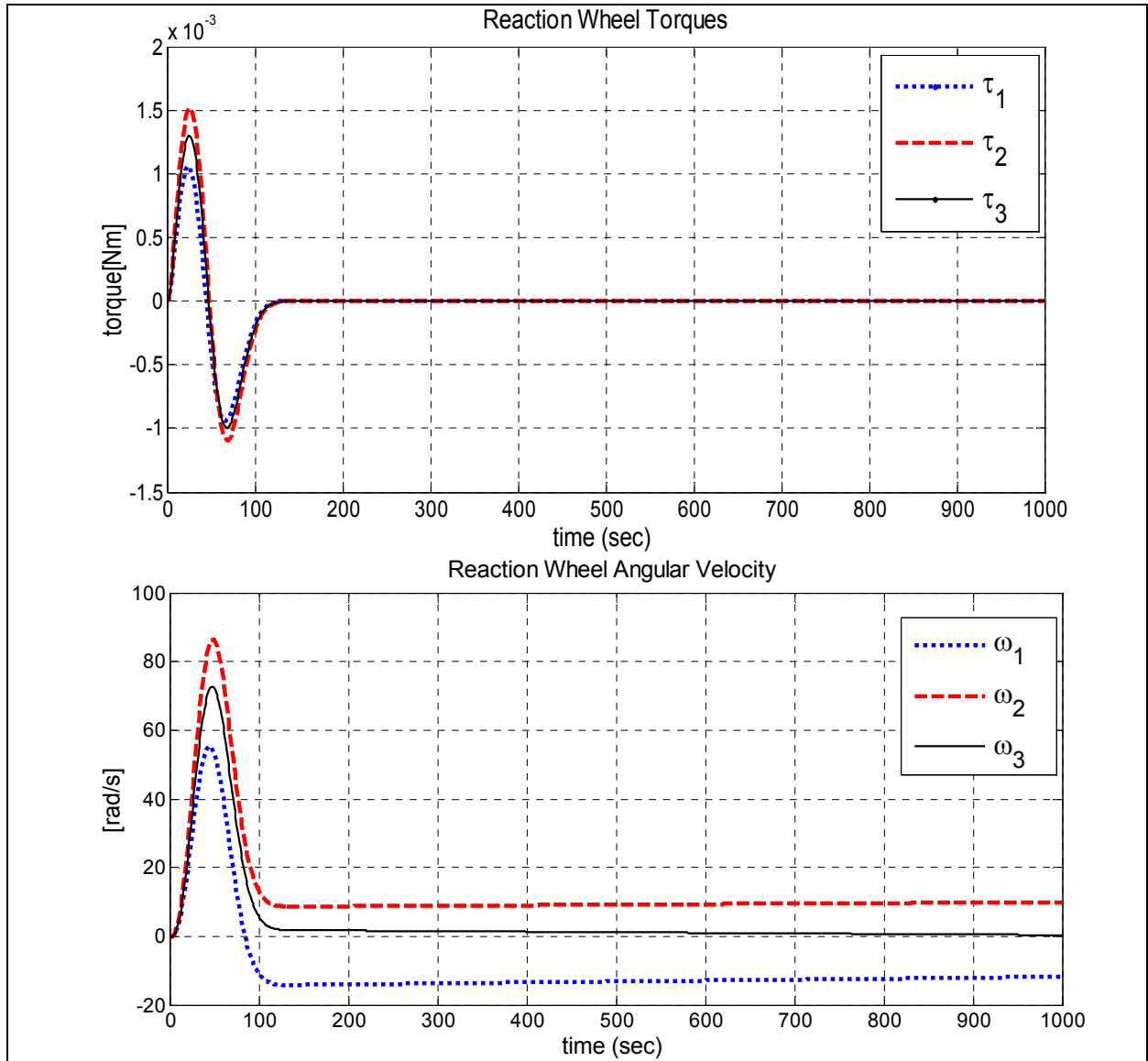

Figure 5.36 – Reaction wheel torques and angular velocities of Sliding Mode for tetrahedron configuration

Reaction wheel torques reaches to zero after 126 seconds. Maximum reaction wheel velocity is 90 rad/s, which is higher than the LQR tetrahedron case. Therefore the power consumption is also higher compared to LQR tetrahedron case, which is 0.0059 W.

5.2.2.1 Reaction Wheel-1 Failure
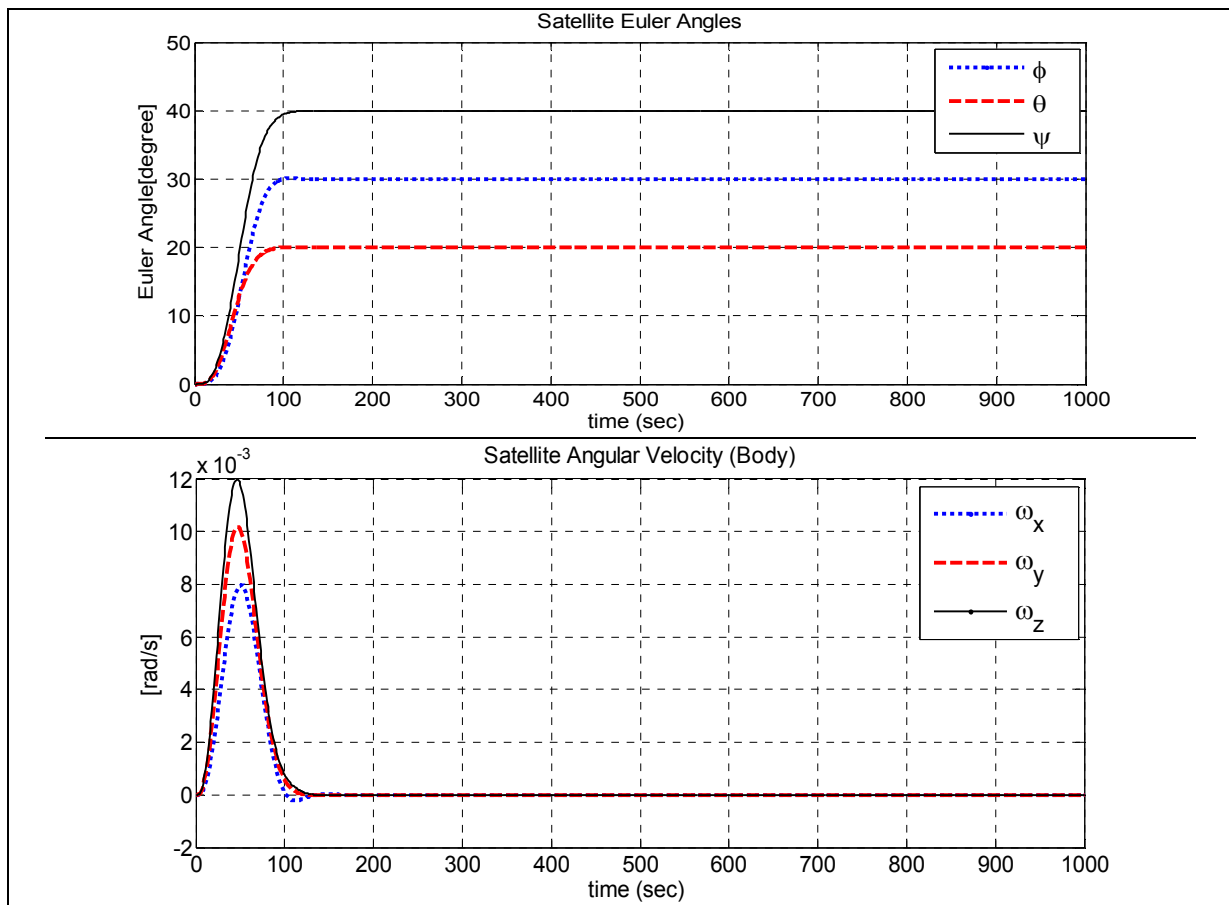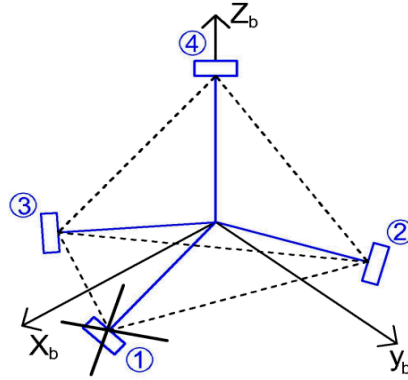
Figure 5.37 – System response of Sliding Mode for tetrahedron configuration when wheel-1 disabled

The system reaches to desired Euler angles in 151 seconds. The settling time for the satellite angular velocity is 162 seconds. It is clear that, settling times increase in the case of an actuator loss.

Figure 5.38 – Reaction wheel torques and angular velocities of Sliding Mode for tetrahedron configuration when wheel-1 disabled

Reaction wheel torques reaches to zero after 145 seconds. Maximum reaction wheel velocity is 111 rad/s. Total power consumption in Sliding Mode tetrahedron configuration when wheel-1 disabled is much lower than pyramid configuration wheel-1 failure case, which is 0.0070 W.

5.2.2.2 Reaction Wheel-2 Failure

Figure 5.39 – System response of Sliding Mode for tetrahedron configuration when wheel-2 disabled

The system reaches to desired Euler angles in 126 seconds. The settling time for the satellite angular velocity is 137 seconds.

Figure 5.40 – Reaction wheel torques and angular velocities of Sliding Mode for tetrahedron configuration when wheel-2 disabled

Reaction wheel torques reaches to zero after 140 seconds. Maximum reaction wheel velocity is 105 rad/s. Total power consumption is 0.0066 W.

5.2.2.3 Reaction Wheel-3 Failure

Figure 5.41 – System response of Sliding Mode for tetrahedron configuration when wheel-3 disabled

The system reaches to desired Euler angles in 158 seconds. The settling time for the satellite angular velocity is 168 seconds.

Figure 5.42 – Reaction wheel torques and angular velocities of Sliding Mode for tetrahedron configuration when wheel-3 disabled

Reaction wheel torques reaches to zero after 172 seconds. Maximum reaction wheel velocity is 150 rad/s. Total power consumption is 0.0249 W, which is much higher than the other wheel failure cases.

5.2.2.4 Reaction Wheel-4 Failure

Figure 5.43 – System response of Sliding Mode for tetrahedron configuration when wheel-4 disabled

The system reaches to desired Euler angles in 157 seconds. The settling time for the satellite angular velocity is 168 seconds.

Figure 5.44 – Reaction wheel torques and angular velocities of Sliding Mode for tetrahedron configuration when wheel-4 disabled

Reaction wheel torques reaches to zero after 170 seconds. Maximum reaction wheel velocity is 146 rad/s. Total power consumption is 0.0129 W.

5.2.3 Standard 3-wheel Configuration

Figure 5.45 – System response of Sliding Mode for standard 3-wheel configuration

The system reaches to desired Euler angles in 122 seconds. The settling time for the satellite angular velocity is 130 seconds. The settling times are almost the same as pyramid and tetrahedron configurations.

Figure 5.46 – Reaction wheel torques and angular velocities of Sliding Mode for 3-wheel configuration

Maximum reaction wheel velocity is 86 rad/s. Power consumption is higher compared to pyramid and tetrahedron configurations, which is 0.0080 W.

5.3 Integrator Backstepping Controller Simulation Results

Control input for linear quadratic regulator controller is defined in Chapter 4 as:

$$u = -K_2 z_2 - G z_1 + \omega_{ib}^b \times (I\omega_b + h_w) - \omega_o IS(c_2)\omega_{ib}^b + I\dot{\alpha}_1 - T_d \qquad (5.6)$$

Controller parameters used in the simulation are given below:

Parameter	Value
Initial Angular Velocity	$\omega_{bo}^{b} = [0\ 0\ 0]^{T}$
Initial Euler Angles	$[\varnothing\ \theta\ \Psi] = [0\ 0\ 0]^{T}$
Control Weighting Matrices	K1 = 0.0001*eye(3); K2 = 5*eye(3);
Desired Euler Angles	$[\varnothing\ \theta\ \Psi] = [30\ 20\ 40]^{T}$
Cross-over frequency	$\omega_{n} = 0.02$
Relative damping factor	$\zeta = 1$
Maximum Wheel Torque	5 mNm

Table 5.4 - Simulation parameters of Integrator Backstepping Control

Implementation of the controller can be shown in flow chart as follows:

Loading the current and desired quaternion values

Loading the current and desired quaternion values

Loading angular velocity relative to inertial frame

Transformation of angular velocity into orbit frame

Creating control weight matrices

Calculation of state variables and stabilizing functions

Calculation of angular momentum of reaction wheels

Calculation of command torque
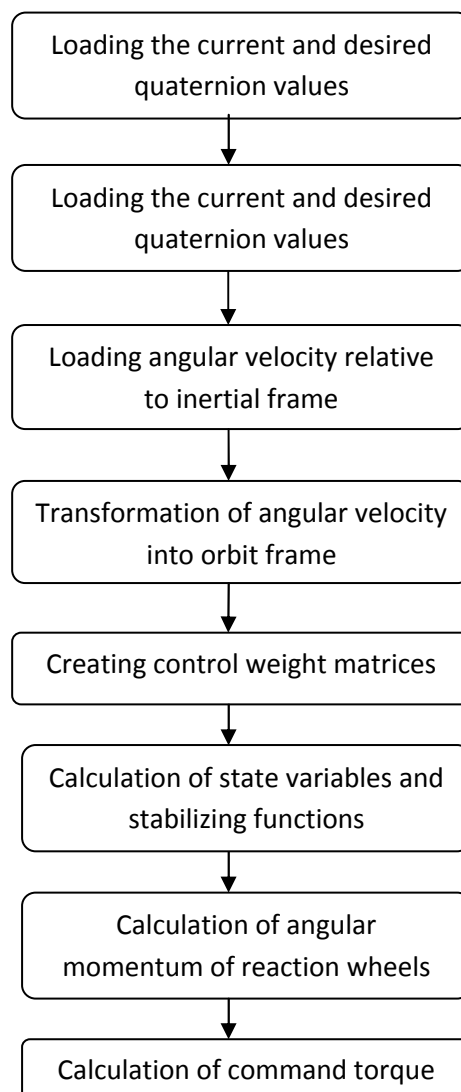
5.3.1 Pyramid Configuration
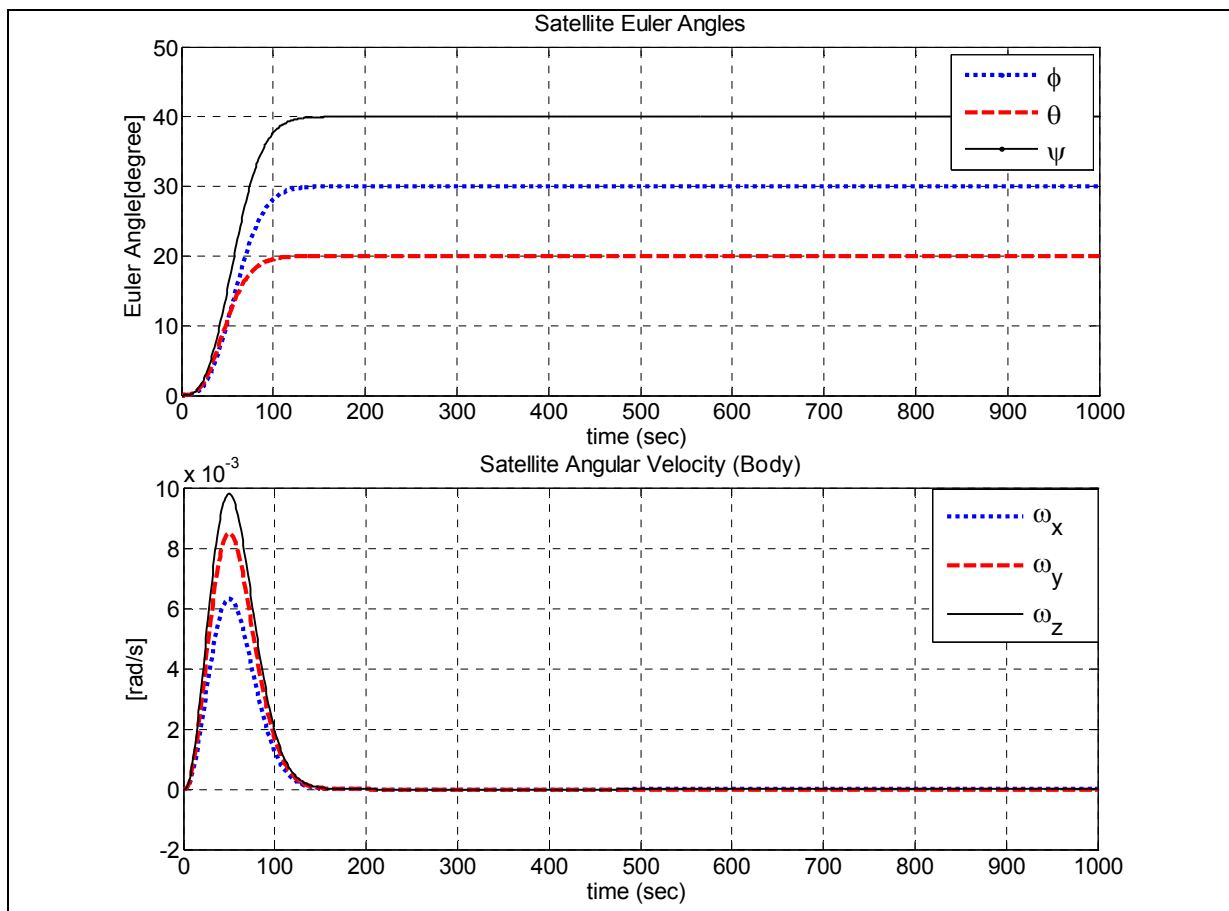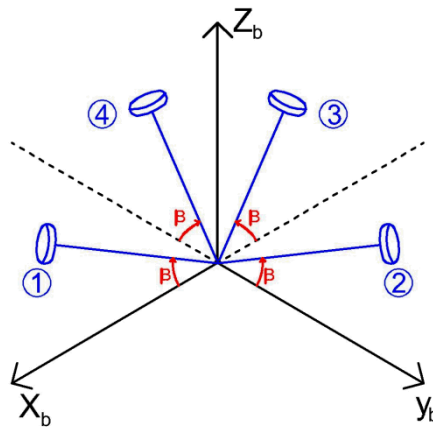
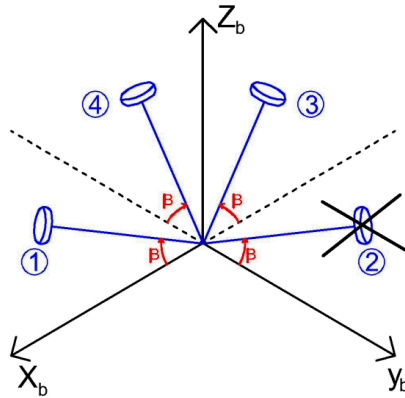**Figure 5.47** – System response of Integrator Backstepping for pyramid configuration

The system reaches to desired Euler angles in 166 seconds. The settling time for the satellite angular velocity is 170 seconds. These settling times are higher than Sliding Mode and close to LQR pyramid configurations.
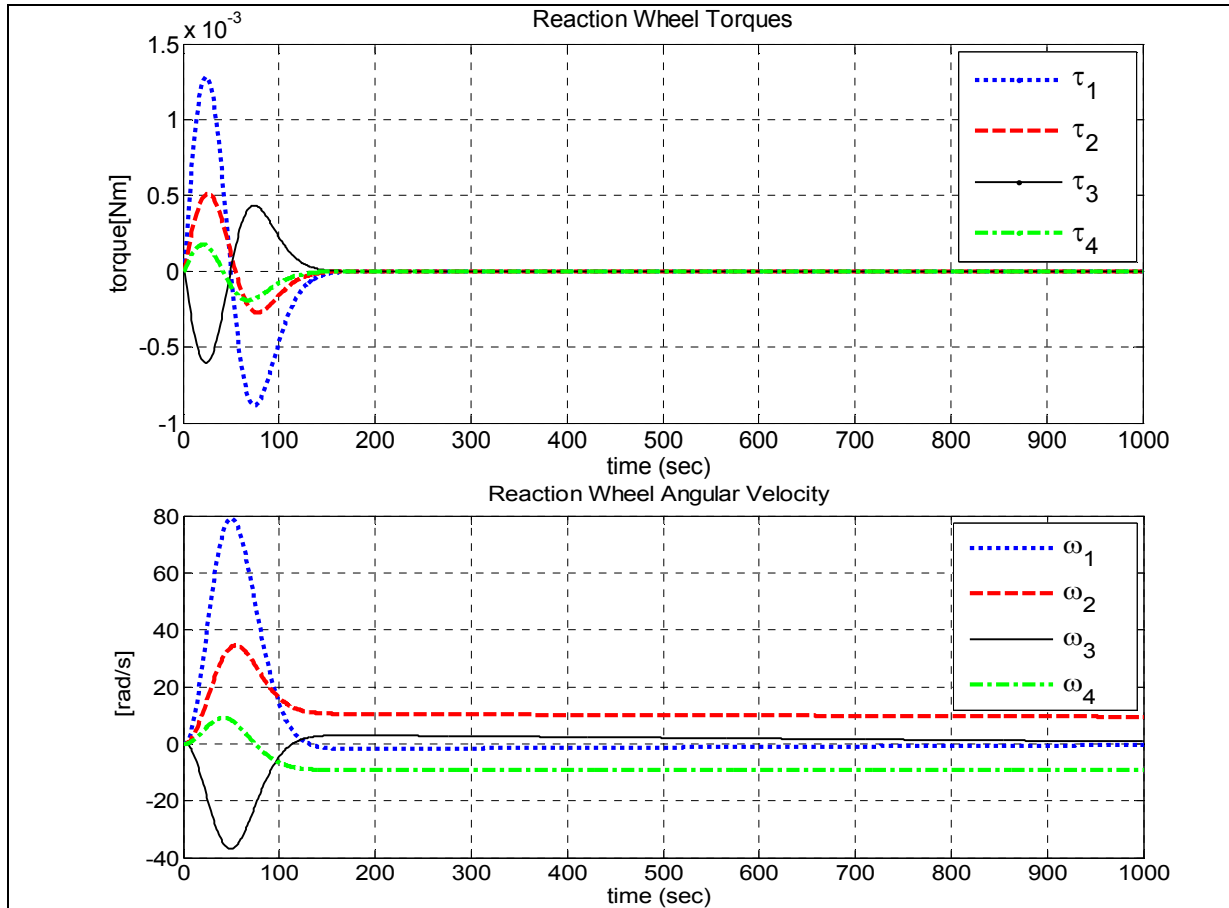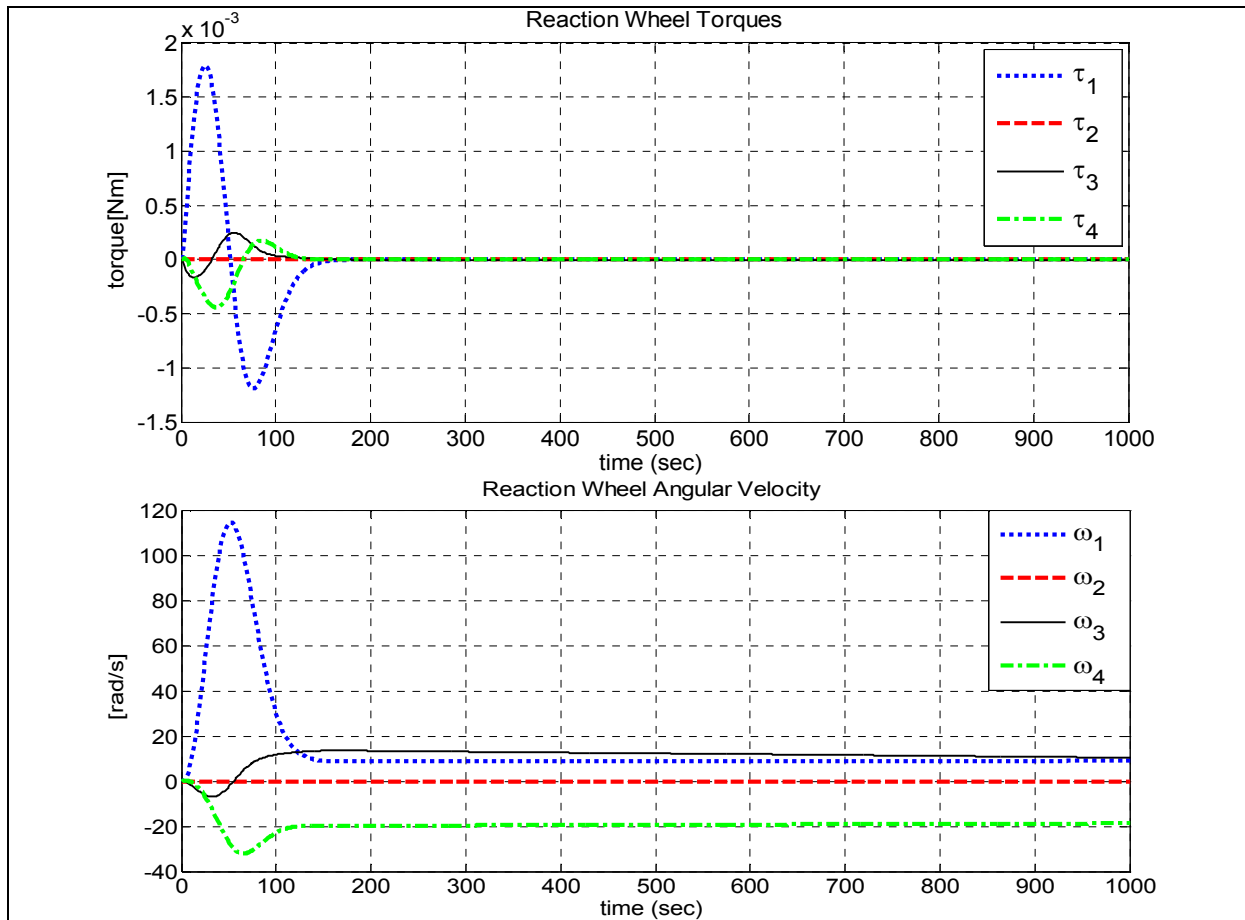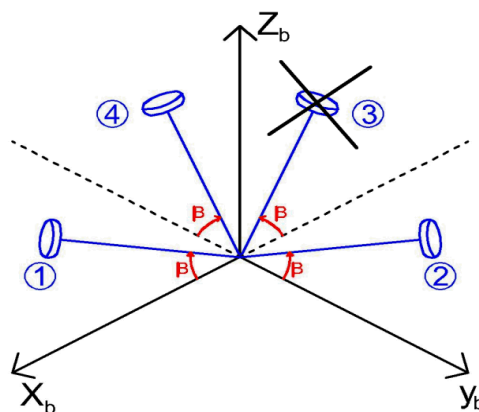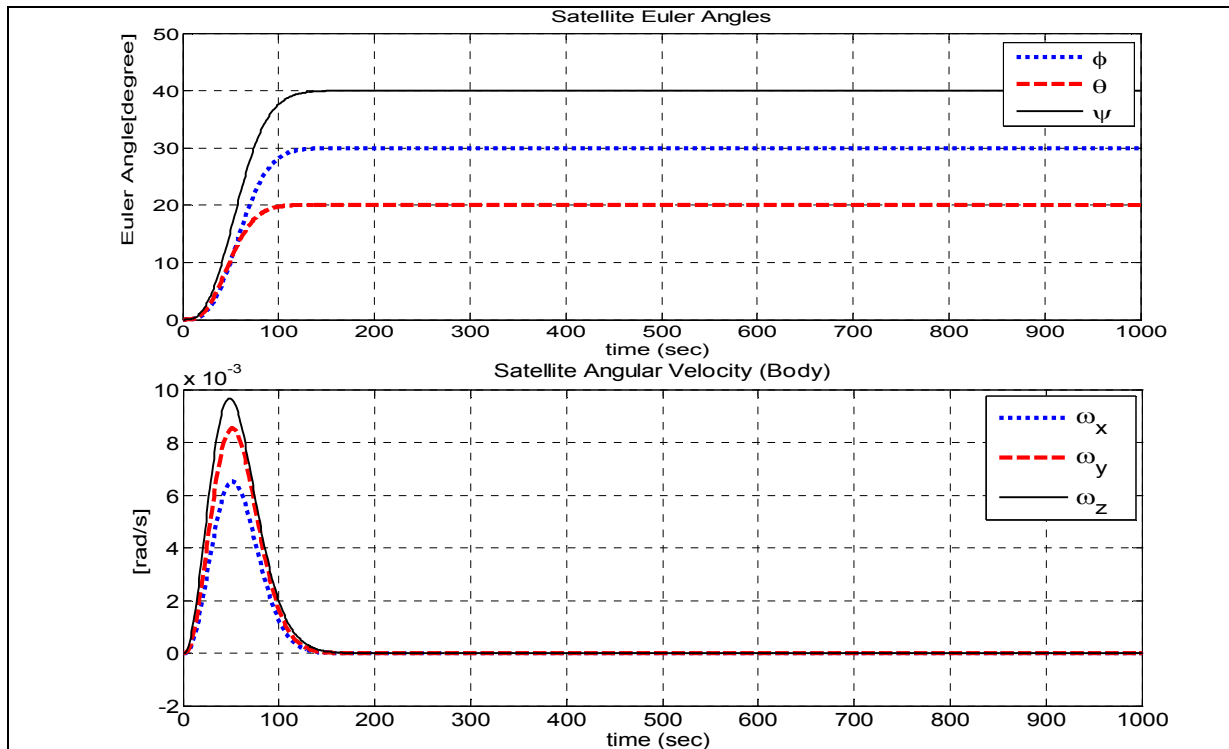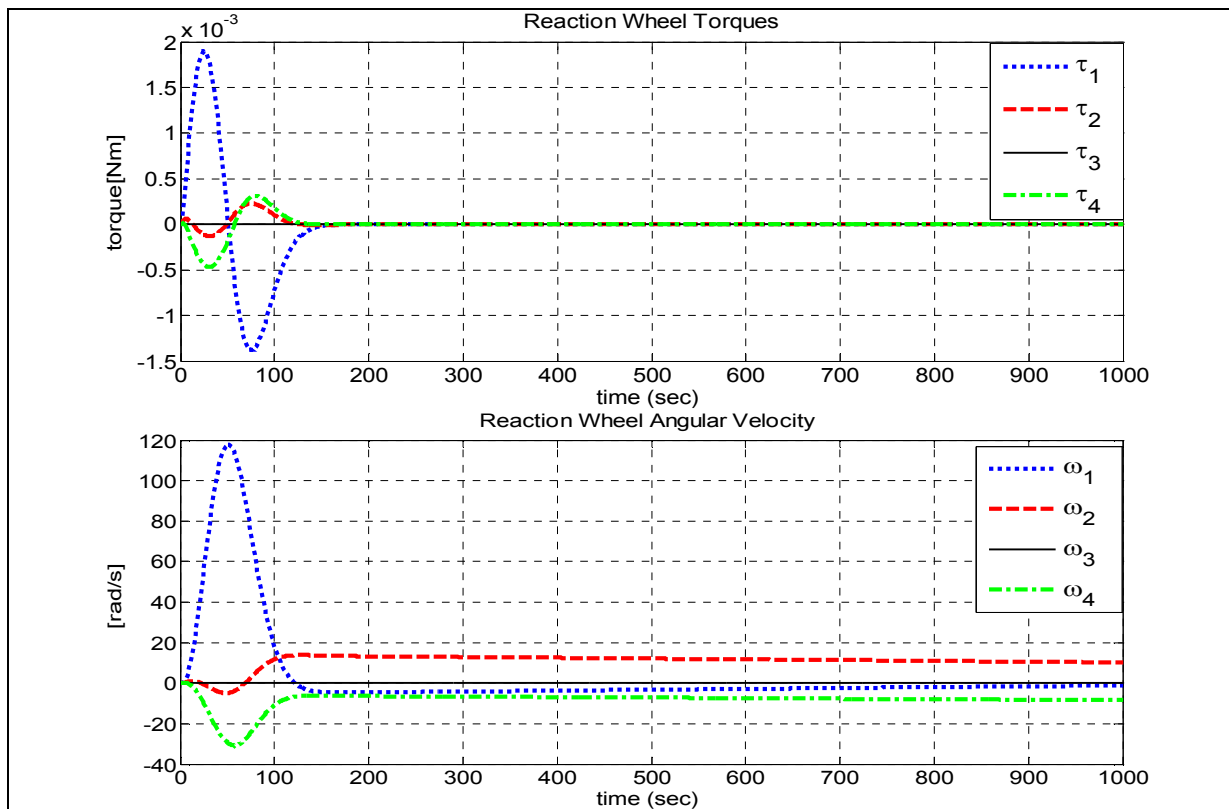
Figure 5.48 – Reaction wheel torques and angular velocities of Integrator Backstepping for pyramid configuration

Reaction wheel torques reaches to zero after 155 seconds. Maximum reaction wheel velocity is 79 rad/s. Power consumption is higher than LQR and lower than Sliding Mode pyramid configuration, which is 0.0045 W.

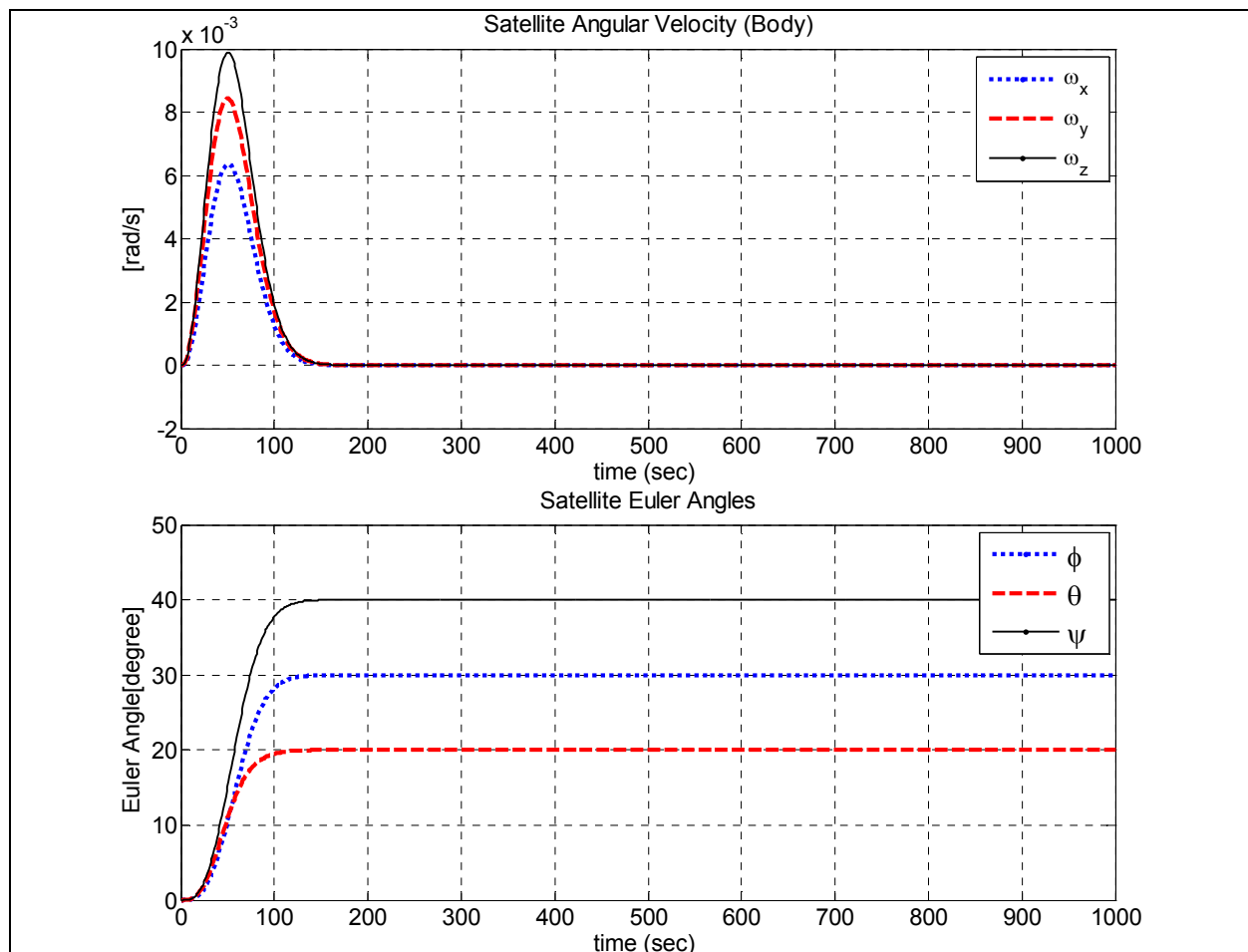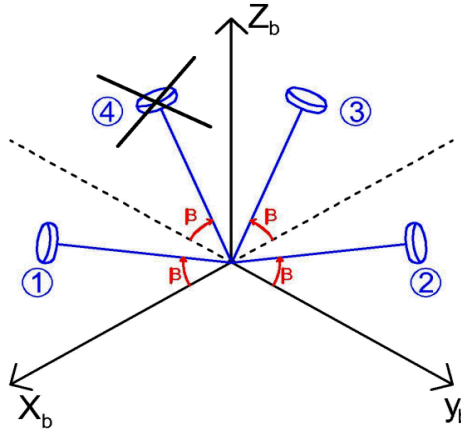### 5.3.1.1 Reaction Wheel-1 Failure
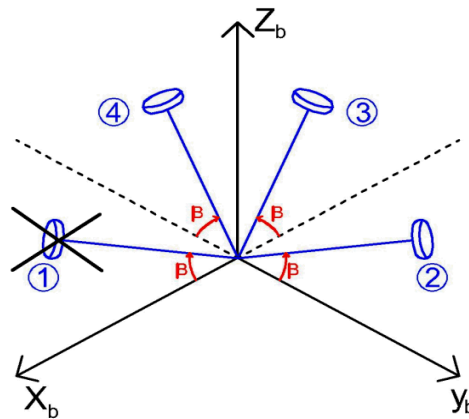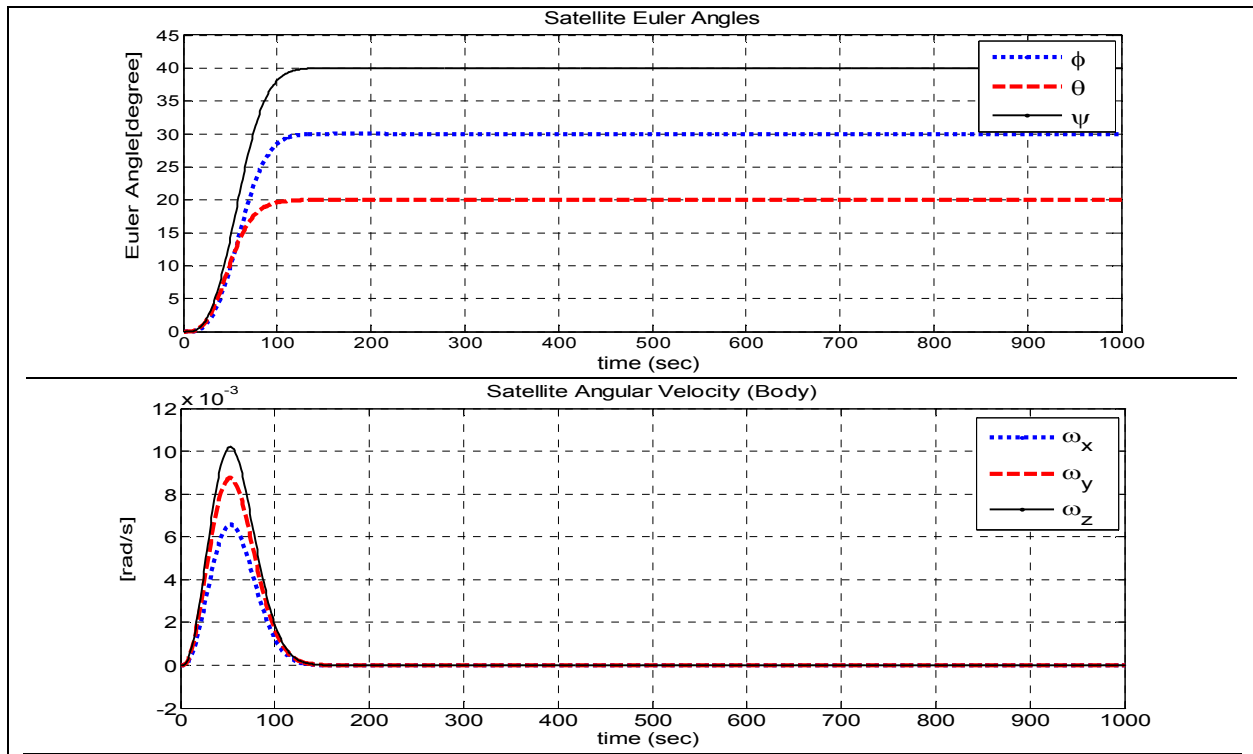
Figure 5.49 – System response of Integrator Backstepping for pyramid configuration when wheel-1 disabled

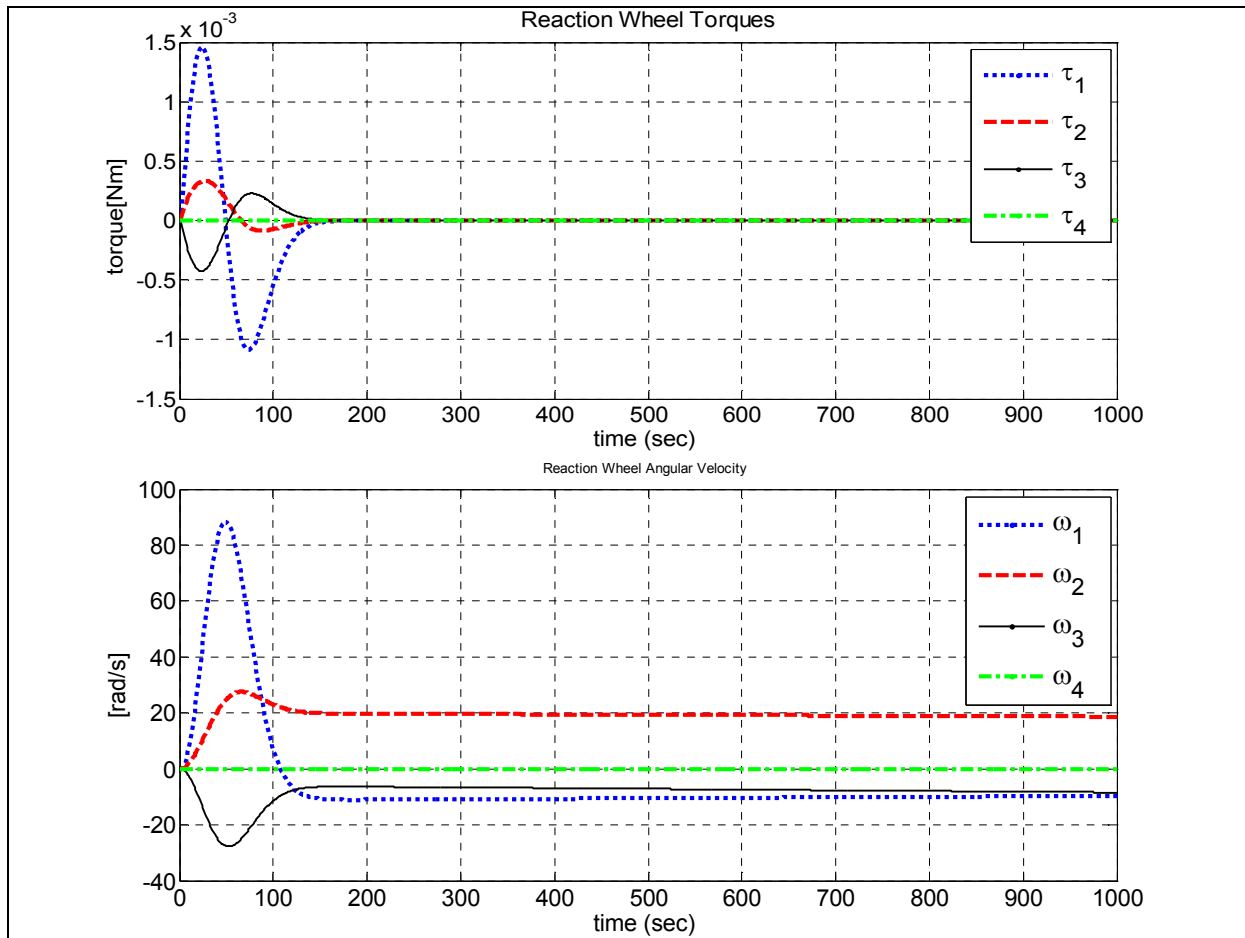The system reaches to desired Euler angles in 160 seconds. The settling time for the satellite angular velocity is 165 seconds. The settling times are very close to the 4-wheel (without actuator loss) case.
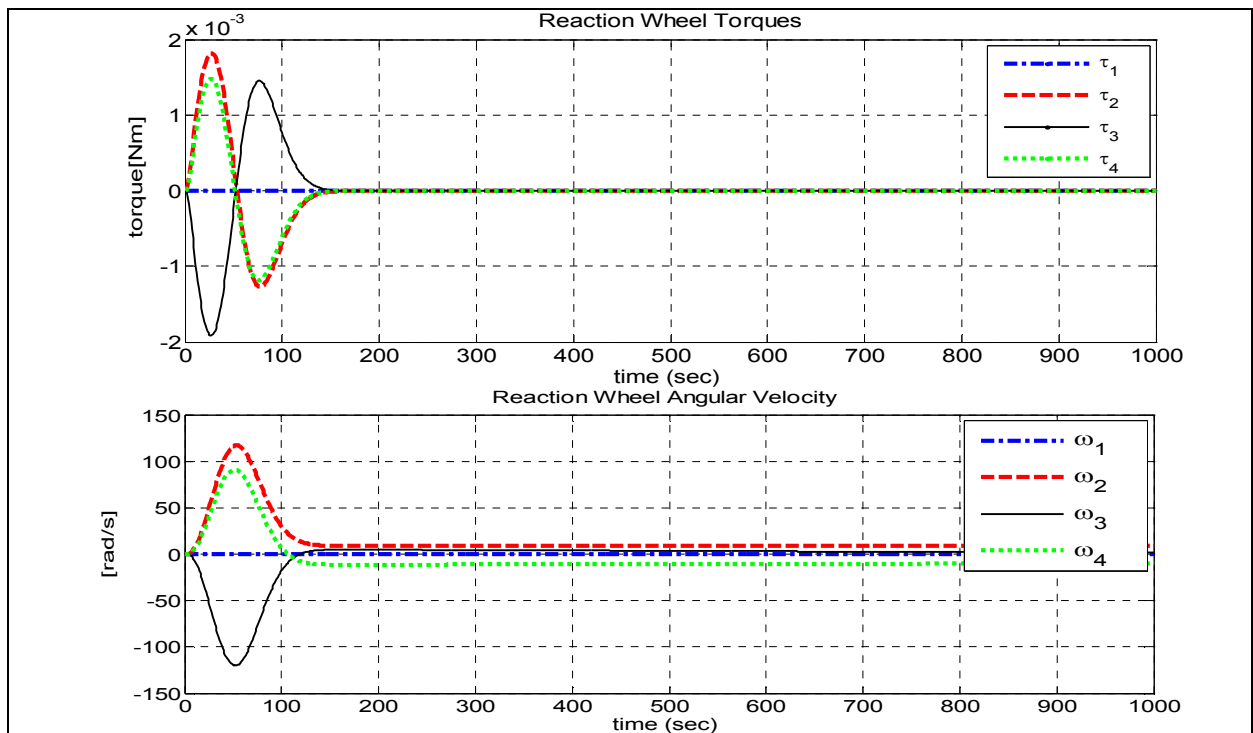
Figure 5.50 – Reaction wheel torques and angular velocities of Integrator Backstepping for pyramid configuration when wheel-1 disabled

Reaction wheel torques reaches to zero after 155 seconds. Maximum reaction wheel velocity is 119 rad/s. The power consumption significantly increases with one actuator loss, which is 0.0182 W. While the settling times are very close to Sliding Mode pyramid wheel-1 loss case, power consumption is much lower with Integrator Backstepping controller.

5.3.1.2 Reaction Wheel-2 Failure
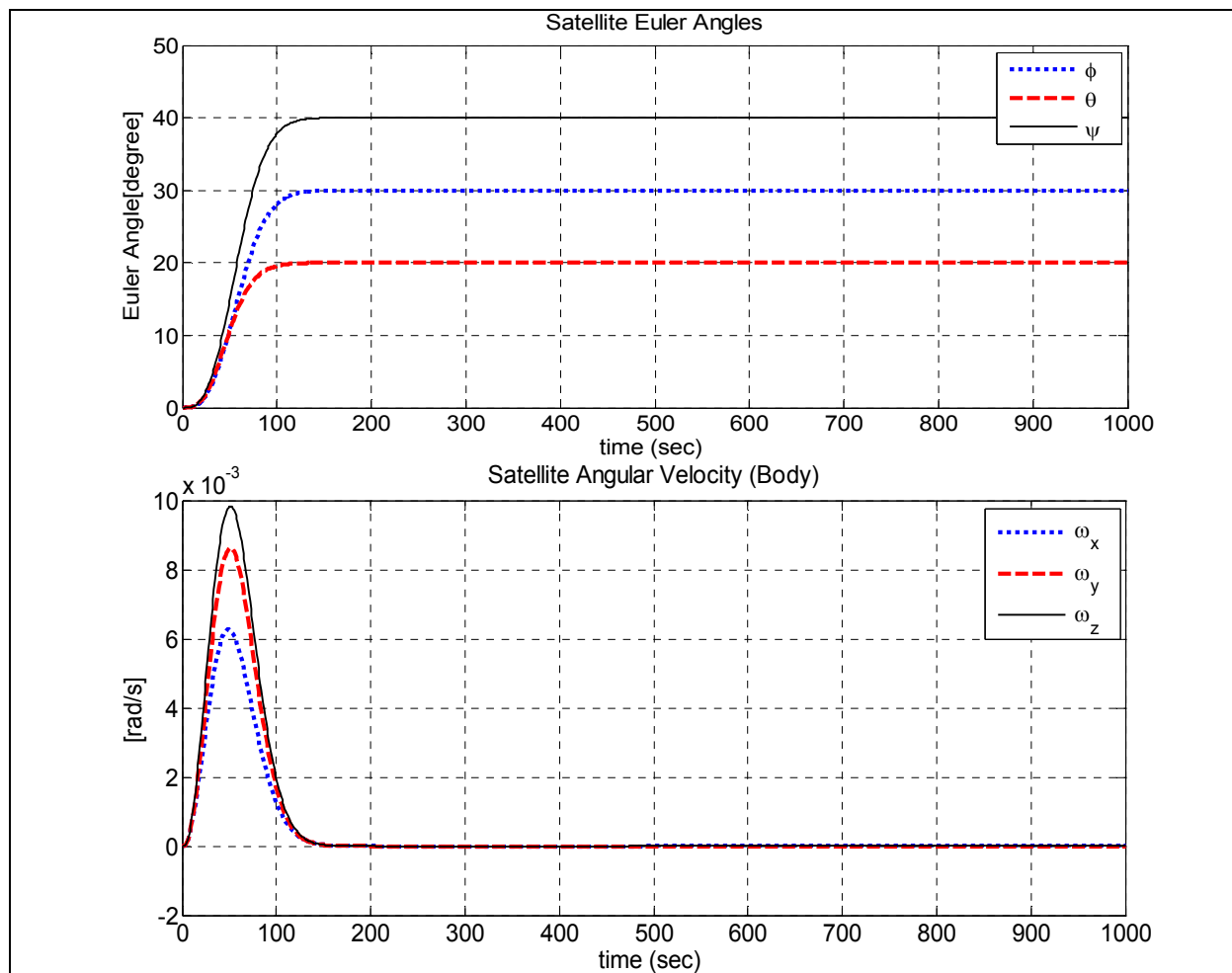
Figure 5.51 – System response of Integrator Backstepping for pyramid configuration when wheel-2 disabled

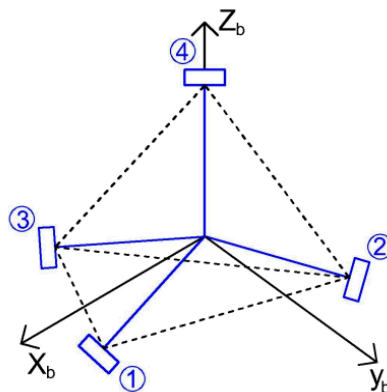The system reaches to desired Euler angles in 164 seconds. The settling time for the satellite angular velocity is 166 seconds. The settling times are very close to the wheel-1 failure case.

Figure 5.52 – Reaction wheel torques and angular velocities of Integrator Backstepping for pyramid configuration when wheel-2 disabled

Reaction wheel torques reaches to zero after 160 seconds. Maximum reaction wheel velocity is 114 rad/s. The total power consumption is 0.0071 W, which is much lower than wheel-1 failure case.

5.3.1.3 Reaction Wheel-3 Failure

Figure 5.53 – System response of Integrator Backstepping for pyramid configuration when wheel-3 disabled

The system reaches to desired Euler angles in 167 seconds. The settling time for the satellite angular velocity is 172 seconds.
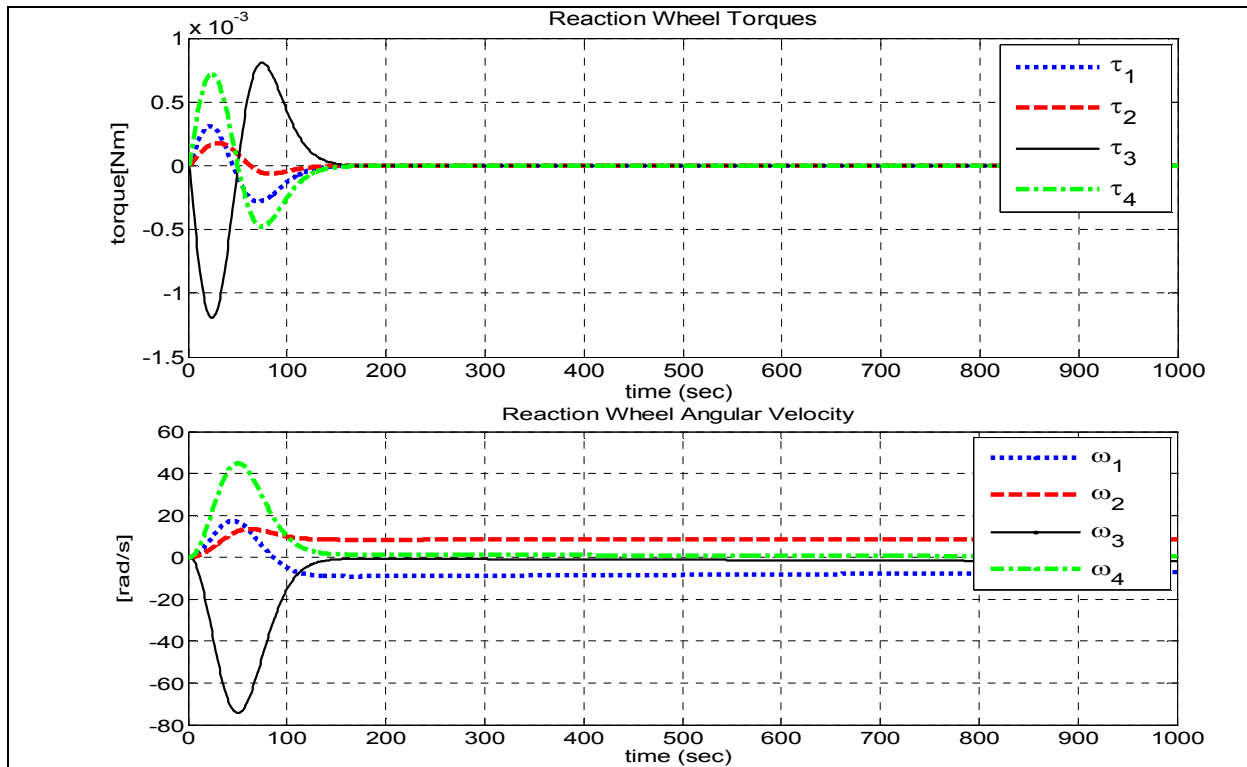

Figure 5.54 – Reaction wheel torques and angular velocities of Integrator Backstepping for pyramid configuration when wheel-3 disabled

Reaction wheel torques reaches to zero after 160 seconds. Maximum reaction wheel velocity is 117 rad/s. The total power consumption is 0.0075 W.
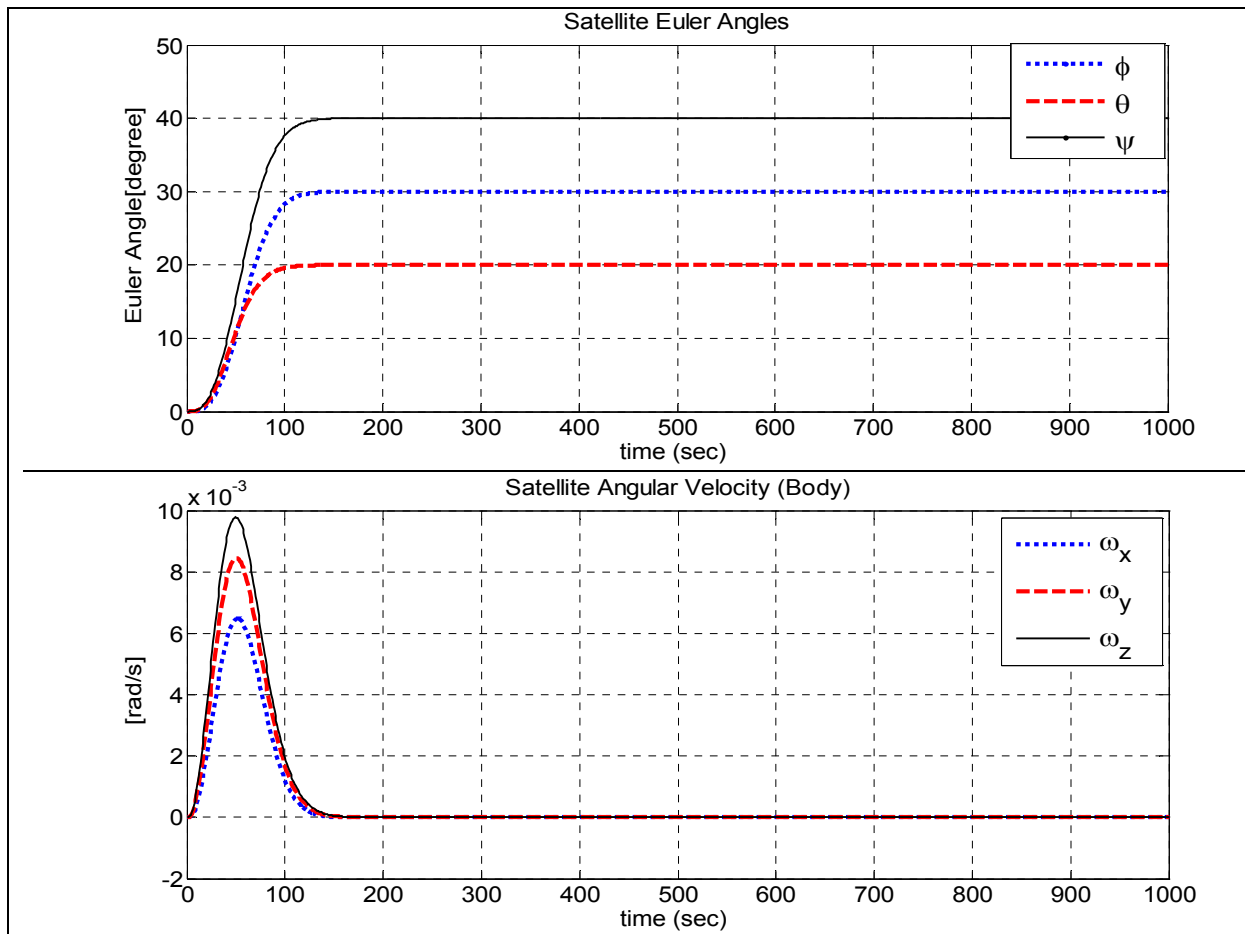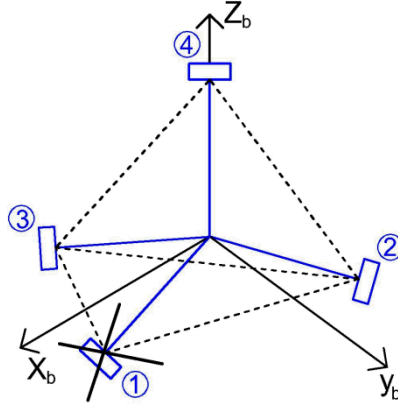
5.3.1.4 Reaction Wheel-4 Failure

Figure 5.55 – System response of Integrator Backstepping for pyramid configuration when wheel-4 disabled

The system reaches to desired Euler angles in 165 seconds. The settling time for the satellite angular velocity is 167 seconds.
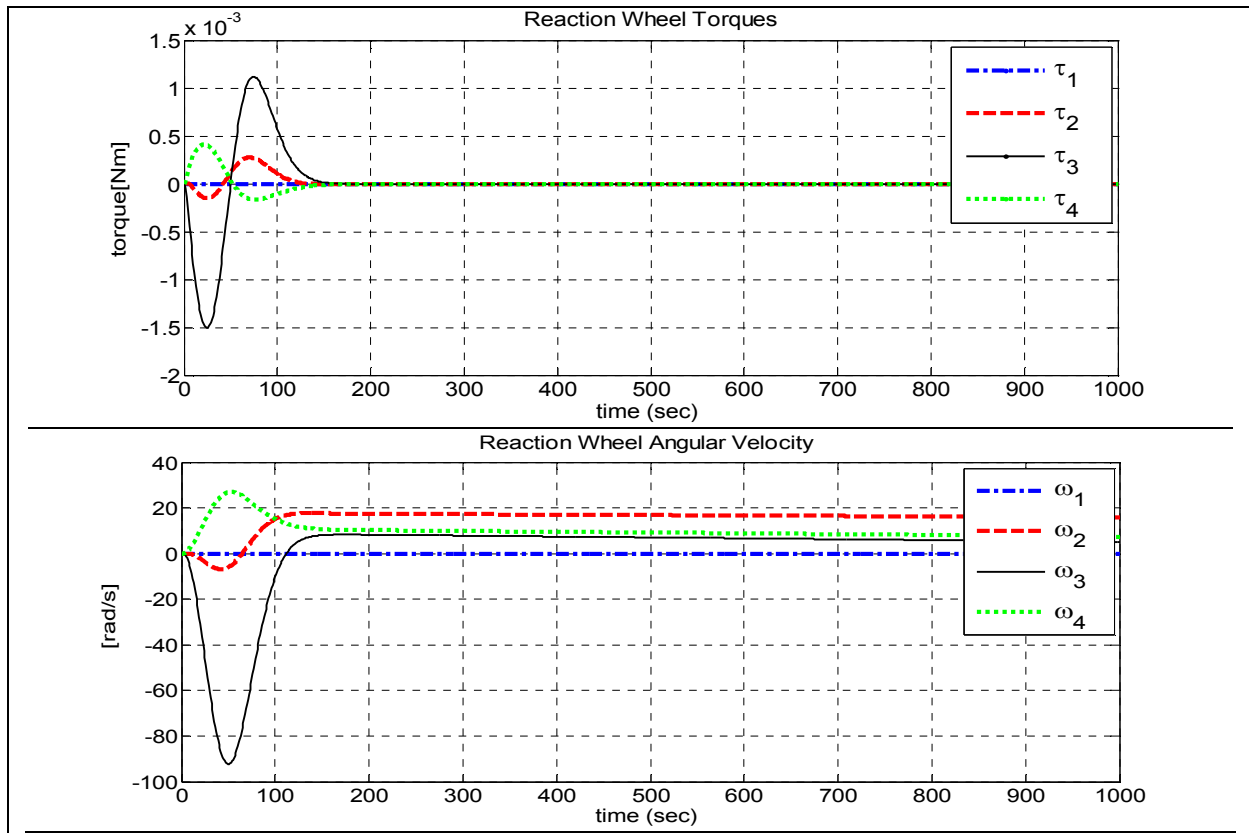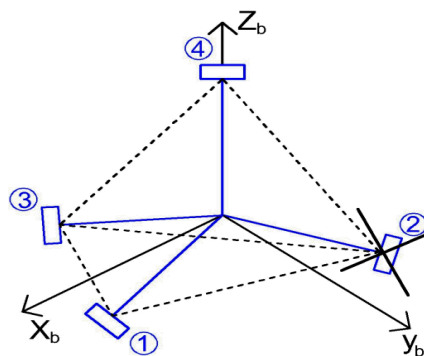

Figure 5.56 – Reaction wheel torques and angular velocities of Integrator Backstepping for pyramid configuration when wheel-4 disabled

Reaction wheel torques reaches to zero after 167 seconds. Maximum reaction wheel velocity is 88 rad/s. The total power consumption is 0.0046 W, which is lower that other wheel failure cases.

5.3.2 Tetrahedron Configuration
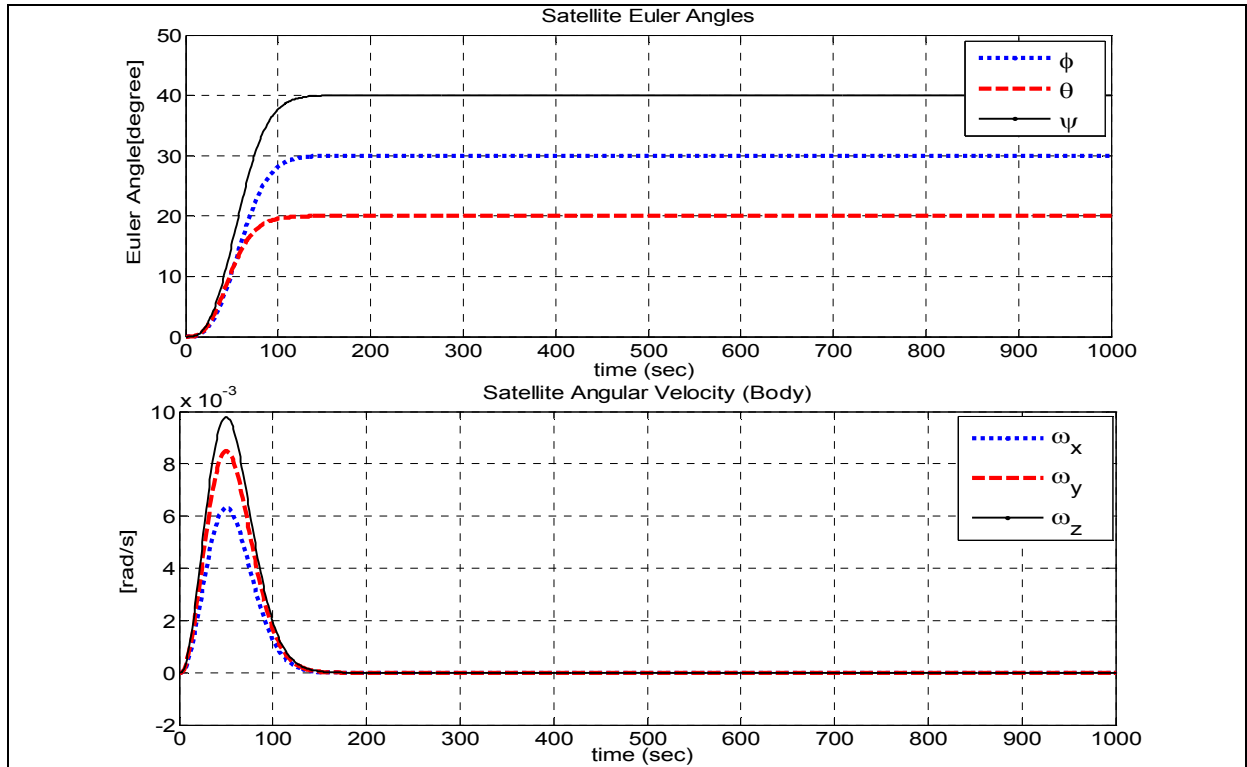
Figure 5.57 – System response of Integrator Backstepping for tetrahedron configuration

The system reaches to desired Euler angles in 166 seconds. The settling time for the satellite angular velocity is 170 seconds. These settling times are close to LQR and higher than Sliding Mode tetrahedron configurations.

Figure 5.58 – Reaction wheel torques and angular velocities of Integrator Backstepping for tetrahedron configuration

Reaction wheel torques reaches to zero after 160 seconds. Maximum reaction wheel velocity is 74 rad/s. Power consumption is higher than LQR and lower than Sliding Mode tetrahedron configuration, which is 0.0040 W.
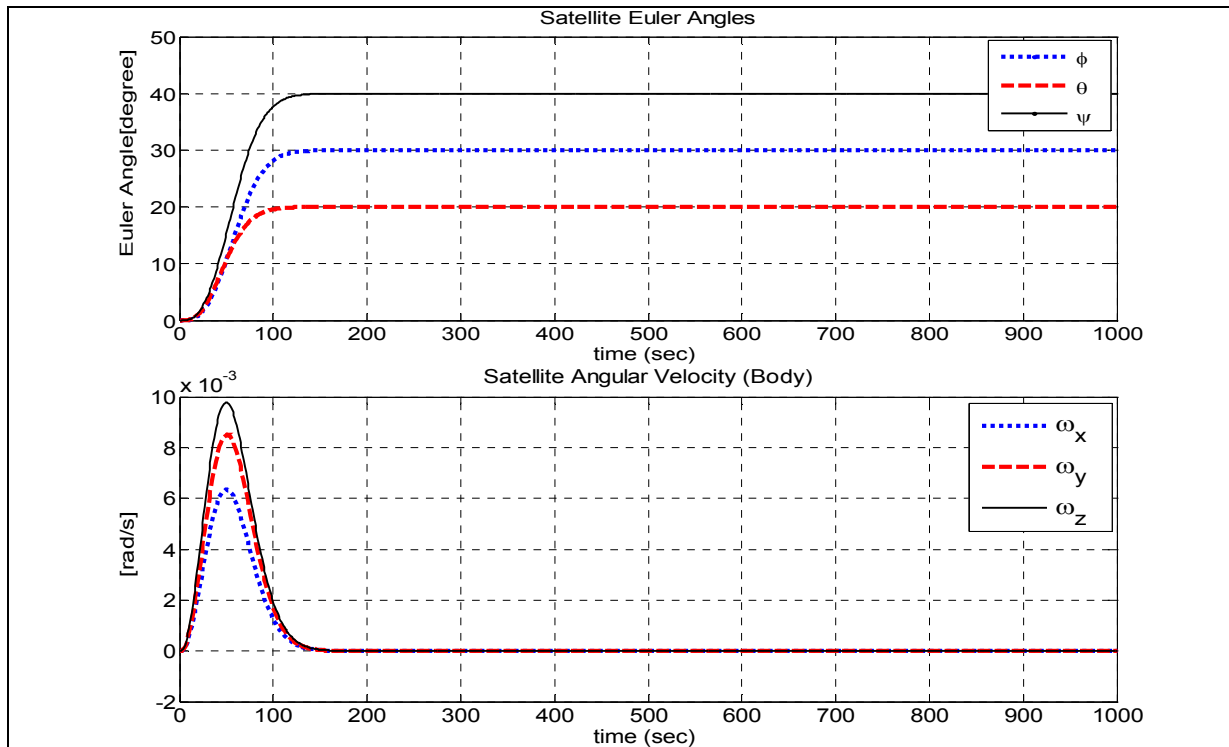
5.3.2.1 Reaction Wheel-1 Failure

Figure 5.59 – System response of Integrator Backstepping for tetrahedron configuration when wheel-1 disabled

The system reaches to desired Euler angles in 166 seconds. The settling time for the satellite angular velocity is 170 seconds. The settling times are almost the same with 4-wheels (without failure) case.
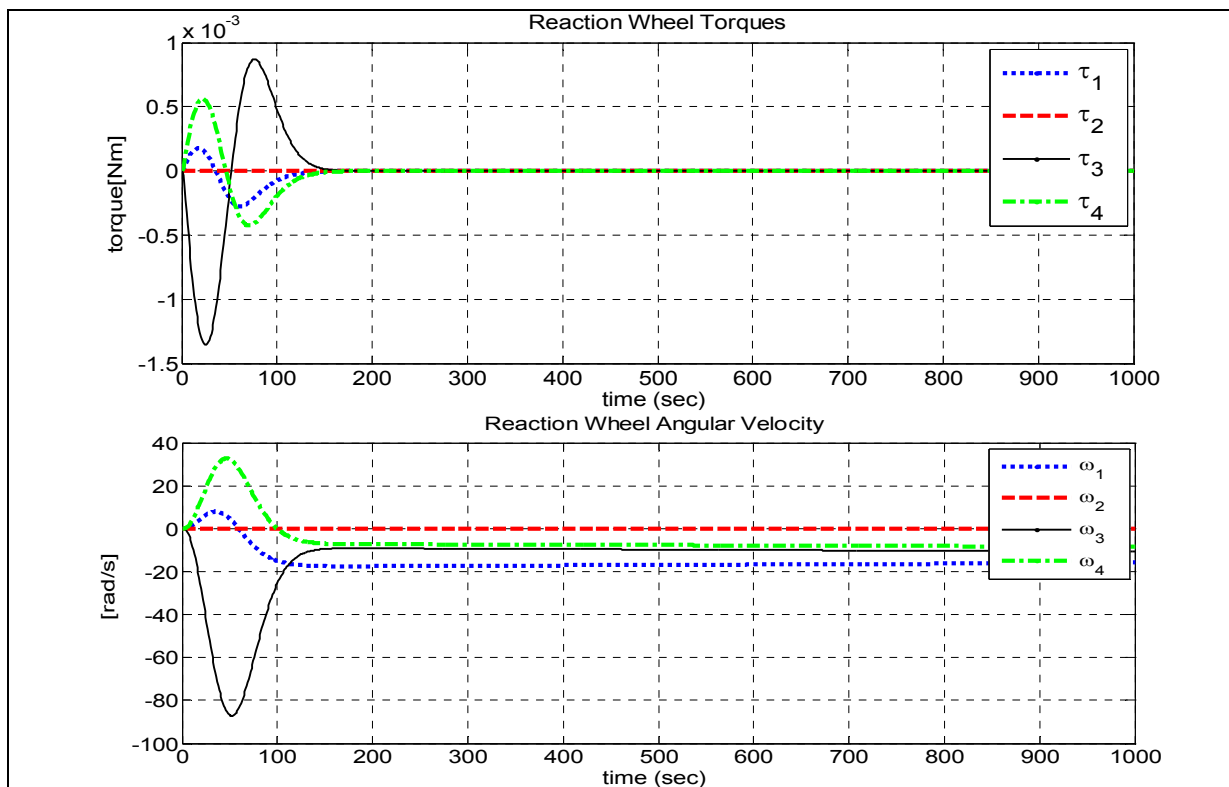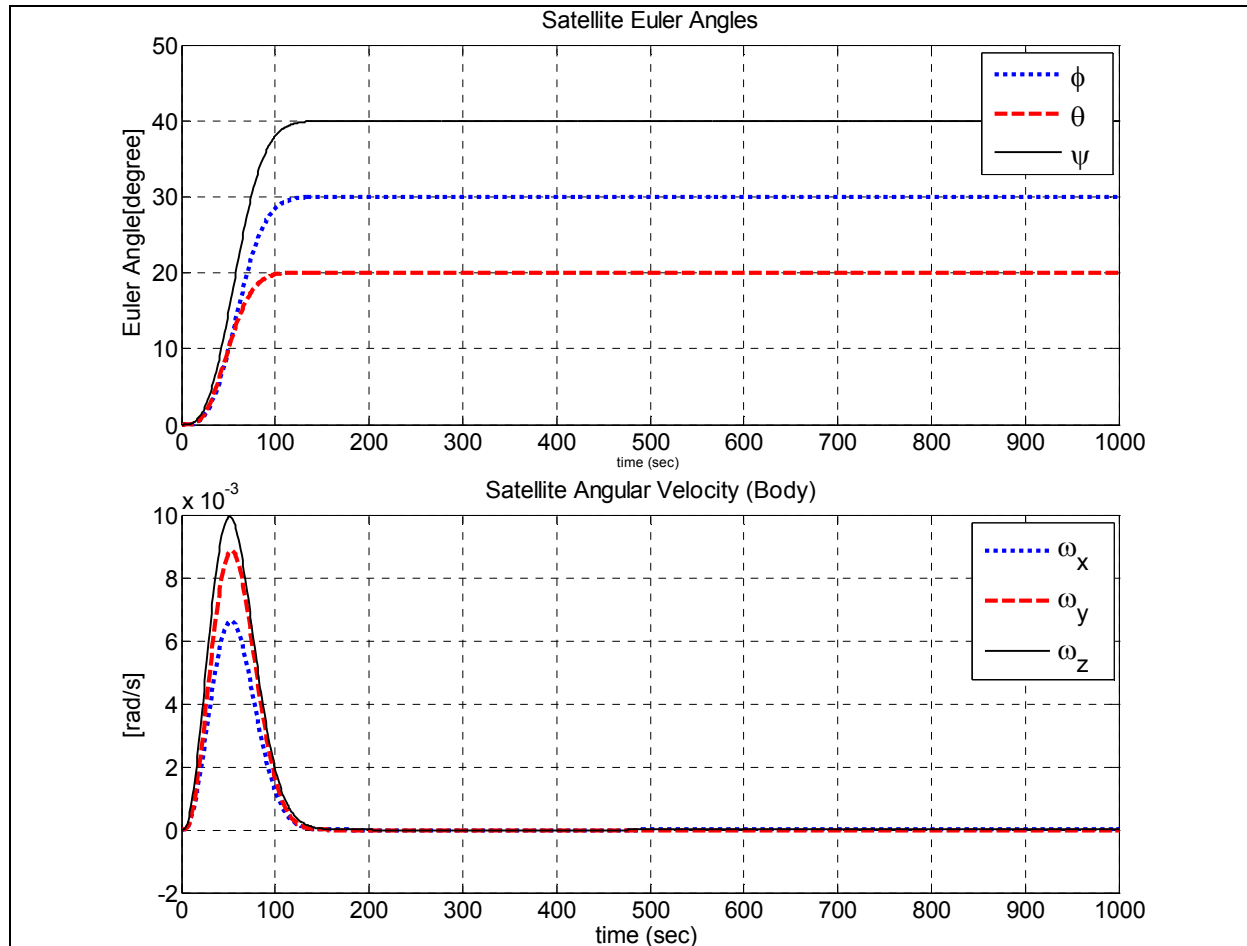

Figure 5.60 – Reaction wheel torques and angular velocities of Integrator Backstepping for tetrahedron configuration when wheel-1 disabled

Reaction wheel torques reaches to zero after 160 seconds. Maximum reaction wheel velocity is 92 rad/s. Power consumption slightly increases with the loss of one actuator, which becomes 0.0048 W. Therefore, tetrahedron configuration with the employment of Integrator Backstepping is more robust for the loss of one actuator compared to other controllers and configurations.
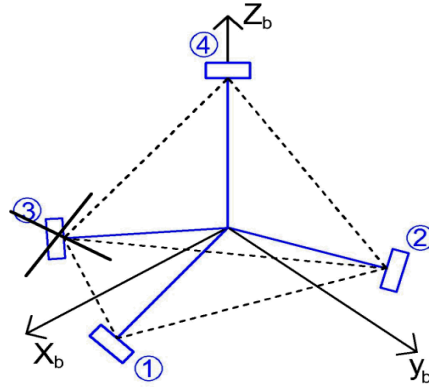
5.3.2.2 Reaction Wheel-2 Failure

Figure 5.61 – System response of Integrator Backstepping for tetrahedron configuration when wheel-2 disabled

The system reaches to desired Euler angles in 165 seconds. The settling time for the satellite angular velocity is 169 seconds.
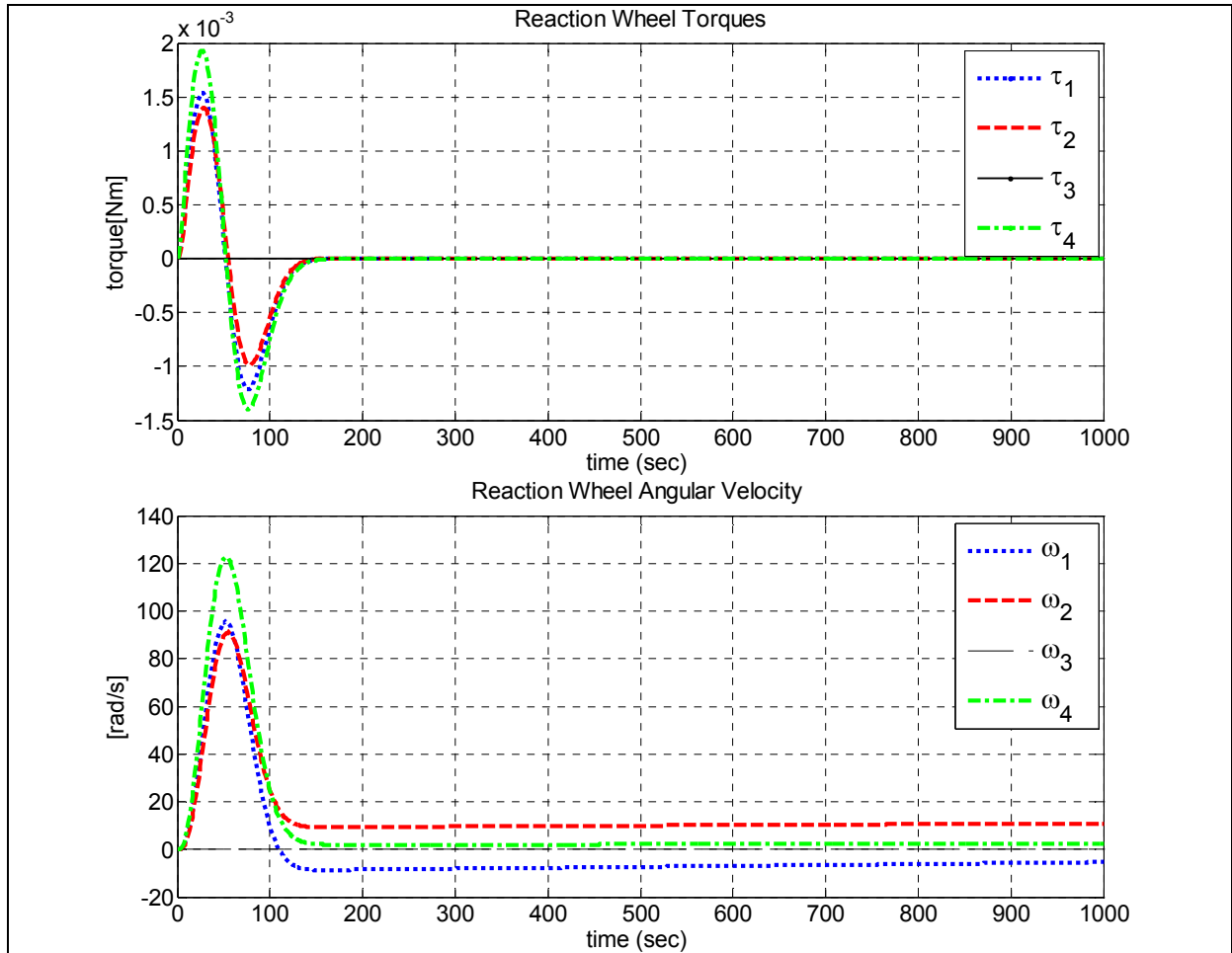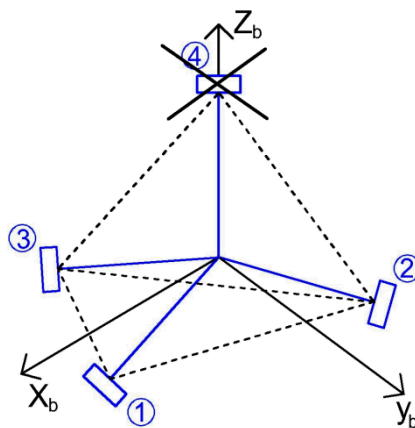

Figure 5.62 – Reaction wheel torques and angular velocities of Integrator Backstepping for tetrahedron configuration when wheel-2 disabled

Reaction wheel torques reaches to zero after 160 seconds. Maximum reaction wheel velocity is 87 rad/s. Total power consumption is 0.0045 W.

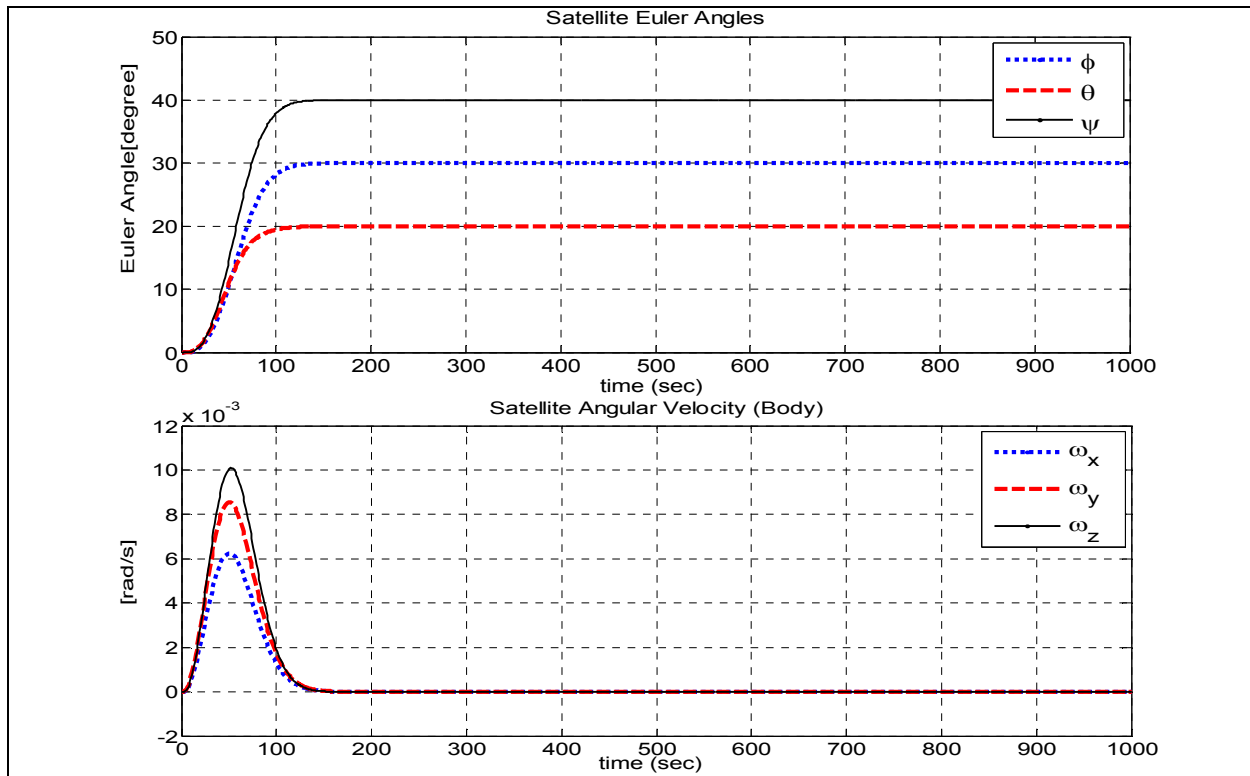### 5.3.2.3 Reaction Wheel-3 Failure

Figure 5.63 – System response of Integrator Backstepping for tetrahedron configuration when wheel-3 disabled

The system reaches to desired Euler angles in 156 seconds. The settling time for the satellite angular velocity is 164 seconds.
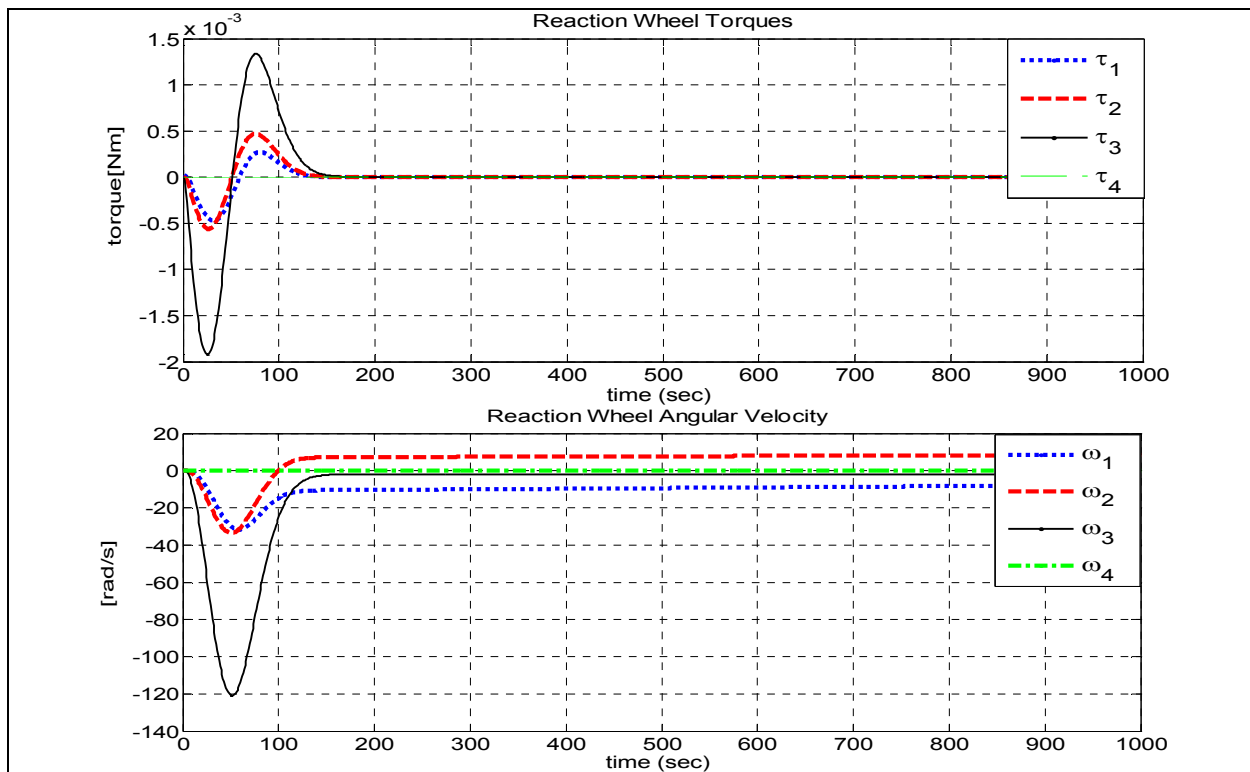
Figure 5.64 – Reaction wheel torques and angular velocities of Integrator Backstepping for tetrahedron configuration when wheel-3 disabled

Reaction wheel torques reaches to zero after 155 seconds. Maximum reaction wheel velocity is 122 rad/s. Total power consumption is 0.0162 W, which is much higher than other wheel failure cases.

5.3.2.4 Reaction Wheel-4 Failure

Figure 5.65 – System response of Integrator Backstepping for tetrahedron configuration when wheel-4 disabled

The system reaches to desired Euler angles in 160 seconds. The settling time for the satellite angular velocity is 166 seconds.

Figure 5.66 – Reaction wheel torques and angular velocities of Integrator Backstepping for tetrahedron configuration when wheel-4 disabled

Reaction wheel torques reaches to zero after 158 seconds. Maximum reaction wheel velocity is 120 rad/s. Total power consumption is 0.0084 W.

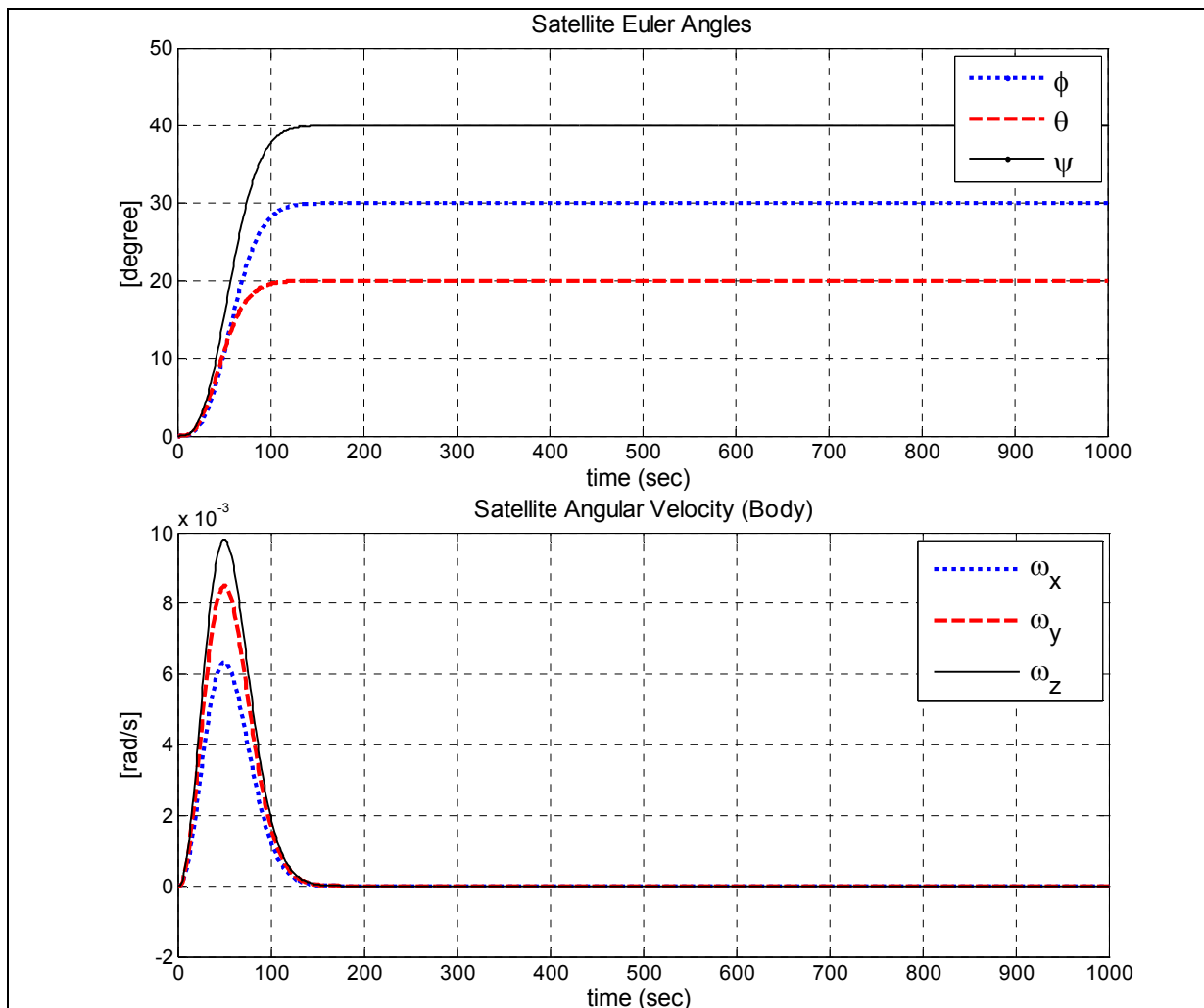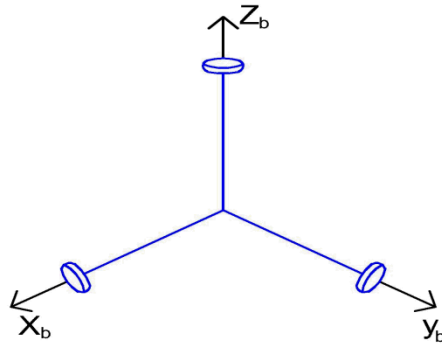### 5.3.3 Standard 3-wheel Configuration

Figure 5.67 – System response of Integrator Backstepping for 3-wheel configuration

The system reaches to desired Euler angles in 165 seconds. The settling time for the satellite angular velocity is 170 seconds. The settling times are same as pyramid and tetrahedron configurations.
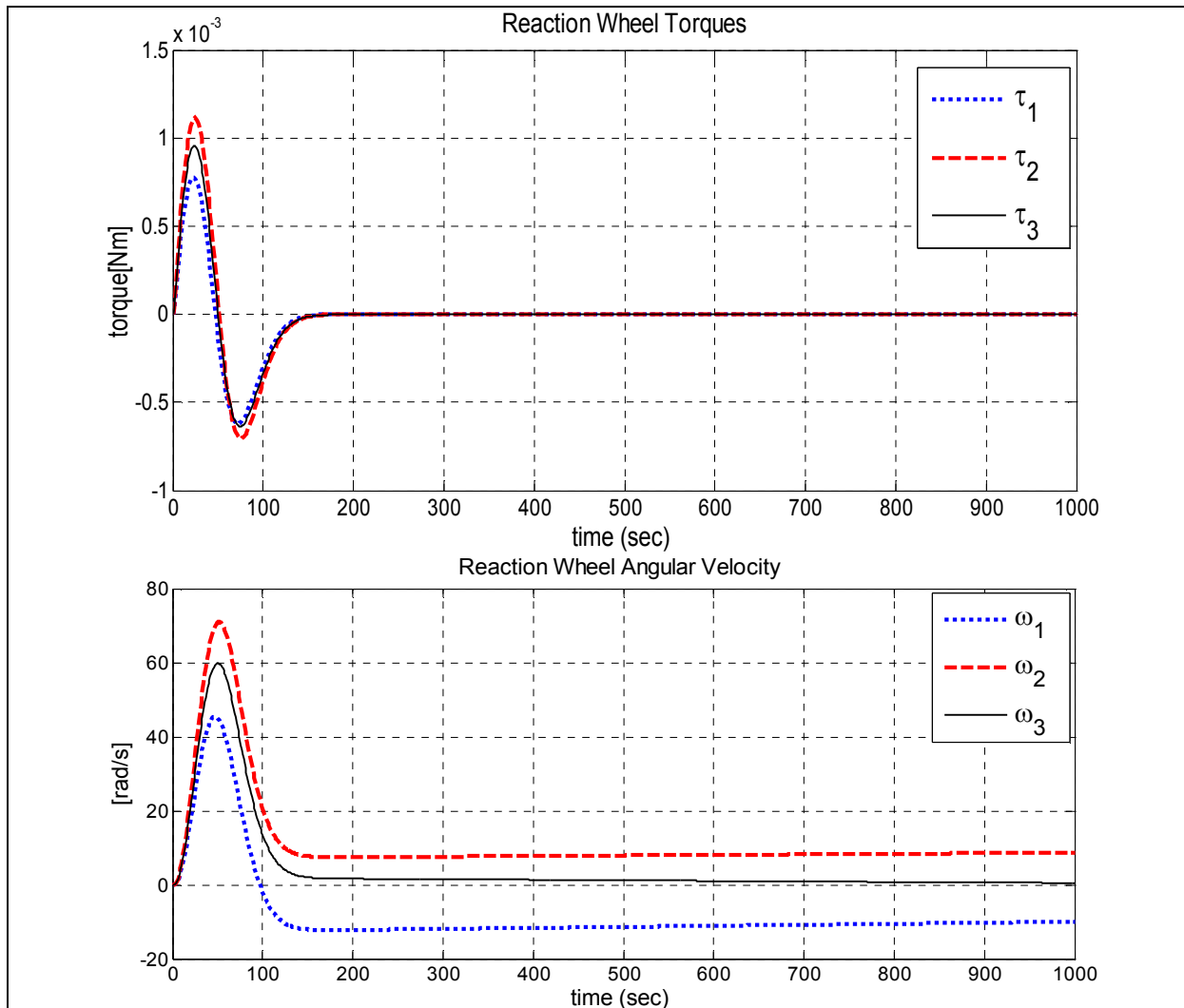

Figure 5.68 – Reaction wheel torques and angular velocities of Integrator Backstepping for 3-wheel configuration

Maximum reaction wheel velocity is 71 rad/s. Power consumption is higher than both pyramid and tetrahedron configurations, which is 0.0054 W. It can be concluded that, Integrator Backstepping provides the same system performances for different reaction wheel configurations while the power consumption changes respectively.

Moreover, it can be observed that for all of the three controllers, classical 3-wheel configuration consumes more power compared to pyramid and tetrahedron configurations without actuator loss.

5.4 Reaction Wheel Distribution Matrix Analysis

To find the optimum reaction wheel distribution matrix, simulations can be employed by changing the angles inside the matrix and comparing the results. For comparison purposes, the following tables are derived keeping the controller the same (Integrator Backstepping) while changing the structure angles. Integrator Backstepping is an ideal controller for these comparison purposes since this controller keeps the settling times almost the same, even in the case of actuator loss, while changing power consumptions for different reaction wheel distribution matrices. In this sub-chapter, the cross-over frequency is increased to $\omega_n = 0.1$ to show its effect on power consumption and settling time.

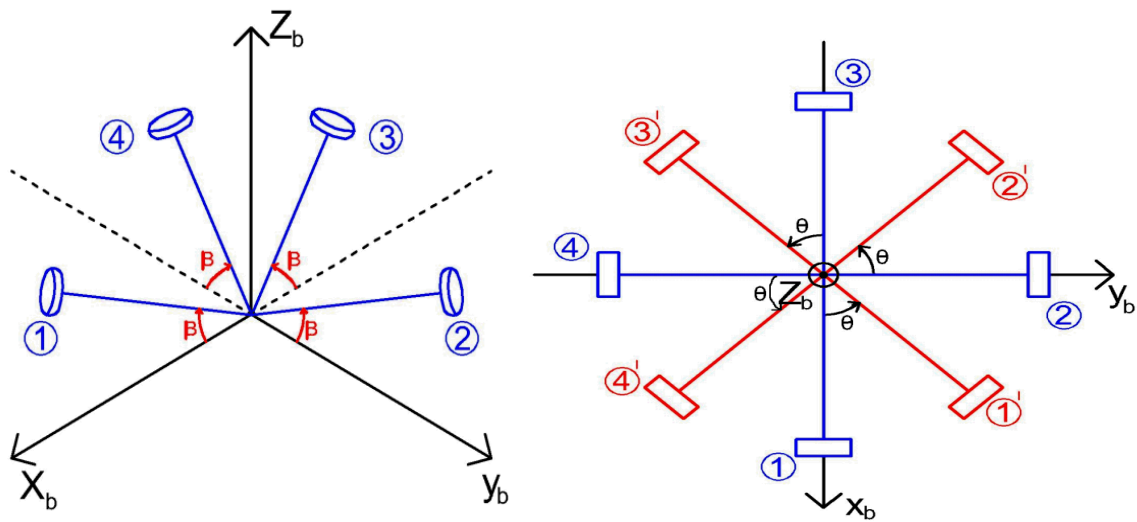### 5.4.1 Pyramid Reaction Wheel Configuration

Figure 5.69 – Pyramid reaction wheel configuration

In chapter 3.4.2, the distribution matrix for pyramid configuration is derived as follows:

$$L = \begin{bmatrix} cos\beta cos\theta & -cos\beta sin\theta & -cos\beta cos\theta & cos\beta sin\theta \\ cos\beta sin\theta & cos\beta cos\theta & -cos\beta sin\theta & -cos\beta cos\theta \\ sin\beta & sin\beta & sin\beta & sin\beta \end{bmatrix} \tag{5.7}$$

The following table is derived employing pyramid configuration for different Ө angles while keeping β=45 degrees.

Θ (deg)	Power (Watt)	Settling Time (s)
0	0.020347	104
10	0.020309	104
20	0.020265	104
30	0.020234	104
40	0.020276	104
45	0.020278	104
50	0.020277	104
60	0.020285	104
70	0.020316	104
80	0.020385	104
90	0.020347	104

Table 5.5 – Comparison of power consumptions for different Θ angles of pyramid configuration while β=45 deg.

From the Table 5.5, it is clear that changing the Θ angle does not have a significant effect on the overall power consumption. The following table is derived employing pyramid configuration for different β angles while keeping Θ =45 deg.

β (deg)	Power (Watt)	Settling Time (s)
10	0.0743	104
20	0.0262	104
30	0.0188	104
40	0.0187	104
45	0.0203	104
50	0.0231	104
60	0.0352	104
70	0.0716	104
80	0.2707	104

Table 5.6 – Comparison of power consumptions for different β angles of pyramid configuration while Θ=45 deg

From the Table 5.6, it is observed that minimum power consumption for β angle, while Θ=45 deg, is somewhere between 30-40 deg. In chapter 3.4.1, it is shown that for $\theta = 45^o$ and $\beta = 35.264^o$, the following homogenous distribution matrix can be found:

$$L = \begin{bmatrix} \sqrt{3}/3 & -\sqrt{3}/3 & -\sqrt{3}/3 & \sqrt{3}/3 \\ \sqrt{3}/3 & \sqrt{3}/3 & -\sqrt{3}/3 & -\sqrt{3}/3 \\ \sqrt{3}/3 & \sqrt{3}/3 & \sqrt{3}/3 & \sqrt{3}/3 \end{bmatrix} \tag{5.8}$$

The power consumption for this homogenous distribution matrix is 0.0182 W, which is the lowest power value compared to the values in the graphs above. It can be concluded that, for the pyramid wheel configuration the optimum power consumption can be derived with a homogenous reaction wheel distribution matrix.

The following table is derived employing pyramid configuration for different Ө angles when wheel-1 disabled:

Ө (deg)	Power (Watt)	Settling Time (s)
0	0.0497	102
10	0.0593	100
20	0.0687	97
30	0.0769	93
40	0.0831	88
50	0.0868	83
60	0.0876	86
70	0.0855	92
80	0.0795	96
90	0.0690	104

Table 5.7 – Comparison of power consumptions for the pyramid configuration when wheel-1 disabled

From Table 5.7, it can be concluded that for the actuator failure case it is more adventageous to insert the pyramid configuration along the body axis-planes, e.g. $\Theta = 0$ in Figure 5.69. Another point is, for pyramid reaction wheel configuration the increase in the power consumption with an actuator failure is much higher compared to tetrahedron configuration.

Moreover, to show the effect of cross-over frequency ω_n, its value is increased from $\omega_n = 0.02$ to $\omega_n = 0.1$ in this chapter. For the case of $\theta = 45^o$ and $\beta = 45^o$, it is found that for $\omega_n = 0.02$ in chapter 5.3.1 the power consumption is 0.0045 W and settling time is 170 seconds. For $\omega_n = 0.1$, however, the power consumption is 0.0203 W and settling time is 104 seconds. It is clear that, increasing the cross-over frequency ω_n increases the power consumption while decreasing the settling time.

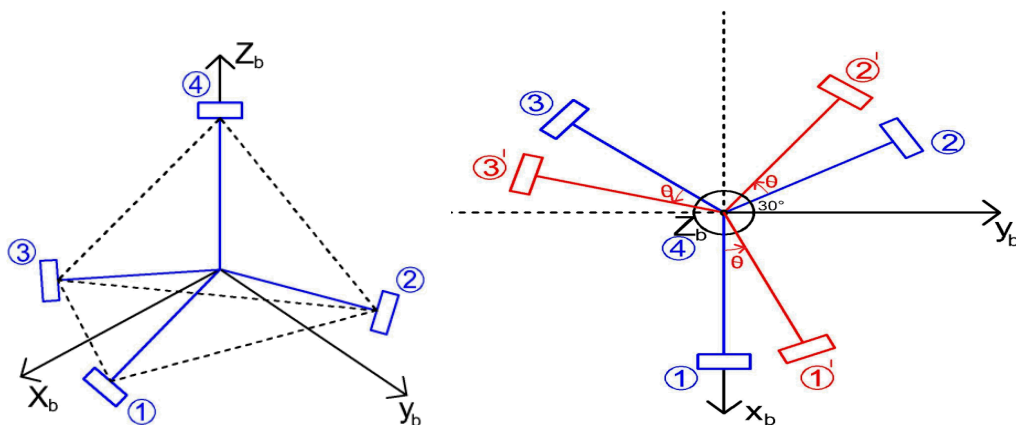### 5.4.2 Tetrahedron Reaction Wheel Configuration

Figure 5.70 – Tetrahedron reaction wheel configuration

In chapter 3.4.3, the distribution matrix for tetrahedron configuration, when wheel-4 is on z_B axis, is derived as follows:

$$L = \begin{bmatrix} \cos(19.47)\cos\theta & -\cos(19.47)\cos(60-\theta) & -\cos(19.47)\cos(60+\theta) & 0 \\ \cos(19.47)\sin\theta & \cos(19.47)\cos(30+\theta) & -\cos(19.47)\cos(30-\theta) & 0 \\ -\sin(19.47) & -\sin(19.47) & -\sin(19.47) & 1 \end{bmatrix} \qquad (5.9)$$

The following table is derived employing tetrahedron configuration for different Ө angles:

Ө (deg)	Power (Watt)	Settling Time (s)
0	0.018217	104
10	0.018258	104
20	0.018269	104
30	0.018253	104
40	0.018231	104
50	0.018208	104
60	0.018186	104
70	0.018166	104
80	0.018153	104
90	0.018148	104
100	0.018228	104
110	0.018230	104
120	0.018217	104

Table 5.8 – Comparison of power consumptions for the tetrahedron configuration with wheel-4 is on z_B axis

From the Table 5.8, it is clear that changing the Ө angle does not have a significant effect on the overall power consumption. In Appendix B, it is shown that the following homogenous distribution matrix for tetrahedron configuration can be found :

$$L = \begin{bmatrix} \sqrt{3}/3 & -\sqrt{3}/3 & -\sqrt{3}/3 & \sqrt{3}/3 \\ \sqrt{3}/3 & -\sqrt{3}/3 & \sqrt{3}/3 & -\sqrt{3}/3 \\ \sqrt{3}/3 & \sqrt{3}/3 & -\sqrt{3}/3 & -\sqrt{3}/3 \end{bmatrix} \qquad (5.10)$$

The power consumption for this distribution matrix is 0.018196 W, which is in the range of the the power consumption values in Table 5.8. It can be concluded that, the attitude of the tetrahedron structure of reaction wheels relative to the body frame does not have a significant effect on overall power consumption. However, for the case of loss of a reaction wheel (wheel-1), position of tetrahedron structure has a significant effect as can be seen in the following table:

Θ (deg)	Power (Watt)	Settling Time (s)
0	0.0218	105
10	0.0254	106
20	0.0297	106
30	0.0336	106
40	0.0367	106
50	0.0385	106
60	0.0388	107
70	0.0374	106
80	0.0347	106
90	0.0309	106
100	0.0267	106
110	0.0228	105
120	0.0200	105

Table 5.9 – Comparison of power consumptions for the tetrahedron configuration with wheel-4 is on z_B axis and wheel-1 disabled

From Table 5.9, it can be concluded that having zeros in the distribution matrix, which can be achieved when one or two of the reaction wheels does not have torque contributions on some body axes (e.g. $\Theta = 0$ in Figure 5.70), provides the optimum power consumptions in the case of loss of a reaction wheel. For the homogenous distribution matrix in (5.10), the power consumption in the case of an actuator failure is 0.0783 W, which is much higher than the values in Table 5.8. This also proves that it is better not to have a homogenous distribution matrix for the case of loss of an actuator.

Chapter 6

Conclusion and Recommendations

6.1 – Conclusion

In this thesis, one linear controller and two non-linear control algorithms are analyzed for the attitude control of a satellite. Three different reaction wheel configurations, namely pyramid, tetrahedron and 3-wheel configurations, are analyzed and compared in terms of power consumption, settling times and actuator failure robustness.

In the simulations a second order reference model is employed, which provides a rather smooth trajectory which consumes less power. It is observed that, increasing the cross-over frequency ω_n results in lower settling times but higher power consumptions. Therefore, this term together with the controller gain matrices need to be adjusted to satisfy a mission's system performance requirements.

For LQR quaternion-feedback controller it is demonstrated that by adjusting the controller weight matrices or cross-over frequency in reference model, like for the other control algorithms, the system performance can be modified. However, the problem with the LQR controller, which is essentially a quaternion based PD controller, is that for the actuator loss cases big oscillations in Euler angles are observed. Moreover, with an actuator loss, settling times also gets very longer. Sliding Mode controller simulations resulted in the shortest settling times and highest power consumptions. For the pyramid configuration of Sliding Mode, loss of an actuator resulted in longer settling times. Among these controllers, Integrator Backstepping is the best option in terms of actuator failure robustness. Integrator Backstepping controller keeps the settling times almost the same for different reaction wheel distribution matrices. Moreover, for the case of an actuator loss the settling times are very close to 4-wheel case while the increase in power consumption is relatively small.

Pyramid and tetrahedron configurations employ four reaction wheels, which provides an actuator redundancy since three actuators are required for the three-dimensional attitude control of a satellite. In all three of the control algorithms, simulations show that the settling times without an actuator failure for both configurations are very close, while the power consumptions are lower for tetrahedron configuration. Moreover, in the case of an actuator failure, the percentage of increase in the power consumption is much lower for the tetrahedron configuration compared to pyramid configuration. Although classical 3-wheel configuration does not have the highest wheel angular velocities, simulations show that it consumes more power compared to 4-wheel configurations. The reason can be observed from the graphs, which show that during the attitude maneuver for the standard 3-wheel configuration all three wheels are highly active in creating torque. However, for the 4-wheel

configurations, one or two of the wheels are doing most of the work while the other wheels do not contribute so much to create torque. Finally, it can be pointed out that employing tetrahedron reaction wheel configuration with Integrator Backstepping controller provides power efficiency and actuator failure robustness in terms of system performances.

6.2 – Recommendations for Future Work

Although Integrator Backstepping proved to be a very efficient controller in terms of system performances and power consumption, implementation of this controller requires the computation of control torque for each integrator level, which may end up in a computational burden. Therefore, in the case of a computational burden, some simpler control algorithms with satisfactory system performances needs to be employed or some new control strategies can be designed and tested.

Attitude control of underactuated satellites, which have less than three attitude control actuators, is another important issue. In the last few years some papers have been published regarding this control problem. In most of these articles, actuator failure possibility for the standard orthogonal 3-wheel configurations is investigated. For the 4-wheel configurations, regarding that it already is an overactuated system, there is not much investigations for the case of loss two of the wheels. Since the dynamical equations of the satellite are highly coupled, it is mentioned in the literature that an underactuated spacecraft cannot be asymptotically stabilized via continuous state feedback controllers. [15],[16],[17] Therefore, some discontinuous feedback control strategies need to be developed for the 4-wheel configurations in case of loss of two of the wheels.

Bibliography

[1] Q. Hu. *Robust adaptive sliding-mode fault-tolerant control with L_2-gain performance for flexible spacecraft using redundant reaction wheels*. Harbin Institute of Technology, 2009

[2] Johannes Schoonwinkel*. Attitude Determination and Control System of a Nanosatellite*. Master Thesis, University of Stellenbosch 2007

[3] Aaron John Dando. *Robust Adaptive Control of Rigid Spacecraft Attitude Maneuvers*. PhD Thesis, Queensland University of Technology, 2008

[4] B. Prabhakar Rao, G. Sunil Kumar*. Sliding Mode Controller Design For Spacecraft Attitude Stabilization*. International Journal of Advanced Engineering Sciences and Technologies, Vol No. 11, Issue No. 1, 183 – 189

[5] Soner Karataş. *LEO Satellites: Dynamic Modelling, Simulations and some Nonlinear Attitude Control Techniques*. Master's thesis, Middle East Technical University 2006

[6] R. Kristiansen*. Attitude Control Of a Microsatellite*. Master Thesis, Department of Engineering Cybernetics, NTNU, 2000

[7] Marcel J. Sidi. *Spacecraft Dynamics and Control*. Cambridge University Press, 1997

[8] Raymond Kristiansen, Per J. Nicklasson. *Satellite Attitude Control by Quaternion-Based Backstepping.* American Control Conference, Portland June 8-10, 2005

[9] Mihaela Raluca Stefanescu, Claudiu Lucian Prioroc. *Automatic Control Systems for ESMO Satellite Using LQR Control Strategy*. 1st IAA Conference on Dynamics and Control of Space Systems, 2012

[10] Katsuhiko Ogata. *Modern Control Engineering*. Prentice Hall, 1997

[11] F.L. Lewis. *Linear Quadratic Regulator (LQR) State Feedback Design*. University of Texas at Arlington, 1998.

[12] Peijun Yu, Keqiang Xia, Jiancheng Li. *A Design of Reconfigurable Satellite Control System with Reaction Wheels Based on Error Quaternion Model*. International Conference on Internet Computing and Information Services, 2011.

[13] Reşat Özgür Doruk*. Nonlinear Controller Designs For A Reaction Wheel Actuated Observatory Satellite.* PhD Thesis, Department of Electrical and Electronics Engineering, METU 2008

[14] San Luis Obispo. *Control And Sensor Development On A Four-Wheel Pyramidal Reaction Wheel Platform*. Master's thesis, California Polytechnic State University, 2008

[15] Ge Xinsheng, Zhang Qizhi, Chen Li-Qun. *Optimal Motion Planning For a Rigid Spacecraft With Two Momentum Wheels Using Quasi-Newton Method*. Acta Mechanica Solida Sinica, Vol. 19, No. 4, 2006

[16] Lei Jin, Shijie Xu. *Underactuated Spacecraft Angular Velocity Stabilization and Three-axis Attitude Stabilization Using Two Single Gimbal Control Moment Gyros*. The Chinese Society of Theoretical and Applied Mechanics and Springer-Verlag GmbH, 2009

[17] Hariharan Krishnan, N. Harris McClamroch, Mahmut Reyhanoglu. *Attitude Stabilization of a Rigid Spacecraft Using Two Momentum Wheel Actuators*. Journal of Guidance, Control and Dynamics, Vol.18 No. 2, 1995

[18] Morten Pedersen Topland*. Nonlinear Attitude Control of the Micro-Satellite ESEO*. Master thesis, Norwegian University of Science and Technology, 2004

[19] Geir Ytrehus. *Styring av mikrosatellitt med reaksjonshjul i tetraeder*. Master's thesis, Norwegian University of Science and Technology, 2003

 [20]   Stig Johanessen. *ESMO ADCS Redundancy Management*. Master's thesis, Narvik University College, 2006

[21]   Joel Burdick. *The Moore-Penrose Pseudo Inverse.* Introduction to Kinematics and Robotics lecture notes, California Institute of Technology

Appendix A

DC Motor Datasheet

FAULHABER

Brushless DC-Servomotors

5,2 mNm

For combination with
Gearheads:
20/1
Encoders:
IE2-1024, 5500, 5540
Drive Electronics:
Speed Controller, Motion Controller

Series 2036 ... B

		2036 U		012 B	024 B	036 B	048 B	
1	Nominal voltage	U_N		12	24	36	48	Volt
2	Terminal resistance, phase-phase	R		3,4	14,0	27,9	62,2	Ω
3	Output power [1]	$P_{2\ max.}$		20	19	18	18	W
4	Efficiency	$\eta_{\ max.}$		70	69	69	69	%
5	No-load speed	n_0		17 600	18 000	19 500	17 400	rpm
6	No-load current (with shaft ø 2,0 mm)	I_0		0,102	0,053	0,040	0,025	A
7	Stall torque	M_H		22	21	22	20	mNm
8	Friction torque, static	C_0		0,27	0,27	0,27	0,27	mNm
9	Friction torque, dynamic	C_v		$2,14 \cdot 10^{-5}$	$2,14 \cdot 10^{-5}$	$2,14 \cdot 10^{-5}$	$2,14 \cdot 10^{-5}$	mNm/rpm
10	Speed constant	k_n		1 506	773	557	374	rpm/V
11	Back-EMF constant	k_E		0,664	1,294	1,796	2,677	mV/rpm
12	Torque constant	k_M		6,34	12,36	17,15	25,56	mNm/A
13	Current constant	k_I		0,158	0,081	0,058	0,039	A/mNm
14	Slope of n-M curve	$\Delta n/\Delta M$		808	875	906	909	rpm/mNm
15	Terminal inductance, phase-phase	L		148	600	1 160	2 500	μH
16	Mechanical time constant	τ_m		16	18	18	18	ms
17	Rotor inertia	J		1,95	1,95	1,95	1,95	gcm²
18	Angular acceleration	$\alpha_{\ max.}$		114	107	113	100	$\cdot 10^3$rad/s²
19	Thermal resistance	$R_{th\ 1} / R_{th\ 2}$	5,7 / 19,9					K/W
20	Thermal time constant	τ_{w1} / τ_{w2}	9 / 577					s
21	Operating temperature range		– 30 ... +125					°C
22	Shaft bearings		ball bearings, preloaded					
23	Shaft load max.:							
	– radial at 3 000/20 000 rpm (4,5 mm from mounting flange)		14 / 7					N
	– axial at 3 000/20 000 rpm (push-on only)		8 / 4					N
	– axial at standstill (push-on only)		30					N
24	Shaft play:							
	– radial	≤	0,015					mm
	– axial	=	0					mm
25	Housing material		aluminium, black anodized					
26	Weight		50					g
27	Direction of rotation		electronically reversible					

Recommended values - mathematically independent of each other

				012 B	024 B	036 B	048 B	
28	Speed up to [2]	$n_{e\ max.}$		50 000	50 000	50 000	50 000	rpm
29	Torque up to [1,2]	$M_{e\ max.}$		5,2	4,9	4,8	4,8	mNm
30	Current up to [1,2]	$I_{e\ max.}$		0,98	0,48	0,34	0,23	A

2036 U ... B
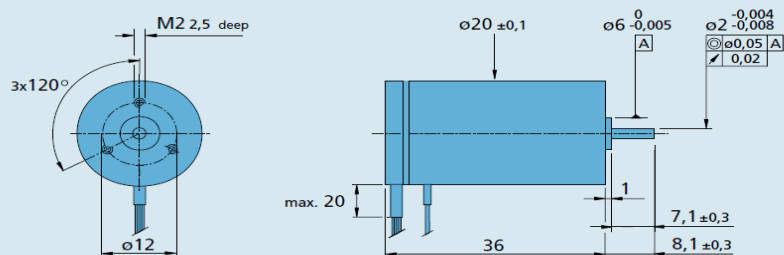
Appendix B

Tetrahedron Geometry and Configuration

In geometry, tetrahedron is a polyhedron composed of four triangular faces and also known as "triangular pyramid".
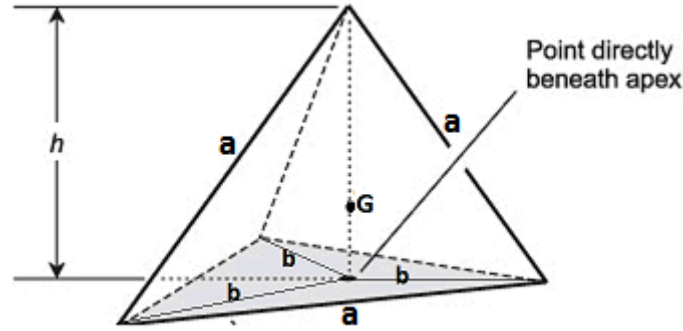
Figure B.1 – Regular Tetrahedron

Tetrahedron configuration of reaction wheels is formed by connecting each vertex with the point G (Figure B.2).
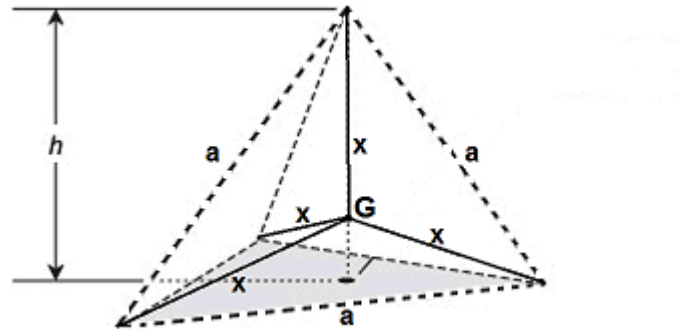
Figure B.2 – Tetrahedron Configuration

From law of cosines, the following relation can be derived (Figure B.1):

$$a^2 = b^2 + b^2 - 2b^2 cos\,(120^0) \qquad \text{(B.1)}$$

$$a^2 = 3b^2 \quad \Rightarrow \quad b = \frac{a}{\sqrt{3}} \qquad \text{(B.2)}$$

Moreover,

$$a^2 = h^2 + b^2 \qquad \text{(B.3)}$$

By substituting (B.2) into (B.3):

$$h^2 = a^2 - \frac{a^2}{3} \quad \Rightarrow \quad h = a\sqrt{\frac{2}{3}} \qquad \text{(B.4)}$$

The angle α in Figure B.3 defines the angle between reaction wheels in tetrahedron configuration.
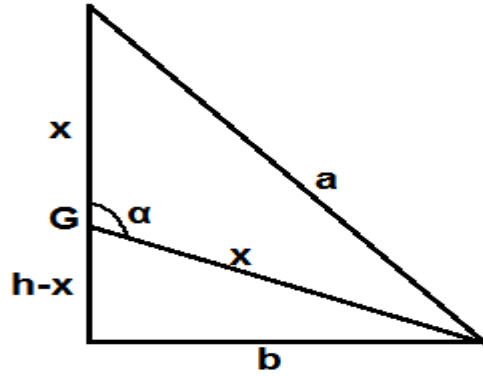
Figure B.3 – Tetrahedron angle α

From pythagorean theorem (Figure B.3):

$$x^2 = b^2 + (h - x)^2 \qquad \Rightarrow \qquad x = \frac{b^2 + h^2}{2h} \qquad \text{(B.5)}$$

By substituting (B.2) and (B.4) into (B.5), the following can be found:

$$x = \frac{\frac{a^2}{3} + 2\frac{a^2}{3}}{2a\sqrt{\frac{2}{3}}} \qquad \Rightarrow \qquad x = a\sqrt{\frac{3}{8}} \qquad \text{(B.6)}$$

From law of cosines (Figure B.3):

$$a^2 = x^2 + x^2 - 2x^2 \cos \alpha \qquad \text{(B.7)}$$

By substituting (B.6) into (B.7), angle α can be found as:

$$\cos \alpha = -\frac{1}{3} \qquad \Rightarrow \qquad \alpha = 109.47^0$$

Let us consider the following tetrahedron distribution matrix:

$$L = \begin{bmatrix} \sqrt{3}/3 & -\sqrt{3}/3 & -\sqrt{3}/3 & \sqrt{3}/3 \\ \sqrt{3}/3 & -\sqrt{3}/3 & \sqrt{3}/3 & -\sqrt{3}/3 \\ \sqrt{3}/3 & \sqrt{3}/3 & -\sqrt{3}/3 & -\sqrt{3}/3 \end{bmatrix} \qquad \text{(B.8)}$$

Each column vector in distribution matrix represents the direction vector of the wheels. For example, the first column gives the direction vector of the first reaction wheel (Figure B.4).
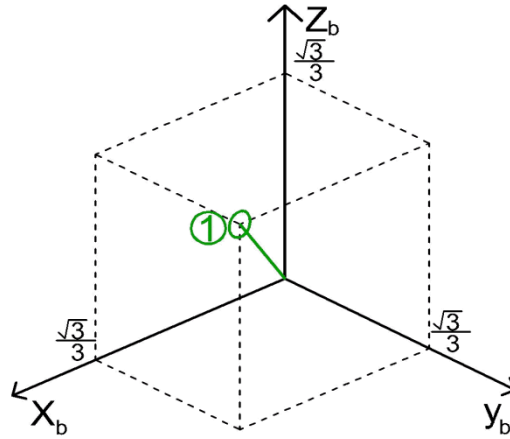
Figure B.4 – Direction of wheel-1 in body frame

By the same token, the directions of the other reaction wheels can be determined and the whole structure can be formed as depicted in Figures B.5 and B.6.
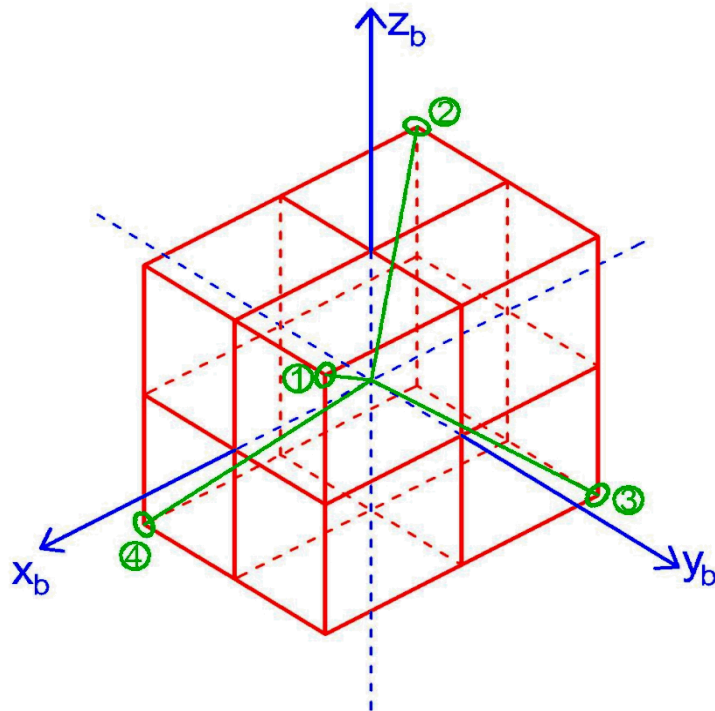
Figure B.5 – Tetrahedron configuration of reaction wheels
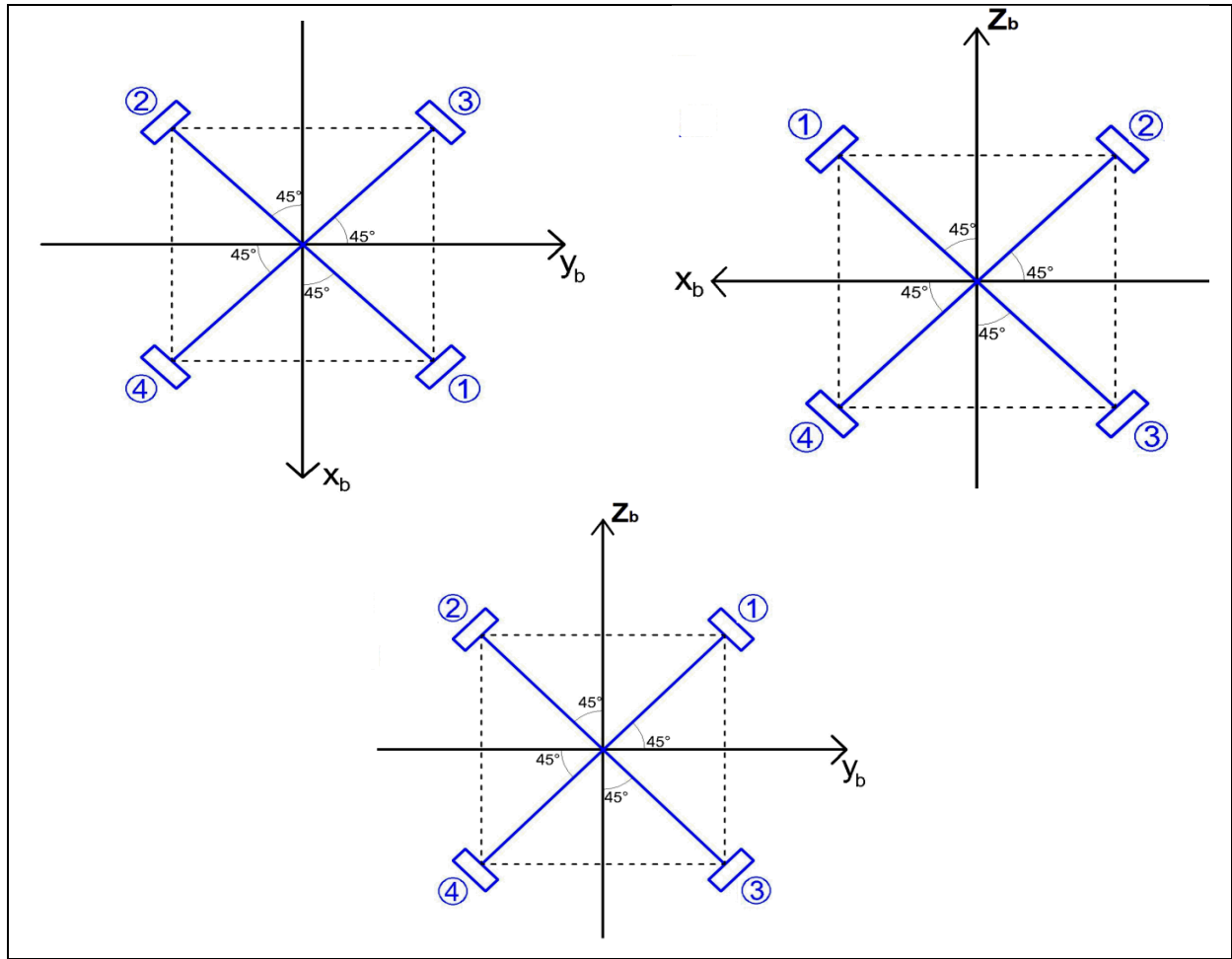
Figure B.6 – Tetrahedron configuration of wheels in x_b-y_b, x_b-z_b and y_b-z_b planes

The angle between the reaction wheels can be checked from the following dot product relation:

$$c^i c^j = |c^i||c^j|cos\alpha , \qquad |c^i| = |c^j| = 1$$

Dot product of any two column vectors in distribution matrix (B.8) will result in $-\dfrac{1}{3}$, therefore :

$$-\frac{1}{3} = cos\alpha \qquad \Rightarrow \qquad \alpha = cos^{-1}\left(-\frac{1}{3}\right) = 109.47^o$$

Appendix C

Lyapunov Stability Analysis

Ogata (1997) covered Lyapunov stability analysis in detail, while this appendix is a summary of it.

For nonlinear or time-varying systems, stability analysis may be very difficult or sometimes impossible. Eigenvalue analysis concept, which can be employed for linear time-invariant systems, does not hold for nonlinear systems. Nonlinear systems can have multiple equilibrium states. Moreover, unlike linear systems, stability behaviour of nonlinear systems may not always be global.

If we consider the system defined by:

$$\dot{\mathbf{x}} = \mathbf{f}(\mathbf{x}, t) \tag{C.1}$$

where $\mathbf{x}$ is a state vector, a state x_e where $\mathbf{f}(\mathbf{x}_e, t) = 0$ for all t is called an **equilibrium state** of the system.

An equilibrium state x_e is said to be **stable** in the sense of Lyapunov provided for each $\epsilon > 0, \exists \delta(\epsilon) > 0$:

$$\|x_e - x_0\| < \delta(\epsilon) \quad \Rightarrow \quad \|x(t) - x_e\| < \epsilon \quad \text{for all } t \geq t_0 \tag{C.2}$$

An equilibrium state x_e is said to be **asymptotically stable** if it is stable in the sense of Lyapunov and if every solution starting within $S(\delta)$ converges to x_e as t increases.

$$\text{For } \exists \delta(\epsilon): \ \|x_e - x_0\| < \delta(\epsilon) \quad \Rightarrow \quad \lim_{t \to \infty} x(t) = x_e \tag{C.3}$$

A time-varying function $V(\mathbf{x}, t)$ is said to be **positive definite** in a region Ω if there exists a positive definite function $V(\mathbf{x})$ such that:

$$V(\mathbf{x}, t) > V(\mathbf{x}), \qquad \text{for all } t \geq t_0$$

$$V(\mathbf{0}, t) = 0, \qquad \text{for all } t \geq t_0$$

A scalar function $V(\mathbf{x})$ is said to be **negative definite** if $-V(\mathbf{x})$ is positive definite.

Theorem :

Consider the system $\dot{\mathbf{x}} = \mathbf{f}(\mathbf{x}, t)$

where $\mathbf{f}(\mathbf{0}, t) = 0,$ for all $t.$ If there exists a scalar function $V(\mathbf{x}, t)$ having continuous, first partial derivatives and providing that:

1. $V(\mathbf{x}, t)$ is positive definite

2. $\dot{V}(\mathbf{x}, t)$ is negative definite

then the equilibrium state at the origin is **uniformly asymptotically stable**.

Analysis of linear time-invariant systems

Consider the following linear, time-invariant system:

$$\dot{\mathbf{x}} = A\mathbf{x} \tag{C.4}$$

where $\mathbf{x}$ is a state vector (n-vector) and A is an n-by-n constant matrix. For nonsingular A, the only equilibrium state is the origin $\mathbf{x} = \mathbf{0}$.

A possible Lyapunov function is chosen as:

$$V(x) = x^T P x \tag{C.5}$$

where **P** is a positive definite real symmetric function for **x** is a real vector and **A** is a real matrix. The time derivative of V(**x**) along any trajectory is :

$$\dot{V}(x) = \dot{x}^T P x + x^T P \dot{x}$$

$$= x^T A^T P x + x^T P A x$$

$$= x^T (A^T P + PA) x$$

For asymptotic stability, $\dot{V}(x)$ needs to be negative definite such that:

$$\dot{V}(x) = -x^T Q x \tag{C.6}$$

where $Q = -(A^T P + PA)$ is positive definite. Therefore, for the asymptotic stability of the system (B.4), it is sufficient that Q be positive definite.

Choosing an arbitrary symmetric positive definite matrix Q (e.g. $Q = \mathbf{I}$) and solving the following Lyapunov equation

$$Q = -(A^T P + PA) \tag{C.7}$$

P can be determined. Positive definiteness of **P** is a necessary and sufficient condition for the asymptotic stability of the equilibrium state $\mathbf{x} = \mathbf{0}$.

Appendix D

The Moore-Penrose Pseudo Inverse

Moore–Penrose pseudoinverse is used to compute least squares solution to a system of linear equations having not a unique solution. The Moore-Penrose pseudo-inverse is a general way to find the solution to the following system of linear equations [21]:

$$\vec{b} = A\,\vec{y} \qquad \vec{b} \in \mathbb{R}^m; \quad \vec{y} \in \mathbb{R}^n; \quad A \in \mathbb{R}^{mxn} \tag{D.1}$$

Moore and Penrose showed that there is a general solution to these equations in the form $\vec{y} = A^\dagger \vec{b}$. A Moore–Penrose pseudoinverse of A is defined as $A^\dagger \in \mathbb{R}^{mxn}$ and they proved that this matrix is a unique matrix that satisfies the following properties:

$$\textbf{1.}\ A\,A^\dagger\,A = A \tag{D.2}$$

$$\textbf{2.}\ A^\dagger A\,A^\dagger = A^\dagger \tag{D.3}$$

$$\textbf{3.}\ (A\,A^\dagger)^{\mathrm{T}} = A\,A^\dagger \tag{D.4}$$

$$\textbf{4.}\ \left(A^\dagger A\right)^{T} = A^\dagger A \tag{D.5}$$

The Moore-Penrose pseudo-inverse has the following properties:

- When $m = n$, $A^\dagger = A^{-1}$ if A has full rank.
- When $m > n$, which corresponds to a kinematically underactuated system, the solution is the one that minimizes the quantity:

$$\left\|\vec{b} - A\,\vec{y}\right\| \tag{D.6}$$

In this case, the number of equations are more than number of free variables $\vec{y}$. Hence, it is not possible to find an exact solution to these equations. The pseudo-inverse gives the solution $\vec{y}$ such that $A^\dagger \vec{y}$ is closest to the desired solution $\vec{b}$.

- When $m < n$, which corresponds to a kinematically overactuated system, the Moore-Penrose solution minimizes the norm of $\vec{y}$: $\|\vec{y}\|$. In this case, there are generally an infinite number of solutions, and the Moore-Penrose solution is the particular solution whose vector norm is minimal.

The Null Space of a matrix A, denoted $N(A)$, is defined as follows:

$$N(A) = \{\vec{v} \mid A\vec{v} = 0\} \tag{D.7}$$

If **r** is the rank of matrix A, then the null space is a linear vector space with dimension:

$$\dim\big(N(A)\big) = \max\{0, (r - n)\} \tag{D.8}$$

The Row Space of A, denoted Row(A), is the linear span of its rows. Every element of N(A) is orthogonal to any element in Row(A), and hence we say that N(A) and Row(A) are othogonal to each other. Hence, any vector $\vec{y} \in \mathbb{R}^n$ can be uniquely split into its row and null space components:

$$\vec{y} = \vec{y}_{\text{row}} + \vec{y}_{\text{null}} \tag{D.9}$$

Since Row(A) and N(A) are orthogonal to each other, it must be true by Pythogoras' theorem that:

$$\|\vec{y}\|^2 = \|\vec{y}_{\text{row}} + \vec{y}_{\text{null}}\|^2 = \|\vec{y}_{\text{row}}\|^2 + \|\vec{y}_{\text{null}}\|^2 \tag{D.10}$$

It can be concluded that, the Moore-Penrose solution is the minimum norm solution provided that the Moore Penrose solution is the particular solution that has no null space component.

$$\vec{b} = A\vec{y} = A(\vec{y}_{\text{row}} + \vec{y}_{\text{null}}) = A\vec{y}_{\text{row}} \tag{D.11}$$

When A is full rank, the Moore-Penrose pseudo-inverse can be directly calculated as follows:

- if $m < n$: $A^\dagger = A^T(A\,A^T)^{-1}$ $\hspace{4cm}$ (D.12)

- if $m > n$: $A^\dagger = (A^TA)^{-1}A^T$ $\hspace{4cm}$ (D.13)

Appendix E

List of Figures

112

113

Appendix F

Contents of the CD (Simulation Files)

acs.mdl

allocation.m

euler2q.m

figures.m

integratorBackstepping.m

quaternionFeedback.m

R_OB.m

Rzyx.m

sat_dyn.m

setupSim.m

signal.m

slidingMode.m

Smtrx.m

ucalloc.m

wI_to_wO.m

Statement of Authorship

"Except where reference is made in the text of the thesis, this thesis contains no material published elsewhere or extracted in whole or in part from a thesis submitted for the award of any other degree or diploma. No other person's work has been used without due acknowledgement in the main text of the thesis. This thesis has not been submitted for the award of any degree or diploma in any other tertiary institution."

Signed: _____

Date: _____